2018

DEFECT CHEMISTRY AND TRANSPORT PROPERTIES OF SOLID STATE MATERIALS FOR ENERGY STORAGE APPLICATIONS

Xiaowen Zhan
University of Kentucky, xzh.uky@gmail.com
Author ORCID Identifier:
https://orcid.org/0000-0002-1422-6233
Digital Object Identifier: https://doi.org/10.13023/etd.2018.418

STUDENT AGREEMENT:

I represent that my thesis or dissertation and abstract are my original work. Proper attribution has been given to all outside sources. I understand that I am solely responsible for obtaining any needed copyright permissions. I have obtained needed written permission statement(s) from the owner(s) of each third-party copyrighted matter to be included in my work, allowing electronic distribution (if such use is not permitted by the fair use doctrine) which will be submitted to UKnowledge as Additional File.

I hereby grant to The University of Kentucky and its agents the irrevocable, non-exclusive, and royalty-free license to archive and make accessible my work in whole or in part in all forms of media, now or hereafter known. I agree that the document mentioned above may be made available immediately for worldwide access unless an embargo applies.

I retain all other ownership rights to the copyright of my work. I also retain the right to use in future works (such as articles or books) all or part of my work. I understand that I am free to register the copyright to my work.

REVIEW, APPROVAL AND ACCEPTANCE

The document mentioned above has been reviewed and accepted by the student's advisor, on behalf of the advisory committee, and by the Director of Graduate Studies (DGS), on behalf of the program; we verify that this is the final, approved version of the student's thesis including all changes required by the advisory committee. The undersigned agree to abide by the statements above.

Xiaowen Zhan, Student

Dr. Yang-Tse Cheng, Major Professor

Dr. Matthew J. Beck, Director of Graduate Studies

DEFECT CHEMISTRY AND TRANSPORT PROPERTIES OF SOLID STATE MATERIALS FOR ENERGY STORAGE APPLICATIONS

DISSERTATION

A dissertation submitted in partial
fulfillment of the requirements for
the degree of Doctor of Philosophy
in the College of Engineering at the
University of Kentucky

By
Xiaowen Zhan
Lexington, Kentucky

Director: Dr. Yang-Tse Cheng, Professor of Materials Engineering
Lexington, Kentucky

2018

ABSTRACT OF DISSERTATION

DEFECT CHEMISTRY AND TRANSPORT PROPERTIES OF SOLID STATE MATERIALS FOR ENERGY STORAGE APPLICATIONS

Replacing organic liquid electrolytes with nonflammable solid electrolytes can improve safety, offer higher volumetric and gravimetric energy densities, and lower the cost of lithium-ion batteries. However, today's all-solid-state batteries suffer from low Li-ion conductivity in the electrolyte, slow Li-ion transport across the electrolyte/electrode interface, and slow solid-state Li-ion diffusion within the electrode. Defect chemistry is critical to understanding ionic conductivity and predicting the charge transport through heterogeneous solid interfaces. The goal of this dissertation is to analyze and improve solid state materials for energy storage applications by understanding their defect structure and transport properties.

I have investigated defect chemistry of cubic $Li_7La_3Zr_2O_{12}$ (c-LLZO), one of the most promising candidate solid electrolytes for all-solid-state lithium batteries. By combining conductivity measurements with defect modeling, I constructed a defect diagram of c-LLZO featuring the intrinsic formation of lithium vacancy-hole pairs. The findings provided insights into tailoring single-phase mixed lithium-ion/electron conducting materials for emerging ionic devices, i.e., composite cathodes requiring both fast electronic and ionic paths in solid-state batteries. I suggested that oxygen vacancies could increase the Li-ion conductivity by reducing the amount of electron holes bound with lithium vacancies.

Using a simpler but also attractive solid electrolyte Li_2ZrO_3 (LZO) as an example, I significantly improved Li-ion conductivity by creating extra oxygen vacancies via cation doping. In particular, Fe-doped LZO shows the highest Li-ion conductivity reported for the family of LZO compounds, reaching 3.3 mS/cm at 300 °C. This study brought attentions to the long-neglected oxygen vacancy defects in lithium-ion conductors and revealed their critical role in promoting Li-ion transport. More importantly, it established a novel defect engineering strategy for designing Li-oxide based solid electrolytes for all-solid-state batteries.

I surface-modified $LiNi_{0.6}Co_{0.2}Mn_{0.2}O_2$ cathode material with a LZO coating prepared under dry air and oxygen, and systematically investigated the effect of coating atmosphere on their transport properties and electrochemical behaviors. The LZO coating prepared in oxygen is largely amorphous. It not only provided surface protection against

the electrolyte corrosion but also enabled faster lithium-ion transport. Additionally, oxygen atmosphere facilitated Zr diffusion from the surface coating to the bulk of $LiNi_{0.6}Co_{0.2}Mn_{0.2}O_2$, which stabilized the crystal structure and enhanced lithium ion diffusion. Consequently, $LiNi_{0.6}Co_{0.2}Mn_{0.2}O_2$ cathodes coated with Li_2ZrO_3 in oxygen achieved a significant improvement in high-voltage cycling stability and high-rate performance.

KEYWORDS: Defect Chemistry, Transport Properties, Lithium-Ion Batteries, Conductivity, Electrochemical Performance.

Author's Signature: Xiaowen Zhan

Date: October 26, 2018

DEFECT CHEMISTRY AND TRANSPORT PROPERTIES OF SOLID STATE MATERIALS FOR ENERGY STORAGE APPLICATIONS

By

Xiaowen Zhan

Director of the Dissertation: Yang-Tse Cheng

Director of Graduate Studies: Matthew J. Beck

Date: October 26, 2018

Dedicated to the love of my life

ACKNOWLEDGMENTS

My last four years in UK has been a colorful journey, in which I benefited from many great people. Specially, I would like to appreciate the following individuals.

Firstly, I would like to express my greatest appreciation to Dr. Mona Shirpour, who had profound belief in my abilities at the initial stage of my Ph.D. study, and played a decisive role in preparing me as an independent researcher. Secondly, I would like to extend my deepest gratitude to my advisor Dr. Yang-Tse Cheng for his consistent support and guidance. Dr. Cheng not only guided me with extensive knowledge and in-depth discussions in research, but also offered valuable advice and continuous help on my career development. In addition, I would specially like to thank Dr. Fuqian Yang for his unwavering support in my graduate study.

Next, I must thank my committee members Dr. Chad Risko and Dr. Stephen Rankin for their efforts and suggestions on my dissertation. I also want to thank Dr. Miaofang Chi for hosting me for a short summer visit to the Oak Ridge National Laboratory in 2018, during which I acquired skills useful for my research onward.

I would also like to acknowledge my lab mates such as Shuang Gao, Yikai Wang, Yan Sun, Long Zhang, and Jiazhi Hu for their invaluable assistance. Meanwhile, I want to extend my gratitude to my previous group members Dr. Jie Pan and Dr. Qinglin Zhang for offering great career advice and help. I cannot leave UK without mentioning Nancy Miller and Nick Cprek who helped me a lot with technique problems throughout my Ph.D. projects.

Most importantly, I greatly appreciate my parents for their unconditional love and support. Especially helpful during this period when I was away from home was my sister and brother-in-law who took care of my parents.

Lastly, I want to express my deepest appreciation to my fiancée, Tiantian Zeng, who has accompanied me through highs and lows with her relentless love and understanding.

TABLE OF CONTENTS

LIST OF FIGURES

LIST OF TABLES

Chapter 1. Background and Motivations

1.1 Introduction and Rationale

Lithium-ion batteries are currently the dominant power source for portable electronic devices because of their high energy density and efficiency. Recently, there is a strong growing interest to develop large-scale lithium-ion batteries, particularly for electric vehicles. Developing batteries with high energy density, safe operation, low cost, and long life is vital for successful implementation of lithium-ion batteries in the automotive industry. In comparison with the liquid-containing batteries, all-solid-state lithium-ion batteries have been shown to exhibit improved volumetric energy density, safety, and cycle life, but their real-world application is hindered by the lack of durable and compatible materials, and the complex and costly manufacturing processes.

1.2 Common Rechargeable Lithium-Ion Batteries: Organic Liquid Electrolyte

Conventional lithium-ion batteries typically consist of a positive electrode (cathode), a negative electrode (anode), and a liquid organic electrolyte. During discharge/charge cycles, lithium ions migrate through the liquid electrolyte between the two electrodes. Large-scale lithium-ion batteries face many challenges in terms of safety, cost, and cycle life. Many of these challenges are associated with the use of flammable organic liquid electrolytes. The liquid electrolyte can leak through the containment walls of the battery and catch on fire. The liquid electrolyte cannot provide separation between the cathode and anode; therefore, polymeric separators need to be used in order to avoid short-circuit of the battery. The use of flammable organic liquid electrolytes and polymeric separators induce serious safety problems including the risk of fire and explosion. Besides these safety concerns, the complex packaging remarkably increases the manufacturing cost, and lowers the energy density by increasing the weight and volume of the battery packs. In addition, side reactions and poor thermal stability of the liquid electrolyte result in a capacity fade which shortens the battery cycle life.[1-3]

1.3 All-Solid-State Lithium-Ion Batteries: Why Solid Electrolyte?

In all-solid-state lithium-ion batteries, the components are all made up of solid phases. The non-flammability of the solid electrolyte overcomes the safety problem of the conventional lithium-ion batteries. Since solid electrolytes neither leak nor vaporize easily,

all cell components can be directly stacked in one container, instead of multiple containers as in the liquid-containing cells. Therefore, the battery size reduces (See Figure 1.1), and thus the volumetric energy density significantly improves (up to 3 times). Moreover, solid electrolytes physically separate the cathode from the anode, eliminating the need for separators. In addition, solid electrolytes have a wider range of operating voltages (over 5 V) and operating temperatures. They can be paired with certain high-voltage and high-capacity electrodes that are generally difficult to combine with liquid electrolytes (e.g., lithium metal anode and sulfur cathode). Another feature of solid electrolytes is their single-ion conduction that suppresses side reactions and leads to a long battery life. Benefiting from a unity transference number (indicating that lithium ions are the sole charge carriers), there is no concentration gradient inside the operating cells, and thus the cell over-potential is negligible. Furthermore, the capacity fade caused by the continuous decomposition of the electrode surface in contact with liquid is avoided.[4-5]

In summary, solid electrolytes improve safety, offer higher volumetric and gravimetric energy densities, and potentially lower the cost of the battery by increasing the battery life, decreasing the dead space in the battery pack, and simplifying the packaging.

1.4 Recent Progress in Solid-State Lithium-Conducting Electrolytes

The solid electrolyte is the most critical component in all-solid-state batteries. Generally, the pursuit of solid electrolytes are guided by multiple material property requirements, which mainly include:

- High total ionic conductivity comparable to that of liquid electrolytes (~10^{-2} S/cm) at operating temperature.
- A consistent ion transport number close to unity.
- Good chemical stability against moisture, Li anodes, and high voltage cathodes.
- A wide electrochemical window of ~6 V.
- Low processing cost, abundant material source and good environmental benignity.
- Stable interfaces with electrodes experiencing minor charge-transfer resistance.

Over the last few decades, many research efforts have been dedicated to the discovery of solid electrolytes with high ionic conductivity, and a large number of solid lithium ion

conducting inorganic compounds (including both crystalline and amorphous materials) have been reported, most of which are reviewed by Bachman *et al*.[6] Figure 1.2 organizes some well-known groups of conductors based on their total ionic conductivity at room temperature. Several compounds show high conductivity values near 10^{-3} S/cm, and can be considered as candidates for solid electrolytes. However, most of them only partially fulfill the above requirements. For example, thio-LISICON-type $Li_{10}GeP_2S_{12}$ exhibits a very high total conductivity of 12 mS/cm at room temperature,[7-8] but computational studies suggest that it is unstable against lithium and the experimentally observed wide electrochemical window (~5 V) is possibly due to the formation of a passivation layer.[9] In addition, this compound, similar to most sulfides, readily reacts with water and generates H_2S.[10] Similar moisture instability limits the development of Li_2S-P_2S_5 glass ceramics exhibiting high ionic conductivity of about 17 mS/cm. The other two groups of NASICON-type and perovskite-type compounds are stable at high potentials;[5, 11] however, they are unstable against lithium, and the total conductivity of the polycrystalline perovskite-type oxides is lowered by the presence of resistive grain boundaries.[12-15]

Among the abovementioned inorganic superionic materials, garnet-type cubic $Li_7La_3Zr_2O_{12}$ exhibits one of the highest lithium-ion conductivity values (up to 2 mS/cm at room temperature). Recently, this compound has been studied as the most promising candidate solid electrolyte in all-solid-state lithium batteries, due to its high ionic conductivity, good chemical stability against lithium metal, and wide electrochemical stability window.

1.5 Large-Scale All-Solid-State Lithium-Ion Batteries: Barriers and Motivations

In spite of the enormous progress, all-solid-state lithium-ion batteries are still suffering from many issues, such as low Li-ion conductivity in the electrolyte, slow Li-ion transport across the electrolyte/electrode interface, and slow solid-state Li-ion diffusion within the electrode. As a result, their electrochemical performances are far below that required for electric vehicle applications.

Defect chemistry is critical to understanding ionic conductivity and predicting the charge transport through heterogeneous solid interfaces. Therefore, this dissertation is to analyze and improve solid-state materials for energy storage applications by understanding their

defect structures and transport properties. The goal of this dissertation is twofold: (1) developing a methodology to understand the relationship between defect chemistry and electrical properties of solid electrolytes; (2) providing guidelines for improving the Li-ion transport in solid-state materials such as solid electrolytes and electrodes for energy storage applications. The knowledge gained through this research will be beneficial for not only the battery but also the solid-state ionic device research community.

Chapter 1 provides a brief background and motivations of current research, followed by an introduction to characterization techniques in Chapter 2. Chapter 3 focuses on revealing the relationship between defect structure and transport properties of garnet-type cubic $Li_7La_3Zr_2O_{12}$. Utilizing Li_2ZrO_3 as an example, Chapter 4 describes a strategy to enhance the Li-ion conductivity of Li-oxide based solid electrolytes by introducing oxygen vacancies. Based on further understandings of Li-ion transport in oxides, in Chapter 5, I designed a Li_2ZrO_3 coating that enabled facilitated Li-ion transport, stabilized bulk and interface structure, and subsequently superior electrochemical performance of $LiNi_{0.6}Co_{0.2}Mn_{0.2}O_2$ cathode materials. I conclude the dissertation with future directions in Chapter 6.

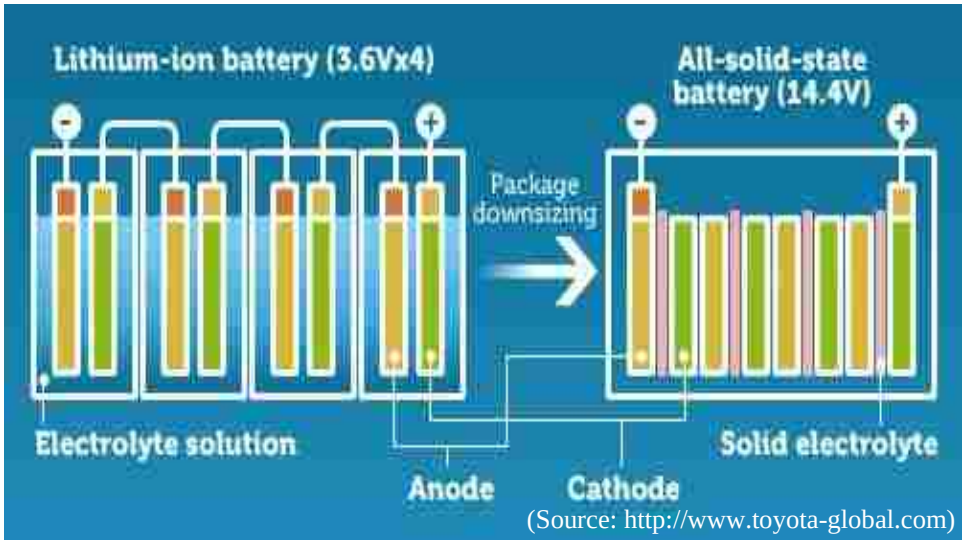

Figure 1.1 Improved packaging efficiency by direct stacking of the all-solid-state cells instead of using multiple containers in liquid-containing cells.

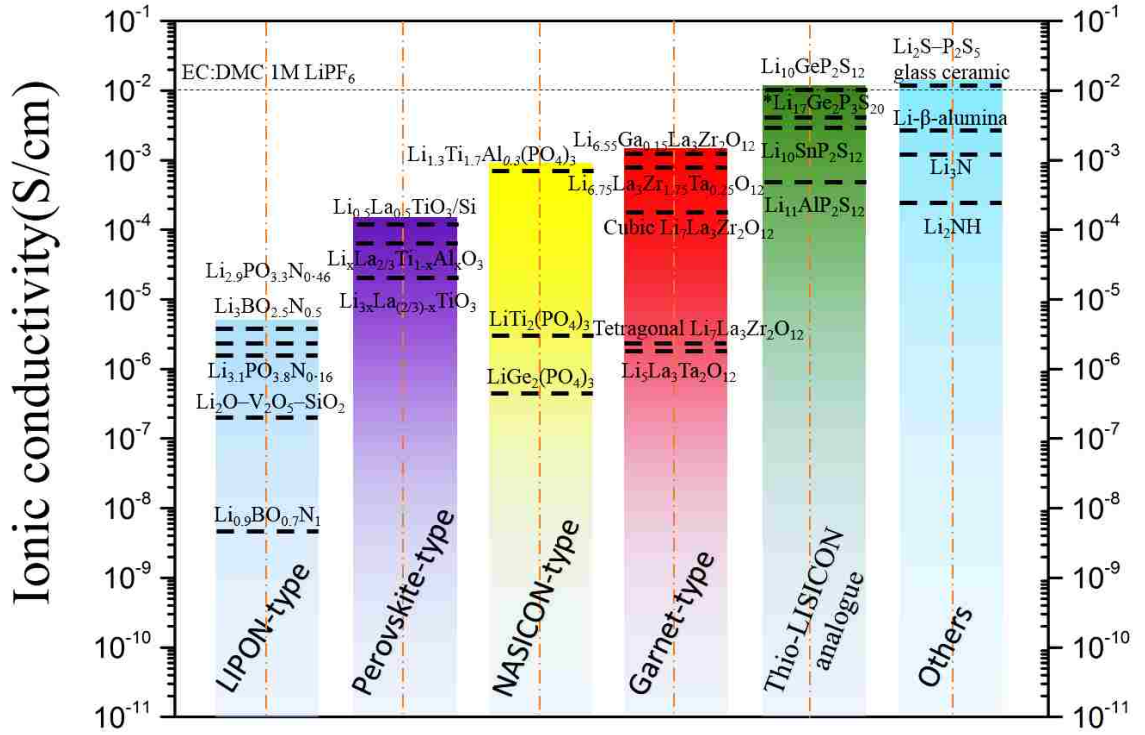

Figure 1.2 The room temperature ionic conductivity of solid-state Li-ion conducting compounds, including lithium phosphorous oxy-nitride (LIPON)-type,[1, 16-18] peroskite-type,[12, 19-20] NASICON-type,[21-22] garnet-type,[23-28] Thio-LISICON analogue materials,[8, 29-31] lithium nitride/imide,[32-33] Li-β-alumina,[34-35] and Li_2S-P_2S_5 glass ceramic.[36] *Its crystal structure is unclear.

Chapter 2. Experimental Methods

2.1 Materials Synthesis

In this dissertation, conventional solid-state method was used to synthesize solid electrolyte ($Li_7La_3Zr_2O_{12}$ and Li_2ZrO_3) and positive electrode ($LiNi_{0.6}Co_{0.2}Mn_{0.2}O_2$) materials. In addition, sol-gel method was used to prepare Li_2ZrO_3 coating for $LiNi_{0.6}Co_{0.2}Mn_{0.2}O_2$ electrodes. The detailed synthesis procedures will be introduced in the following three chapters.

2.2 Characterization Techniques

Multiple characterization techniques were used in this dissertation to characterize compositions, structures, and electrical/electrochemical properties of the synthesized materials.

Crystal structure analysis was conducted using powder X-ray diffraction (XRD). Synchrotron-based high resolution XRD (HRXRD) was used to identify impurity traces in quantities lower than the detection limit of conventional XRD. The atomic compositions were determined using inductively coupled plasma optical emission spectrometry (ICP-OES). The chemical structures were analyzed by X-ray photoelectron spectroscopy (XPS) and/or solid-state nuclear magnetic resonance (NMR) spectroscopy. Microstructures were characterized by transmission electron microscopy (TEM) and scanning electron microscopy (SEM) coupled with energy-dispersive X-ray spectroscopy (EDX).

The defect chemistry study of ceramic oxides was conducted using the measurement set-up shown in Figure 2.1, which enabled *in-situ* extraction of oxygen nonstoichiometry, and ionic and electronic conductivities of samples as a function of oxygen partial pressure and temperature. In the set-up, electrical conductivities were measured using AC impedance spectroscopy paired with DC polarization technique; oxygen nonstoichiometry was determined by thermogravimetric analysis (TGA).

Galvanostatic cycling with potential limitation technique (GCPL) was used to evaluate cycling performance of the electrode materials. Electroanalytical techniques such as electrochemical impedance spectroscopy (EIS), cyclic voltammetry (CV), and galvanostatic intermittent titration technique (GITT) were used to acquire the

electrochemical characteristics and kinetic behaviors of the active materials. The experimental details will be described in the experimental section within each of the next three chapter.

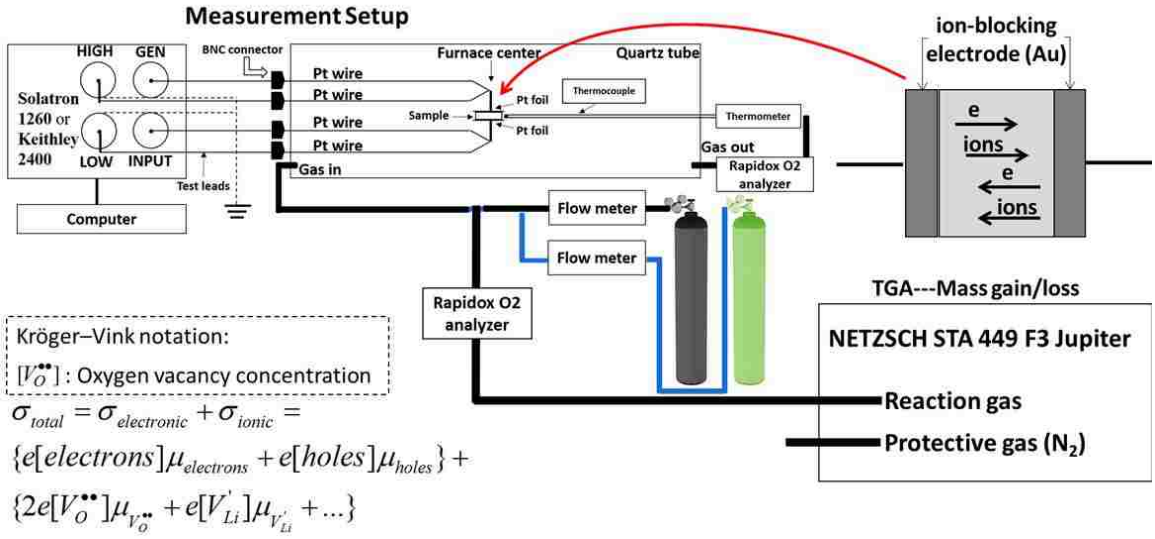

Figure 2.1 A schematic diagram of the experimental set-up used for defect chemistry study.

Chapter 3. Defect Chemistry and Electrical Properties of Cubic $Li_7La_3Zr_2O_{12}$ [1]

3.1 Summary

Garnet-type cubic $Li_7La_3Zr_2O_{12}$ exhibits one of the highest lithium-ion conductivity values amongst oxides (up to ~2 mS/cm at room temperature). This compound has emerged as a promising candidate for solid electrolyte in all-solid-state lithium batteries, due to its high ionic conductivity, good chemical stability against lithium metal, and wide electrochemical stability window. Defect chemistry of this class of materials, yet less studied, is critical to understanding of the nature of ionic conductivity and predicting properties of grain boundaries and heterogeneous solid interfaces. In this study, electrical properties of nominally undoped cubic $Li_7La_3Zr_2O_{12}$ are characterized as a function of temperature and pO_2 using a suite of AC impedance and DC polarization techniques. The formation of ionic defects and defect pairs as well as their impact on transport properties are discussed, and a Brouwer-type diagram is constructed.

3.2 Introduction

Replacing organic liquid electrolytes with nonflammable solid electrolytes in lithium-ion batteries improves safety, offers higher volumetric and gravimetric energy densities, and potentially lowers the cost of the battery by increasing the battery life, decreasing the dead space in the battery pack, and simplifying the packaging. Over the last few decades, major research efforts have been dedicated to the discovery of solid electrolytes with high ionic conductivity, and a large number of solid lithium-ion conducting inorganic compounds (including both crystalline and amorphous materials) have been reported, most of which are reviewed by Bachman *et al*.[6] Among them garnet-type cubic $Li_7La_3Zr_2O_{12}$ (c-LLZO) exhibits excellent thermal stability, chemical stability against molten lithium, and electrochemical stability against lithium metal anode, making it one of the strongest candidate as solid electrolyte for lithium-ion batteries.[37-39]

---

[1] Reproduced from *Zhan, X.; Lai, S.; Gobet, M. P.; Greenbaum, S. G.; Shirpour, M.; Defect chemistry and electrical properties of garnet-type $Li_7La_3Zr_2O_{12}$. Phys Chem Chem Phys. 2018, 20, 1447, DOI: 10.1039/c7cp06768b.*

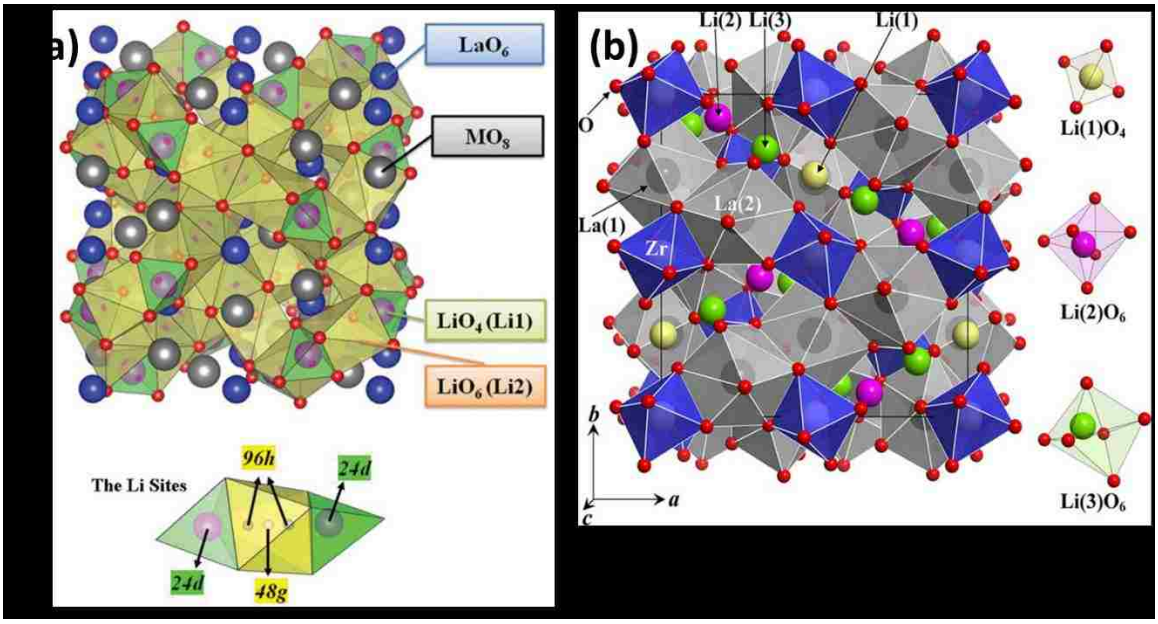

Figure 3.1 (a) Crystal structures of garnet-type cubic $Li_7La_3M_2O_{12}$. (Adapted from reference [40]. Copyright © 2012 American Physical Society. Here M=Zr) (b) Crystal structure of tetragonal $Li_7La_3Zr_2O_{12}$. (Adapted from reference [25]. Copyright © 2009 Elsevier Inc.)

The cubic phase $Li_7La_3Zr_2O_{12}$ ($Ia\bar{3}d$) exhibits room-temperature conductivities of ~10^{-4} S/cm, however, the tetragonal phase ($I4_1/acd$) is less conductive (~10^{-6} S/cm).[25] Due to the partial occupation of Li ions in both tetrahedral (24d or Li1) and octahedral (48g/96h or Li2) spaces,[41] the cubic phase (c-LLZO) exhibits much higher ionic conductivity than the tetragonal phase (t-LLZO) where all three different Li sites (8a, 16f and 32g) are completely occupied in the $I4_1/acd$ structure (Figure 3.1).[25, 42] The pure cubic phase has a narrow stability region and is metastable, and Al^{3+} diffusion from alumina crucible to the garnet structure during high temperature sintering can stabilize the cubic phase.[43] In order to stabilize the cubic phase, lower the synthesis temperature, and achieve higher ionic conductivities, different aliovalent doping methods (i.e., Al, Ga in Li sites and Ta, Nb in Zr sites) have been studied in recent years.[23-24, 44-45] So far, the highest reported total ionic conductivity is 1.8 mS/cm at 300 K achieved via a dual substitution with Sc and Ga.[46] It should be noticed that while multiple doping strategies can stabilize the cubic structure, their impact on ionic conductivity is not always predictable, as the Li-ion mobility not only depends on lithium vacancies but also the disordering of Li ions over the three Li sites. The

key of enhancing the Li^+ transport lies in increasing the ratio of $Li_{48g+96h}$ to Li_{24d} while reducing the occupation of dopants (i.e., Al and Ga) in Li1 sites.[24, 46] Li1 sites are considered to be the connection point of Li1/Li2 loops in c-LLZO sub-lattice and are critical to the 3D Li^+ transport.[47]

The practical power density of all-solid-state batteries is currently limited by the high electrolyte electrode interfacial resistance rather than the ionic conductivity of the electrolyte itself.[48] c-LLZO has shown chemical stability against Li metal reduction,[26] and seems to form a low-impedance Li/c-LLZO interface.[49-51] However, a significant interfacial impedance generally develops at the electrolyte/cathode interface, resulting in low initial discharge capacity[51-52] and poor charge retention during cycling in full cell lithium batteries.[51] Depletion of ionic charge carriers (space charge layers)[48, 53-54] and transition to tetragonal garnet due to cross diffusion of elements[55] are the suggested origins for the development of the interfacial resistance. Any of these origins are closely related to the defect structure of the bulk of c-LLZO, i.e., concentration gradients of, and interactions between ionic defects and charge carriers. Therefore, the defect chemistry of c-LLZO, while less studied, can provide insights into the composition and behavior of electrode/electrolyte interface and will help the engineering of high-performance all-solid-state lithium-ion batteries. Previous computational and experimental studies[44, 56-58] have mainly focused on the role of lithium vacancies on the formation of cubic phase and lithium ion migration. However, from a perspective of charge balance, considerable amount of uncompensated Li vacancies due to Li evaporation can lead to the formation of other charge carriers such as oxygen vacancies[44, 59] and holes that can significantly contribute to the total conductivity and thus the performance of c-LLZO in lithium-ion battery. A very recent work shows that oxygen vacancies do exist in c-LLZO and can play an important role in the cation defect chemistry, lithium ion conductivity and phase equilibria of c-LLZO.[60]

To the best of our knowledge, very few defect chemistry studies have been carried out on Li-containing oxides ($LiFePO_4$ and Li_2O_2).[61-62] Herein, in this paper, we analyze the electrical properties and construct the defect diagram of c-LLZO.

3.3 Experimental

Material synthesis. Conventional solid-state method was used to prepare LLZO compounds with the nominal composition of $Li_7La_3Zr_2O_{12}$. High-purity Li_2CO_3 (Sigma-Aldrich ≥99%), $La(OH)_3$ (Aldrich 99.9%) and ZrO_2 (Aldrich 99%) were first mixed in an agate mortar, where different amount of extra Li_2CO_3 (10/15/20 wt.%) were added to compensate for Li loss at the calcination temperature and form LLZO of various Li concentrations. The mixture was heated in an alumina crucible at 800 °C for 12 h (ramp rate: 5 °C/min) followed by a wet grinding process (300 rpm/9 h) using a planetary ball mill. The powder was then pressed into pellets using a uniaxial press at ~387 MPa and calcined at 1100 °C for 12 h (ramp rate: 5 °C/min). Each calcined pellet was crushed into powder and milled at 300 rpm/6 h. The obtained powder was pressed into a dense pellet under cold isostatic pressure (200 MPa, 30-minute hold) and annealed at 1200 °C for 36 h (ramp rate: 1 °C/min). During the abovementioned calcination steps, the pellets were placed over a powder bed of identical composition in the bottom of the crucible to prevent reactions with alumina and covered by the same powder to reduce lithium loss. Densities of pellets were derived using Archimedes method.

Characterization. Phase analysis was studied using powder X-ray diffraction (Bruker D8, CuKα, 40 kV, 30 mA) and synchrotron-based high-resolution X-ray diffraction (HR-XRD) patterns were collected on beamline 11-BM at the Advanced Photon Source at Argonne National Laboratory. The samples were loaded into Kapton capillaries and rotated during the experiment. The measurement conditions were 295.0 K, a wavelength of 0.414563 Å, and a 2θ step-size of 0.001° from -6.0° to 28.0°. The atomic compositions of Li, La, Zr, and Al were measured using inductively coupled plasma optical emission spectrometry (ICP-OES; Varian Vista Pro). Powder samples were dissolved in aqua regia and a clear solution was obtained after further digestion of the powder at 95 °C/3 h. The surface structure of LLZO pellets was studied using X-ray photoelectron spectroscopy (XPS; Thermo Scientific K-AlphaTM$^+$). To avoid interference from Li_2CO_3 formed at the surface, the samples were polished inside Ar-filled glovebox and transferred into XPS chamber with a vacuum sample holder. Characterization of microstructure was conducted by scanning electron microscopy (SEM; Quanta 250). The nuclear magnetic resonance (NMR) and MQMAS NMR experiments were performed on a 750 MHz Bruker

spectrometer. Magic angle spinning (MAS) spectra were recorded at 195 MHz for ^{27}Al, with a 4 mm rotor at a spinning rate of 15 kHz. Chemical shift values were referred to 1 M aqueous solutions of $AlCl_3$. The MAS spectra were recorded via solid echo sequence, with pulse widths of 1.5 µs with echo delay 130 µs. The recycle delay was set to 1 s for 4k scans.

AC impedance (1 Hz to 1 MHz) and DC polarization measurements with ion-blocking Au electrode were performed using a Solatron 1260 analyzer and a Keithley 2400 source meter, respectively. The sample was placed in the center of a quartz tube inside a tube furnace, with a K-type thermocouple in the close proximity to it recording the accurate temperature. Different oxygen partial pressures (pO_2) were obtained by use of controlled mixtures of Ar/O_2, and a Rapidox 2100 oxygen analyzer (Cambridge Sensotec) detects and records the in situ oxygen composition of the gas mixtures. In each atmosphere, the AC impedance and DC polarization measurements were carried out at different temperatures up to 700 °C during a cooling process. For both, data were recorded after allowing enough holding time (around 2-3 hours depending on the temperature) at each temperature in order to reach equilibrium conditions. The impedance spectra were fitted by equivalent circuits using the Z-View2 software (Scribner). DC polarization measurements with electron-blocking electrodes were established with a LiAl/LiI/LLZO/LiI/LiAl symmetric cell. The LiAl (Aldrich) and LiI (Aldrich, 99.99%) powder was pressed into pellets and contact resistance was minimized by heating the assembled cell at 200 °C for 20 h under a small load. Both preparation procedures and measurements were completed inside a glovebox under Ar atmosphere (H_2O/O_2 content <1 ppm). Non-linear fitting of all DC polarization results was performed using OriginLab Pro.

Mass loss/gain under different *p*O2 were measured using thermal gravimetric analysis (TGA; NETZSCH STA 449 F3 Jupiter). Small cuts of the sintered pellets were used and the pO_2 was controlled and recorded in the same way described for the conductivity measurement. A constant flow rate of 10 ccm was used for protection gas (Ar) and 20 ccm for prepared reaction gases. For each pO_2, a correction measurement with empty sample carrier was performed first. To avoid errors in pO_2 from unbuffered gas at lower temperatures and low pO_2, only the data points obtained at or above 600 °C were used for

analysis. The sample was first heated to 700 °C for mass reactions with the atmosphere, and then was cooled down with a three-hour holding time at each temperature of interest. The results were obtained by averaging all data points taken within holding period where little change was observed.

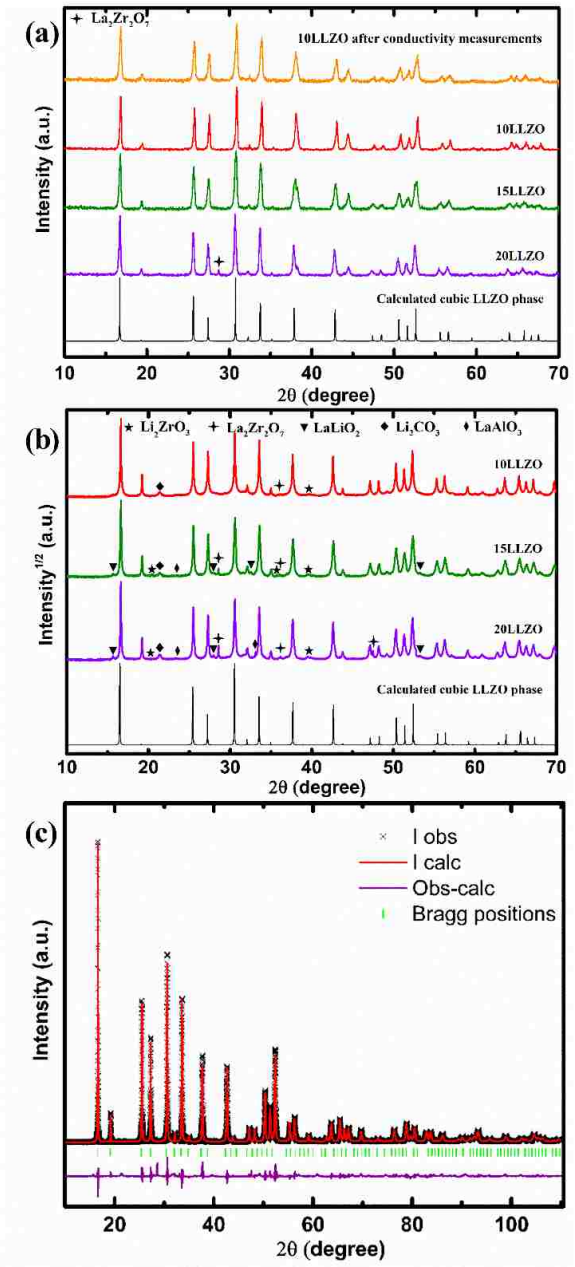

Figure 3.2 (a) XRD pattern of polished LLZO pellets (b) Synchrotron HR-XRD patterns of powder from crushed pellets (c) Full-pattern fitting for synchrotron HR-XRD of 10LLZO sample prepared with 10% Li excess.

3.4 Results and Discussion

Structure and composition. XRD patterns of sintered pellets shown in Figure 3.2a confirmed the formation of cubic phase in all samples. For 20LLZO, an additional impurity peak corresponding to $La_2Zr_2O_7$ (PDF# 01-073-0444) was observed. No tetragonal phase exists or, if any, it is in a quantity lower than the detection limit of conventional XRD. Additionally, the pellets were crushed into powders and analyzed using synchrotron HR-XRD (Figure 3.2b). Very weak reflections at 20.4°, 35.8°, and 39.6° correspond to Li_2ZrO_3 (PDF# 00-033-0843). The single weak peak at 23.4° is most probably due to presence of $LaAlO_3$ (PDF# 01-070-4126). Li_2ZrO_3 impurity phase has also been identified by Lei and Dobretsov.[59, 63] Small reflection peaks of Li_2CO_3 mainly at 21.3° (PDF# 00-001-0996) originating from the surface reactions with CO_2 were observed, too. Li_2CO_3 is less pronounced in the XRD patterns (Figure 3.2a) or XPS analysis (Figure 3.3) of sintered pellets where the surface are polished before analysis.[64] In addition, peaks of $LaLiO_2$ (PDF# 00-037-1023) at 15.7° and 28.1° were observed only in 15LLZO and 20LLZO samples.[44] Full-pattern fittings (using GSAS software[65-66]) of the synchrotron diffraction pattern for 10LLZO is shown in Figure 3.2c. The initial cubic structure where the lithium ions occupy Li1 (24d) and Li2 (48g/96h), and Al in LiI sites is used for fitting. The two theta values in Figure 3.2b and Figure 3.2c are converted to those corresponding to Cu Kα source (λ=1.54056 Å), while the calibrated wavelength used for HR-XRD is 0.414563 Å.

Figure 3.3 shows the XPS spectra collected from the top surface of the pellets. With the major peak positions of *Li*1s, *Zr*3d and *La*4d matching well with reported data,[64] a couple of differences are notable here. For *O*1s spectra, in addition to the peak at 530.8 eV assigned to O in LLZO, an extra peak at 528.3 eV exists in every sample. This peak is the characteristic of metal oxides and can be, as implied by the XRD data discussed above, assigned to O in Li_2ZrO_3 environment. In *C*1s spectra, three adventitious carbon contaminations contributions are observed at 284.6 eV, 286.0 eV and 289.1 eV, corresponding to C-C, C-O, and O-C=O components, respectively. Since the XPS data are collected after initial polishing in Ar atmosphere, characteristic peak of Li_2CO_3 at ~290.0 eV was not observed.[64] In order to ensure the charge state of zirconium during treatment at reducing environments, scans of 10LLZO pellet treated in reducing atmosphere (700 °C/3 h in 5% H_2 balanced Ar) is also shown in Figure 3.3. The spectra of C, La, and Zr do not

change after the treatment, which confirms that zirconium cations remain Zr^{4+} through the treatment. An additional *O*1s peak at ~533 eV shows up, which corresponds to C=O component from adventitious carbon contaminations. Interestingly, the major peak in *Li*1s shifts to a lower binding energy. This could originate from the generation of more oxygen vacancies in the 10LLZO sample during annealing in reduced atmosphere. Existence of oxygen vacancies in c-LLZO and their possible effects on lithium ions have been studied in a recent work by Kubicek *et al.*[60] This will be further discussed in the defect chemistry section.

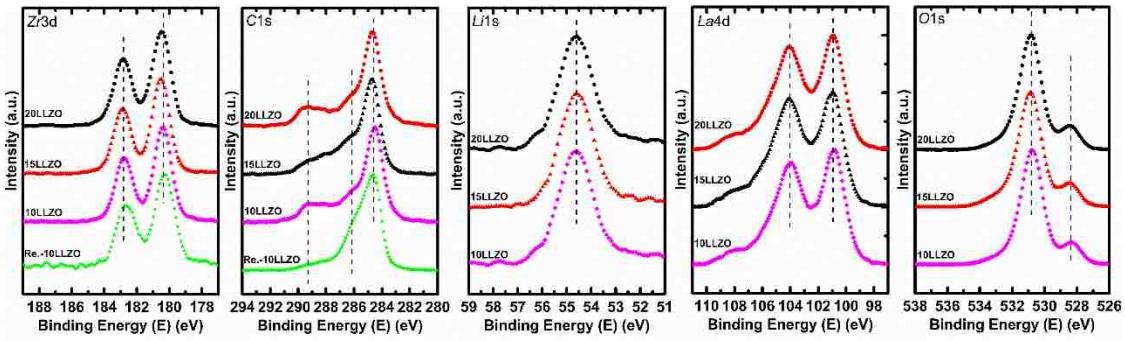

Figure 3.3 XPS spectra collected on the surface of sintered pellets, from top to bottom in each image, with 20%, 15% and 10% Li excess. The green spectra are for 10LLZO samples treated in reducing atmosphere (700 °C/3 h in 5% H_2 balanced Ar).

Figure S3.1 (see Appendices) collects the SEM micrographs of the fracture surface of sintered pellets. Table 3.1 compares composition (obtained from ICP-OES measurements) and relative density of sintered pellets. We detected an Al amount ranging from 0.19~0.26 mole per formula in the samples, where no aluminum was added intentionally during synthesis. The amount of Al was lower in the sample with higher Li excess. These observations are in agreement with previous studies that during sintering at high temperatures Al from Al_2O_3 crucible enters the Li sites and replaces the Li lost to evaporation.[43] Our results here, in accordance with previous suggestions on the stabilization effect of Al, shows that the nominally undoped LLZO in cubic phase does contain a minimum amount of Al required for the formation of cubic phase.[26, 47] Naturally, higher temperature (1200 °C) is used in our work compared to those studies with initial Al incorporation, i.e., 1000 °C with 0.24 mole Al per formula.[44]

Table 3.1 Composition, density and lattice constants of LLZO pellets in this study

Sample	Composition[1]	Relative density[2]	Lattice constant (Å)
10LLZO	$Li_{5.68}La_{3.00}Zr_{2.03}O_{11.79}Al_{0.26}$	95.8±0.3	12.9543
15LLZO	$Li_{6.07}La_{3.00}Zr_{2.01}O_{11.92}Al_{0.24}$	95.0±0.2	12.9725
20LLZO	$Li_{6.30}La_{3.00}Zr_{2.01}O_{11.96}Al_{0.19}$	93.2±0.2	13.0117

In addition to the direct chemical analysis by ICP, change in the lattice parameters (summarized in Table 3.1) reveal the effect of Al substitution. The results show that the unit cells with higher amount of Al in the lattice have smaller lattice size and this is due to the smaller ionic size of Al^{3+} compare to Li^{+}. From 10LLZO to 20LLZO, with increase in Li and decrease in Al concentrations, the lattice parameters gradually increase. Therefore, the combined effect of Al and Li content governs the phase stability of Al-containing cubic LLZO.[44] To be specific, when the Al concentration is high and the Li content is low, enough lithium vacancies (the case for 10LLZO) are generated and the cubic structure is well stabilized. On the other hand, in 15LLZO and 20LLZO with higher Li concentration and lower Al concentration, and consequently lower concentration of Li vacancies, cubic phase starts to decompose and $La_2Zr_2O_7$ phase gradually appears.[67] The oxygen nonstoichiometry δ=(y-3x-4z)/2 in $Li_{7-y}La_3Zr_{2+z}Al_xO_{12-\delta}$ (z is negligible) evaluated based on charge balance roughly reflects the joint effect of Al and Li concentration, and thus can be used as an indication of phase stability. For example, 10LLZO (δ=0.21) exhibits higher phase purity compared to 15LLZO (δ=0.09), and particularly 20LLZO (δ=0.04), as implied by the evolution of $La_2Zr_2O_7$ peak in Figure 3.2a and Figure 3.2b.

[1] Calculated ratios obtained by normalizing La to 3. Oxygen compositions are estimated based on charge balance.
[2] Averaged value from measurements on three pellets for each sample.

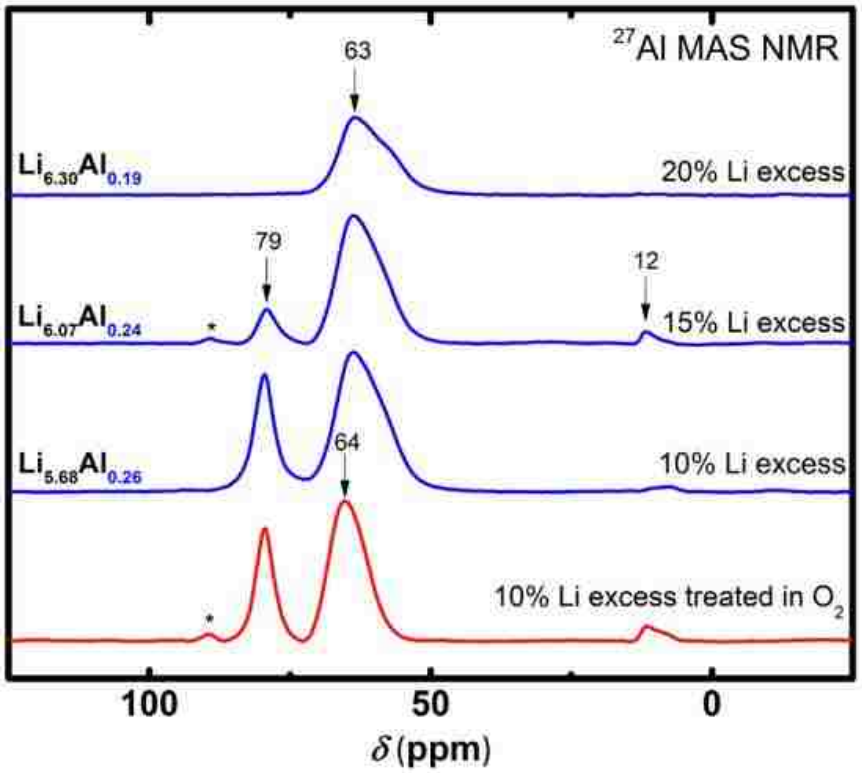

Figure 3.4 ^{27}Al MAS NMR spectra of powder from as-sintered LLZO pellets with 10%, 15% and 20% Li excess. The red spectrum is for sample with 10% Li excess treated in highly oxidized atmosphere (700 °C/3 h at pO_2=1.9 bar). *Side band.

Several ^{27}Al magic angle spinning (MAS) nuclear magnetic resonance (NMR) studies have proposed that the resonance observed at a chemical shift ranging from 63 to 68 ppm corresponds to Al^{3+} located at 24d tetrahedral site,[68] and some via DFT and data mining have provided more detailed analysis of the ^{27}Al chemical shifts related to the structure of c-LLZO.[69-70] Our NMR results (Figure 3.4) show that Al entered from the crucible, similar to the intentional added one, mainly takes the Li1 or 24d tetragonal sites, as indicated by the chemical shift at 63 ppm. The intensity of this peak indicating the Al content within c-LLZO drops with more Li excess added, and the trend matches well with the Al amount measured via ICP-OES. Besides, NMR lines with chemical shift at approximately 79 ppm are assigned to a distorted, four-fold coordinated 96h position, which are usually referred to Al in Zr or La positions.[69, 71] Li excess added in the synthesis clearly affects the Al^{3+} distribution, in that the 79 ppm feature is suppressed before it completely disappears in the 20LLZO sample. Geiger *et al.*[72] suggest that the peak at a chemical shift at 12 ppm is

octahedral coordinated Al in $LaAlO_3$. This peak shows up clearly in the NMR line of our 15LLZO sample, and we observe the corresponding impurity phase in HR-XRD patterns (Figure 3.2b). It is not appreciable in 20LLZO sample where low Al incorporation occurs. The red line at the bottom (Figure 3.4) depicts a 10LLZO sample treated in pure oxygen (pO_2=1.9 bar). It indicates similar Al distribution as untreated 10LLZO sample in terms of major peaks (Al in Li and Zr/La). However, we see a well-defined $LaAlO_3$ peak at 12 ppm for the treated 10LLZO sample. To resolve potentially overlapping lines, MQMAS NMR experiment were performed for several samples and the result for 10LLZO is provided in Figure S3.2 (see Appendices). The technique gives better resolution of the spectra that are affected by non-negligible second-order quadrupolar interactions that cannot be averaged by MAS. The ^{27}Al MQMAS spectra prove that the line broadening is not caused by overlapping sites, but 2D projection shows that a certain distribution of chemical shifts caused by a small amount of disorder in the sample. The two signals observed reflect Al ions residing in 63 ppm and around 79 ppm as mentioned above.

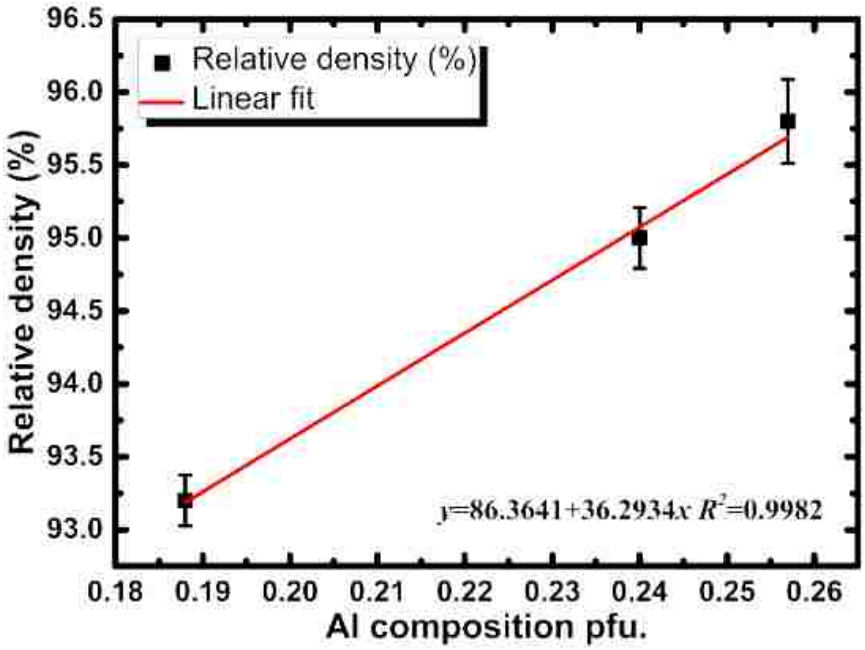

Figure 3.5 Relative density of sintered c-LLZO pellets as a function of Al concertation.

As can be seen in Figure 3.5, the rise in average relative density of sintered pellets is nearly proportional to Al concentration, suggesting that Al is being effective as a sintering aid. Electron microscopy characterizations conducted by Buschmann *et al.*[49] and

Wolfenstine *et al.*[73] revealed a homogeneous distribution of Al over all grains and no segregation of Al into grain boundaries. SEM-EDS results in Cheng *et al.*'s work showed similar uniform distribution of Al when pellets were embedded in fresh scarifying powder during sintering.[59] Our ^{27}NMR results shows that Al cations are occupying Li1 sites, therefore, most likely Al assists sintering by entering lattice, increasing Li vacancy concentration, and thereby facilitating diffusion of point defects of the species that controls sintering.[73]

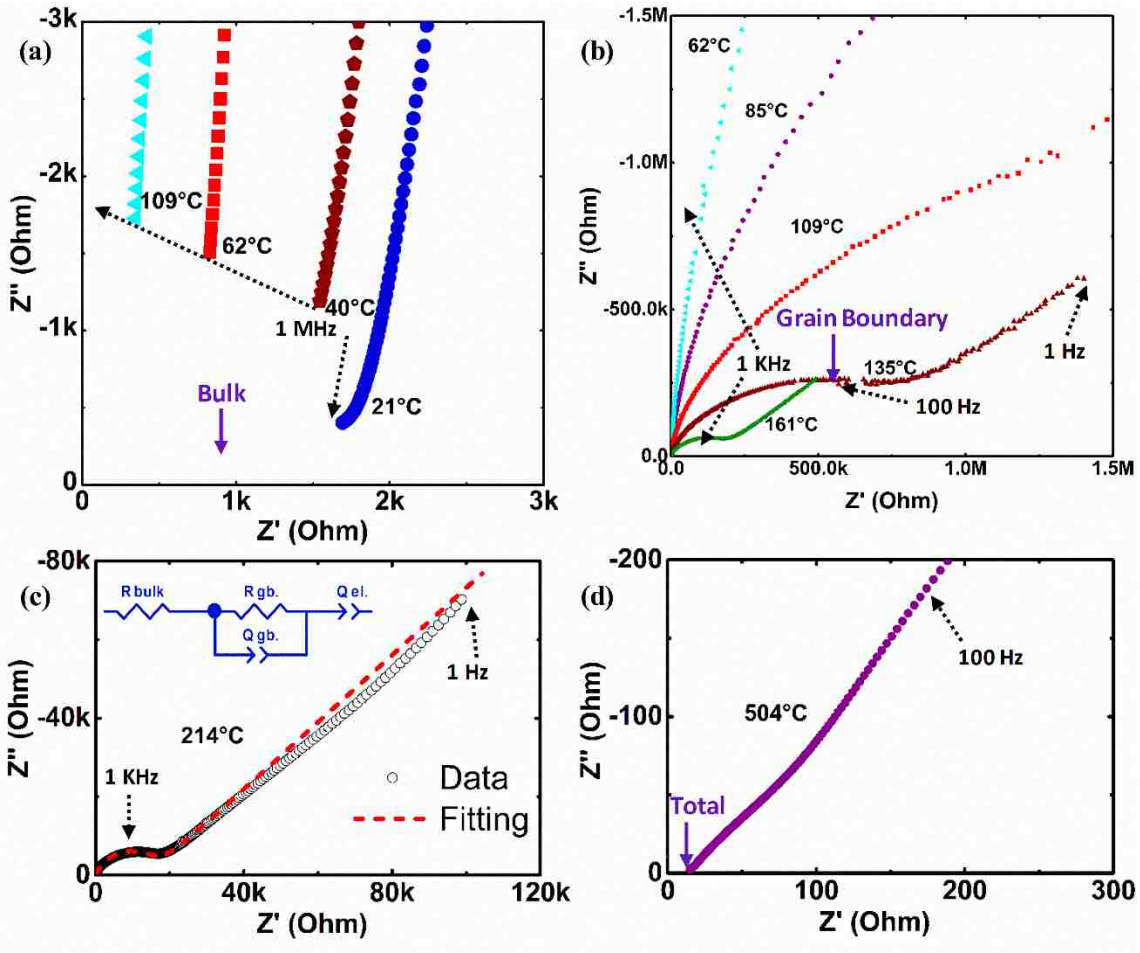

Figure 3.6 Evolution of impedance spectra with temperature measured in air for the sintered cubic 10LLZO pellet.

Transport properties. AC impedance spectra of 10LLZO pellets at different temperatures are presented in Figure 3.6a-d. At lower temperatures, the intersection point of the complex impedance curve with the real axis is attributed to the bulk resistance R_{bulk} (Figure 3.6a). Only at 135 °C and above a high frequency semicircle become visible. In

this study, this semicircle is discussed (below) and assigned to grain boundary contribution noted as R_{GB} (Figure 3.6b). Blocking character of grain boundaries in LLZO has been recently reported by Dobretsov.[63] The low frequency tail (Q_{el}) corresponds to the non-faradic behavior of the interface between LLZO and gold current collector (electrode). A typical equivalent circuit $(R_{bulk})(R_{GB}Q_{GB})(Q_{el})$ used in this study is shown in the Figure 3.6c. Q is the constant phase element and C is calculated based on $C = (QR)^{1/n}/R$, where n is an exponent that larger than 0, and n=1 corresponds to perfect capacitor.[74] As temperature increases further, the intercept with Z' axis disappears and an equivalent circuit $(R_{total}Q_{total})(Q_{el})$ is exploited. Finally, at very high temperatures (i.e., 504 °C), the intercept with Z' axis corresponds to the total resistance R_{total} (Figure 3.6d).

The values of R_{bulk}, R_{gb}, and R_{total} are plotted in Figure 3.7, and activation energies are extracted in the Arrhenius plots. The room temperature conductivity (~$2.5\cdot10^{-4}$ S/cm) calculated based on R_{bulk} is comparable to that reported by Murugan *et al*. ($4\cdot10^{-4}$ S/cm)[26] and Kotobuki *et al*. ($1.8\cdot10^{-4}$ S/cm)[51] for nominally Al-free c-LLZO samples. The activation energy of 0.30 eV is consistent with previous reports for bulk conductivity in c-LLZO.[26, 52] As discussed in the previous section, relative density, lithium vacancy concentration, and phase purity are the keys to high lithium lattice diffusion, and thus 10LLZO with the best phase purity, the highest density, and the largest lithium vacancy concentration should exhibit the highest ion conductivity (Table 3.2).

Table 3.2 Summary of transport properties for different samples

Property	Technique	Electrode	10LLZO	15LLZO	20LLZO	T (K)
$\sigma_{ion,\ bulk}$ (S/cm)	AC	Au	$2.5\cdot10^{-4}$	$1.8\cdot10^{-4}$	$5.5\cdot10^{-6}$	294
$\sigma_{ion,\ gb}$[1] (S/cm)	AC	Au	$2.1\cdot10^{-9}$	$1.9\cdot10^{-10}$	$2.7\cdot10^{-10}$	294
σ_{ion} (S/cm)	DC	LiI	$1.9\cdot10^{-9}$	$1.8\cdot10^{-10}$	$2.6\cdot10^{-10}$	294
$E_{a,\ bulk}$ (eV)	AC	Au	0.30	0.38	0.49	294-434
$E_{a,\ gb}$ (eV)	AC	Au	0.77	0.80	0.80	294-973[2]
σ_{eon} (S/cm)	DC	Au	$1.8\cdot10^{-11}$	$4.4\cdot10^{-11}$	$2.3\cdot10^{-11}$	294

[1] Extrapolated from higher temperature data shown in Figure 3.7.
[2] σ_{ion} can be readily approximated by $\sigma_{ion,\ gb}$ from 434-973 K.

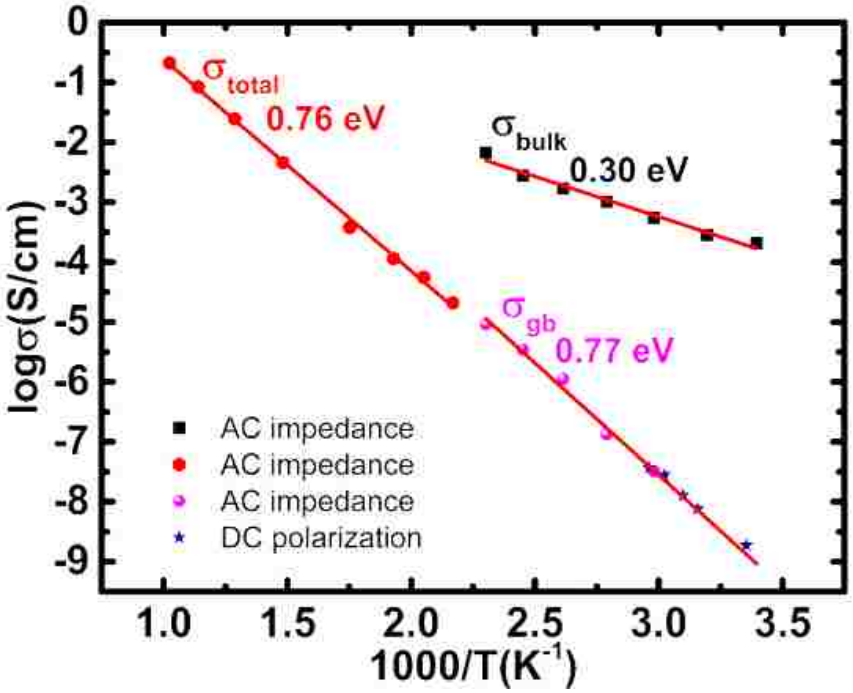

Figure 3.7 Arrhenius plots and corresponding activation energies for the sintered cubic 10LLZO pellet.

In comparison with the bulk (lattice), grain boundaries show several orders of magnitude lower conductivity and higher activation energies (0.77 eV). Resistive grain boundaries ($\sigma_{ion,\ gb}$ <10^{-8} S/cm at 25 °C) with activation energies in the range of 0.75-0.95 eV were observed in Nb-doped c-LLZO[63] and also in Al-doped c-LLZO ($\sigma_{ion,\ gb}$ ~10^{-6} S/cm and $E_{a,\ gb}$~0.5 eV).[75] Similar blocking effect at the grain boundaries of 15LLZO and 20LLZO were observed (Table 3.2). The origin of blocking grain boundaries in LLZO is not known. Previous studies suggested that Al can segregate into grain boundaries and reduce the grain boundary resistance,[76-77] which is obviously not the case here. Since Li_2ZrO_3 with ion conductivity of about $5.7 \cdot 10^{-5}$ S/cm at 598 K[78] and activation energy of 0.68 eV at 623-738 K[78] and 0.94 eV at 286-730 K[79] is identified in our XRD patterns, we suggest such impurity phase(s) located at grain boundaries could be the major origin for the blocking character of grain boundaries. In our defect chemistry studies, only lattice conductivity is taken into consideration, and further atomic level studies on the grain boundaries of LLZO seems to be important for its application as electrolyte in all-solid-state batteries.

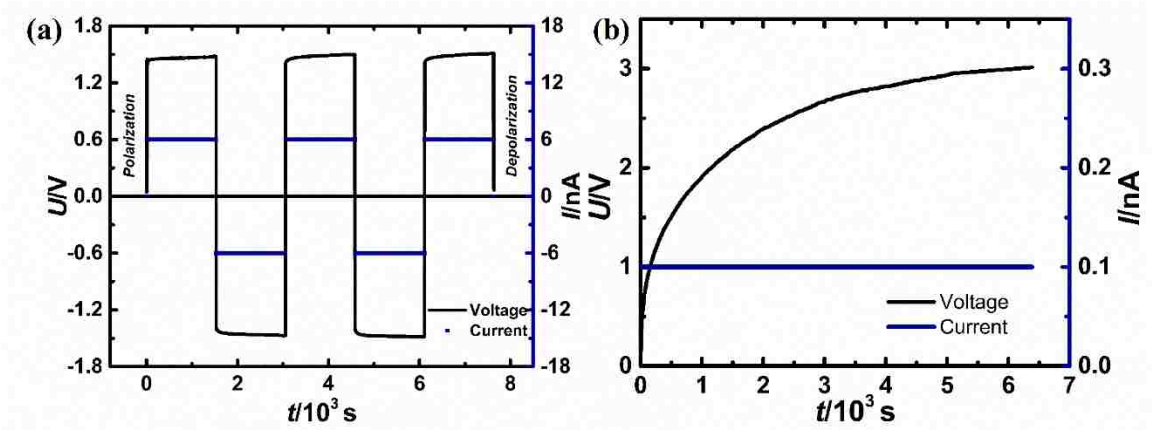

Figure 3.8 (a) Polarization and depolarization results obtained for 10LLZO sample by using electron-blocking LiI electrode. (b) Polarization results obtained for 10LLZO sample by using ion-blocking Au electrode.

To confirm the nature of ion conductivity in c-LLZO and exclude the contribution of other ionic charge carriers (e.g. oxygen ions and protons), DC polarization measurements using electron-blocking current collectors in symmetric LiAl/LiI/Sample/LiI/LiAl configuration were performed. Figure 3.8a shows a typical polarization/depolarization curve obtained from a 10LLZO pellet. Upon switching on the current, the voltage rises in a step-function manner (polarization), and decays in the same way (depolarization) upon switching off the applied current. Little change can be observed during the constant-current stage. Such behavior is indicative of predominant ionic conductivity, and the measured maximum voltage can be used to calculate the lithium-ion conductivity. As summarized in Table 3.2, the room-temperature ionic conductivity obtained from DC measurements (σ_{ion} = $1.9 \cdot 10^{-9}$ S/cm) agrees well with total conductivity of ~$2.1 \cdot 10^{-9}$ S/cm ($R_{GB} \gg R_{Bulk}$ at room temperature; $\sigma_{total} = \frac{1}{(R_b + R_{GB})} . \frac{L}{A} = \frac{1}{(R_{GB})} . \frac{L}{A} = \sigma_{GB}$) obtained from AC impedance measurements. Similar measurements were performed at elevated temperatures up to 338 K, and the data points are incorporated into the Arrhenius plot in Figure 3.7. It should be noted that these points are used to confirm the total conductivity and are not involved in determining the activation energy for grain boundary conductivity measured with AC technique. The Li-ion conductivity values obtained from DC measurements fits well with the total conductivity values and therefore lithium ions are the sole ionic charge carrier in c-LLZO.

Electronic conductivity was investigated using DC polarization measurements with Au as an ion-blocking current collector. Same configuration was used by Maier *et al*. in determining the electronic conductivity of Li_2O_2 with lithium vacancies as main charge carriers.[62] When applying a constant current, the portion of current carried by blocked ions will gradually decrease with time and eventually cease while a stationary voltage IR_{eon} is being reached (Figure 3.8b). Herein, the electronic conductivity (listed in Table 3.2) is calculated based on the applied current and the steady voltage after equilibration.

Defect chemistry. In this study, change in oxygen vacancy concentration (equilibrium with various oxygen partial pressures) in fixed lithium concentration is exploited as a tool to study the defect structure of c-LLZO. Li activity, besides oxygen vacancy concentration, is usually used in studying Li-containing oxides (i.e., Li_2O_2, $LiFePO_4$).[61-62, 80], however, since Li concentration is critical to phase stability of c-LLZO, and variation in Li amount might result in cubic-to-tetragonal phase transition,[44] Li activity is not used as a variable here.

10LLZO sample with the composition of $Li_{5.68}La_{3.00}Zr_{2.03}O_{11.79}Al_{0.26}$, superior phase purity, and the highest bulk ionic conductivity (comparable to reported values) was used for further defect chemistry studies. Lithium ion vacancy diffusion is often suggested as the conduction mechanism for c-LLZO and other Li-ion conducting solid electrolytes, and density function theory studies show that lithium ion vacancies are thermodynamically more favorable than Li ion interstitials.[56] Particularly in c-LLZO where Li sites are partially occupied and Li interstitials, if any, tend to relax into the unoccupied Li sites to minimize the system energy. Therefore, in this study, lithium ion interstitial ($Li_i^{\bullet}$) are assumed to be negligible. Lithium vacancies ($V_{Li}^{'}$) and oxygen vacancies ($V_O^{\bullet\bullet}$) are the major ionic defects. Other cation vacancies ($V_{Zr}^{''''}, V_{La}^{'''}$), interstitials ($Zr_i^{\bullet\bullet\bullet\bullet}, La_i^{\bullet\bullet\bullet}, O_i^{''}$), and antisites ($Zr_{Li}^{\bullet\bullet\bullet}, La_{Li}^{\bullet\bullet}$) are not considered as major point defects and will not be discussed. The existence of reduced cations $Zr_{Zr}^{'}$ is usually negligible[81] unless under extremely reducing atmospheres. Our XPS results (Figure 3.3) confirmed the absence of Zr^{3+} even under extremely reducing conditions. As for Al, only $Al_{Li}^{\bullet\bullet}$ will be taken into account as suggested by NMR study.

The initial c-LLZO contains a certain amount of lithium vacancies and, similar to the $LiFePO_4$ system studied by Maier and Amin[61], the concentration of Li through the course of measurements remains unchanged. This assumption of no lithium loss can be written as

$$\varepsilon = V_{Li}^{'} + V_{Li}^{X} \tag{3.1}$$

To initiate the model, internal electronic, or the intrinsic generation and recombination of electron in the conduction band and holes in the valence band is given by

$$nil \longleftrightarrow e' + h^{\bullet}\,, \tag{3.2a}$$

with *np* product being

$$K_i(T) = np = K_i{}^{0} \exp(-E_g / kT)\,, \tag{3.2b}$$

where E_g is the thermal energy gap of c-LLZO.

Then, we have oxygen loss in reduced atmosphere, noted by

$$O_O^X \longleftrightarrow V_O^{\bullet\bullet} + 2e' + 1/2O_{2(g)}\,, \tag{3.3a}$$

where the corresponding mass-action relationship is:

$$K_{red}(T) = \frac{[V_O^{\bullet\bullet}]pO_2^{1/2}n^2}{[O_O^X]} = K_{red}{}^{0} \exp(-E_1 / kT)\,. \tag{3.3b}$$

For generation of electrons in the reducing atmosphere (Eq. 3.3a-b), similar assumption was used not only in Ce-doped $Y_3Al_5O_{12}$[82] but also in $Ca_3Al_2Ge_3O_{12}$[83] where no obvious reducible cation defects were presented. On the other hand, the assumption of electron holes in Li-containing oxides have been established in both primarily Li-ion conducting phases such as Li_2O_2,[62] and electron-conducting phases such as $LiFePO_4$.[61] The generation of holes usually results from lithium evaporation during either high-temperature synthesis or post annealing in air or O_2 atmosphere. Similarly, we have the variation of hole concentration with pO_2 in oxidized atmosphere

$$V_O^{\bullet\bullet} + \frac{1}{2}O_{2(g)} \longleftrightarrow O_O^X + 2h^{\bullet}\,, \tag{3.3c}$$

where the corresponding mass-action relationship is

$$K_{ox}(T) = \frac{[O_O^X]p^2}{[V_O^{\bullet\bullet}]pO_2^{1/2}} = {K_{ox}}^0 \exp(-E_2/kT)\,, \tag{3.3d}$$

where pO_2 is the oxygen partial pressure and E_2 is the corresponding reaction energy for the reduction. It should be noted that the reactions described in Eq. 3.3a and Eq. 3.3c may be only completely fulfilled at relatively high temperatures where oxygen ions can migrate via the highly mobile vacancies in the crystal lattice.

The charge neutrality is given by

$$n + [V_{Li}^{'}] = 2[V_O^{\bullet\bullet}] + p + 2[Al_{Li}^{\bullet\bullet}]\,. \tag{3.4}$$

Finally, the ionization equilibrium for the trapping of electronic charge carriers is introduced by

$$V_{Li}^{'} + h^{\bullet} \longleftrightarrow V_{Li}^{X}\,, \tag{3.5a}$$

with the mass-action law being given by

$$K_l(T) = \frac{[V_{Li}^X]}{[V_{Li}^{'}]p} = {K_l}^0 \exp(-E_3/kT) \tag{3.5b}$$

The total conductivity of a solid is given as the sum of contributions from all charged species by

$$\sigma = \sum_i |z_i| q n \mu_i\,, \tag{3.6}$$

where z_i, q, n, and μ_i are the ith specie's charge, charge of an electron, concentration, and mobility, respectively.

The logarithmic dependencies of conductivities (σ), mobilities (u), and concentrations (c) of carrier j on the control parameters are described as:[61]

$$E_j \equiv -R\frac{\partial \ln \sigma_j}{\partial 1/T}\,, \tag{3.7a}$$

$$h_j \equiv -R\frac{\partial \ln u_j}{\partial 1/T}, \tag{3.7b}$$

$$W_j \equiv -R\frac{\partial \ln c_j}{\partial 1/T} = E_j - h_j, \tag{3.7c}$$

We have here assumed three distinct regions (N, I, and P) in the defect diagram. In region N, under highly reducing conditions, of the high concentration of positively charged oxygen vacancies ($V_O^{\bullet\bullet}$) is balanced by the electrons generated in the conduction band. Thus, Eq. 3.4 can be simplified as

$$n = 2[V_O^{\bullet\bullet}] \text{ while } [V_O^{\bullet\bullet}] >> [Al_{Li}^{\bullet\bullet}]. \tag{3.8}$$

In region I, as the degree of reduction decreases and concentration of electrons drops, the $V_O^{\bullet\bullet}$ concentration is close to the concentration of $V_{Li}^{'}$ concentration, and it is given by, at reduced conditions

$$[V_{Li}^{'}] = 2[V_O^{\bullet\bullet}] + 2[Al_{Li}^{\bullet\bullet}]. \tag{3.9}$$

As pO$_2$ continues to rise and the $h^{\bullet}$ concentration reaches certain concentration in region P such that it is comparable to oxygen vacancy concentration and it is no longer negligible, the charge neutrality Eq. 3.4 becomes

$$[V_{Li}^{'}] = 2[V_O^{\bullet\bullet}] + p + 2[Al_{Li}^{\bullet\bullet}]. \tag{3.10}$$

The defect association reaction indicated by Eq. 3.5a is considered to mainly happen in this region.

In the remaining of this section, based on our experimental findings, we will try to construct the defect diagram of c-LLZO.

Figure 3.9 described the evolution of bulk conductivity over the measured pO$_2$ range up to 188 ˚C that is the highest temperatures where we can separate the bulk (lattice) conductivity from the total (bulk + GB) conductivity. It should be noted here that in the defect structure analysis, only the lattice transport is concerned unless otherwise stated. Firstly, at very low pO$_2$ (region N), concentration of electrons (*n)* is assumed to be comparable to $[V_O^{\bullet\bullet}]$ so that $n \approx 2[V_O^{\bullet\bullet}] \propto p\mathrm{O}_2^{-1/6}$, and they contribute partially to the

observed change in overall (ionic + electronic) lattice conductivity as a function of pO_2. Moving to the intermediate pO_2 region, a plateau that is characteristic of an ionic region is observed. In this intermediate region, $[V_{Li}^{'}]$ remains approximately constant and is mainly determined by $[V_O^{\bullet\bullet}]$. At high *p*O2 region, a negative slope for conductivity was observed. This negative slope cannot be explained by a typical behavior of mixed ion conductors where a positive slope at pO_2 is often reported. The behavior of c-LLZO in this region is here discussed based on, formation of hole-vacancy pairs and trapping of $[V_{Li}^{'}]$ by holes that results in reduced concentration of mobile $[V_{Li}^{'}]$ at high pO_2.

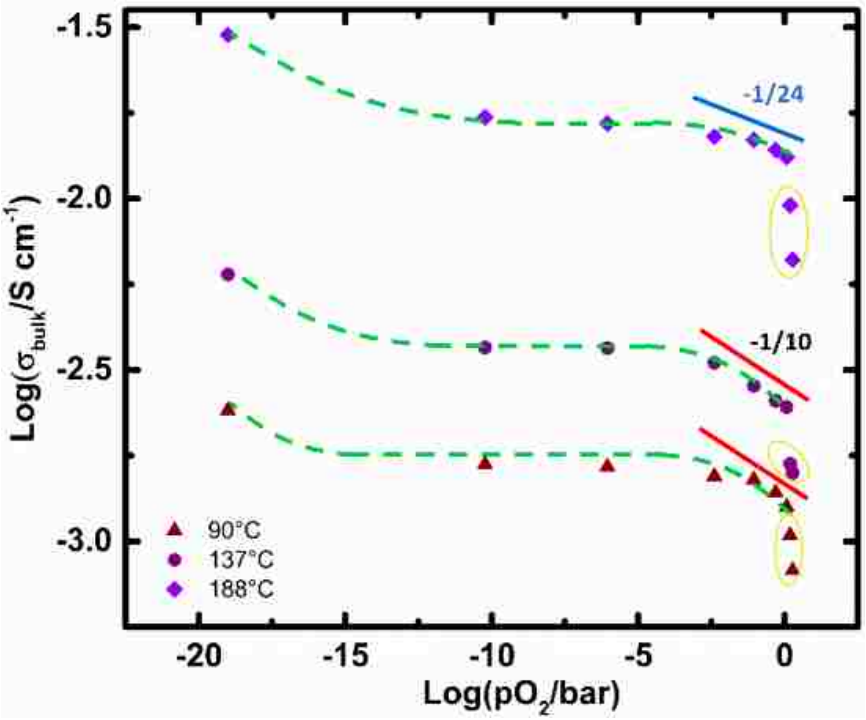

Figure 3.9 The change of bulk conductivity measured with AC impedance spectra as a function of oxygen partial pressure. The dotted lines are for eye-guiding purpose.

Figure 3.10a shows the electronic conductivity of c-LLZO as a function of pO_2. An *n*-type and a *p*-type electronic conduction behavior is revealed at very low and high pO_2, respectively. A typical Arrhenius plot of electronic conductivity in region P measured with aforementioned DC polarization technique is shown in Figure 3.10b. A clear transition from an association to a non-association regime (upward bending in $\sigma_{eon.}$ in the direction of lower temperature) is witnessed with $T_{trapping}$=137° C being the turning point, which

confirms the proposed trapping of $h^{\bullet}$ by $V_{Li}^{'}$. Similar discontinuity due to dependency of defect association on temperature was observed in $LiFePO_4$[61]. Meanwhile, the trapping of holes by $V_{Li}^{'}$ is proved to be a key factor in understanding the defect structure of Li-ion compounds with either dominant Li-ion (Li_2O_2,[62]) or electronic conductivity ($LiFePO_4$,[61]). Generally, such charge carrier trapping is considered to mainly prevail at lower temperatures.[84-85] Bearing in mind that the ionization equilibrium described in Eq. 3.5 is a local process and therefore should be reversible under experimental conditions. We propose that at $T < T_{trapping}$ the holes are considerably trapped by charged lithium vacancies while at $T > T_{trapping}$ they gradually dissociate. In the absence of trapping at higher temperature, an oxygen partial pressure dependency of $p \propto pO_2^{1/6}$ was observed (Figure 3.10a). Below 137 °C, the smaller pO_2 dependence of 1/10, is partially due to trapping effect and loss of free holes. Naturally, the transition during cooling is a continuous process thus an intermediate slope of 1/8 just above 137 °C is expected. Another reason for weakened pO_2 dependence at lower temperatures (<400 °C) could be that mobility of oxygen ions drops with cooling, which gradually lighten the effect of defect reaction described in Eq. 3.3c.

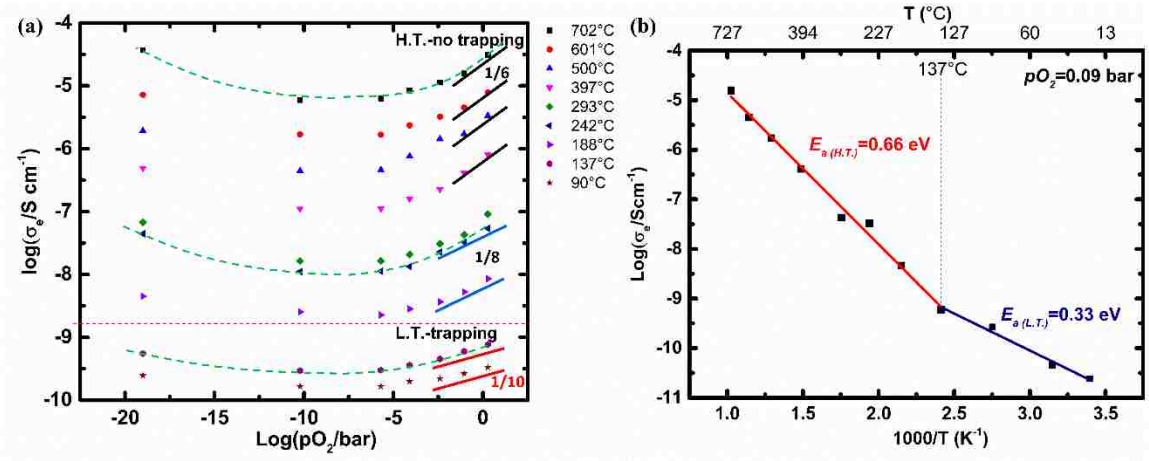

Figure 3.10 (a) Electronic conductivity isotherms as a function of pO_2 obtained from DC Polarization measurements with ion-blocking Au electrode. The dotted lines are for eye-guiding purpose. (b) A typical Arrhenius plot of electronic conductivity in region P showing dependence of trapping on temperature.

Now back to the lattice conductivity changes shown in Figure 3.9, as the lithium vacancy transport dominates the total conductivity in c-LLZO, the increase in electronic conductivity with pO_2 is not large enough to compensate the loss of ionic conductivity due to trapping (region P). Combining Eq. 3.1 and 3.5b will result in

$$p = \frac{\varepsilon - [V_{Li}^{'}]}{K_l [V_{Li}^{'}]}. \tag{3.11}$$

Substituting the observed $p \propto pO_2^{1/10}$ (Figure 3.10a) of the trapping region in highly oxidizing atmosphere into Eq. 3.11, $[V_{Li}^{'}] \propto pO_2^{-1/10}$ is derived. This slope fits well with the slope revealed at 90 °C or 137 °C (Figure 3.9) where trapping is expected. Moreover, the slope at 188 °C appears to be smaller, marking the onset of $[V_{Li}^{'}]$-hole dissociation which is in good agreement with in the observed changes in electronic conductivity changes (Figure 3.10a).

Figure 3.11 shows the change in the concentration of oxygen vacancies in terms of nonstoichiometry δ in $Li_{5.68}La_{3.00}Zr_{2.03}Al_{0.26}O_{12-\delta}$, directly derived from thermogravimetric (TG) measurements. Cuts of sintered pellets, same to that used in conductivity measurements, were used for the TGA measurements to minimize contributions from change in surface stoichiometry.[86-87] Therefore, the assumption of no lithium loss applies here, and the weight change shown in Figure 3.11 originates from the variation of oxygen vacancy concertation with pO_2. By the decrease in pO_2, the oxygen nonstoichiometry first increased with a slope of -1/6 (what we called region P) and then gradually reached a plateau in the region I. Substituting $p \propto pO_2^{1/6}$ observed for electronic conductivity at high temperatures (Figure 3.10a) into Eq. 3.3d will give $[V_O^{\bullet\bullet}] \propto pO_2^{-1/6}$ that matches with the measured slop here.

Figure 3.12 collects the activation energies extracted from AC and DC measurements as a function of pO_2. For ionic bulk conductivity, the activation energy of 0.32 eV measured in region I represents the migration barrier of Li^+ alone in the lattice and is consistent with the values reported for c-LLZO structures with similar compositions.[26, 44, 51] For electronic conductivity, in region P the higher-temperature activation energy is found to be ~0.66 eV

while at lower temperatures it is ~0.33 eV. At certain fixed pO_2, when $T > T_{trapping}$, directly from Eq. 3.3d

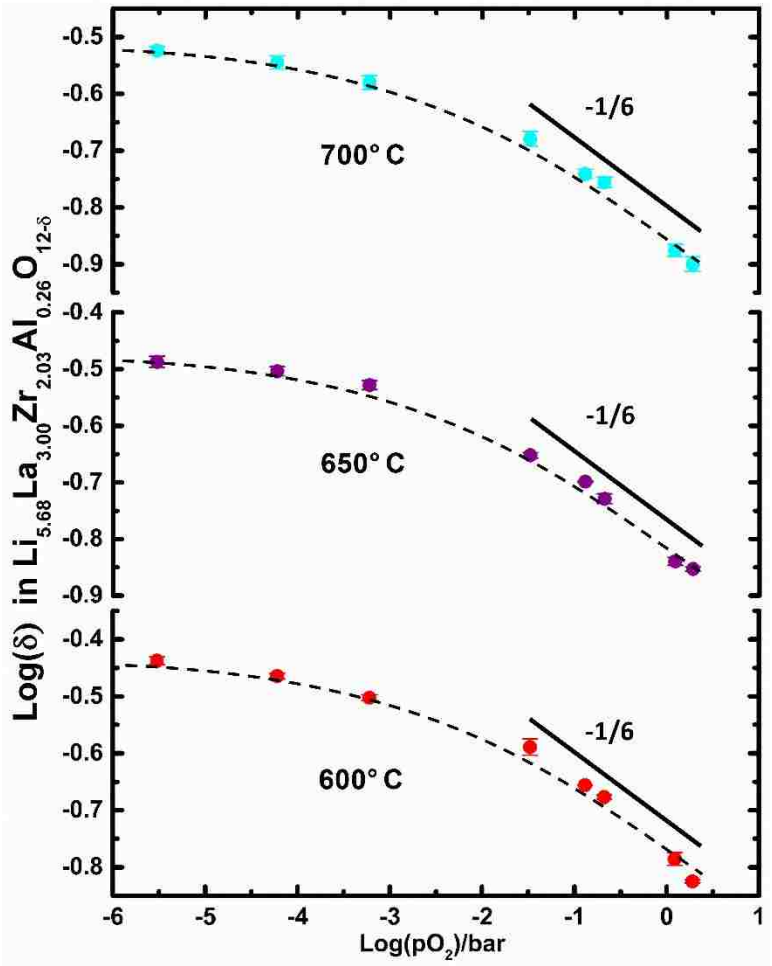

Figure 3.11 Nonstoichiometry of oxygen of 10LLZO in derived from Thermogravimetric measurements. The δ values are referred to that calculated from ICP in air (pO_2=0.21) and the dotted lines are for eye-guiding purpose.

$$W_{h,HT} \equiv -R\frac{\partial \ln p}{\partial 1/T} = E_2/2 \text{ (P-region, no trapping).} \quad (3.12)$$

When $T < T_{trapping}$, the activation of the hole concentration is determined by both oxygen dissolution and trapping. Assuming that V_{Li}^{X} is constant and allowing sufficient trapping by sufficient Li deficiency, we can expect $[V_{Li}^{'}] \approx [h^{\bullet}]$ at certain high pO_2, which simplifies Eq. 3.11 to

$$K_l p^2 + p - \varepsilon = 0 \,. \tag{3.13}$$

Therefore, the activation of hole concentration should be

$$W_{h,LT} \equiv -R\frac{\partial \ln p}{\partial 1/T} = E_2/2 - E_3 \text{ (P-region, trapping).} \tag{3.14}$$

Assuming electrons and holes move by a large polaron process known for ionic conductors,[62, 82, 88] their migration energy h_h (a second-order term) may be ignored. Therefore

$$E_{h,LT} = W_{h,LT} \text{ , and } E_{h,HT} = W_{h,HT} \,. \tag{3.15}$$

Hence, E_3 and E_2 can be estimated to be 0.33 eV and 1.32 eV, respectively. This trapping energy is comparable to the reported value for Li_2O_2 (0.47 eV[62]). In addition, 0.65 eV and 0.30 eV were reported[61] for electronic conductivity of $LiFePO_4$ in trapping and non-trapping region, respectively, and they agree well with our results shown in Figure 3.10b (trapping: 0.33 eV; non-trapping: 0.66 eV).

As pO_2 decreases, $[V_{Li}^{'}]$ is compensated by the sum of $[V_O^{\bullet\bullet}]$ and $[Al_{Li}^{\bullet\bullet}]$. The amount of electrons now is comparable with that of holes, and they together contribute to the observed electronic conductivity. From here, the discontinuity in Arrhenius plot is no longer appreciable due to the weakened effect of trapping on total electronic conductivity, and we thus have one single activation energy. In highly reduced atmosphere, the electron concentration arises according to Eq. 3.3a to compensate the generated oxygen vacancies and an n-type behavior is demonstrated. Combining Eq. 3.3b and 3.8 yields

$$n = (2K_{red})^{1/3} pO_2^{-1/6} \,, \tag{3.16}$$

which implies

$$W_e \equiv -R\frac{\partial \ln n}{\partial 1/T} = E_1/3 \,. \tag{3.17}$$

Again, by neglecting the electron migration barrier h_e

$$E_e = W_e \,. \tag{3.18}$$

As the activation energy extracted from Arrhenius plot in region N is E_e~0.57 eV, thus the enthalpy of E_1=1.70 eV for reaction described by Eq. 3.3a is calculated.

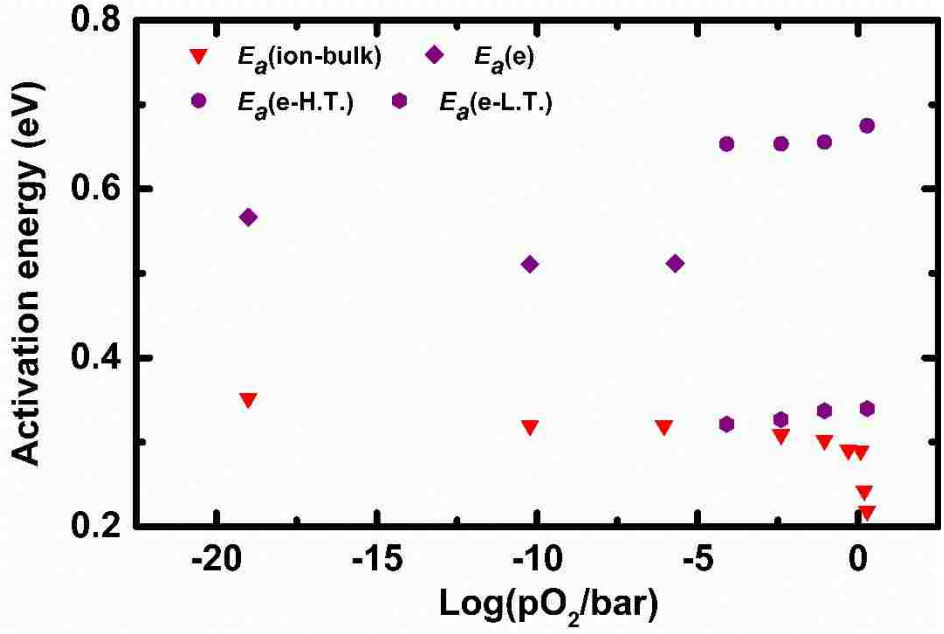

Figure 3.12 Activation energies for ionic and electronic conductivities extracted from Arrhenius plots at different pO_2.

The bulk (lattice) conductivity (Figure 3.9) experiences an abrupt drop when approaching the extremely high pO_2 (> 1 bar) values, and highly deviates from the predicated slope. Meanwhile, abnormal deviation can be seen in Figure 3.12 for the corresponding activation energies. Our ^{27}Al MAS NMR data on the c-LLZO powders annealed at 700 °C for 3 h and in oxygen with pO_2=1.9 suggests that a secondary phase (precipitate), i.e., $LaAlO_3$ (Figure 3.4), forms as the oxygen partial pressure increases. The destructive effect of dispersed secondary phases on the bulk conductivity of the matrix material has been studied in several ionic conductors, e.g., TiO_2/SiO_2,[89] LiI/Al_2O_3,[90] and $Y_3Al_5O_{12}/Al_2O_3$.[91] The formation of this secondary phase could be an origin of the conductivity drop; however, this reaction should be reversible since the conductivity goes back to its original value after the pO_2 again decreases. Another possibility is reversible changes in the distribution Al in c-LLZO throughout the sample. Park *et al*. observed using TOF-SIMS that, after annealing $LiCoO_2$ particles on a c-LLZO pellet at 700 °C, Al cations diffuse significantly from the core toward the surface of c-LLZO pellets (or LLZO/$LiCoO_2$

interface) and even enter the adjacent $LiCoO_2$ phase.[55] As Al, especially those in Li sites, are critical to the phase stability of c-LLZO, Al leaching out of c-LLZO could cause partial transformation to tetragonal phase especially at the surface.[55] Therefore, it is highly possible that, the exposure to ultra-high pO_2 during heating leads to dramatic Al redistribution within our c-LLZO bulk and considerably drags down its ionic conductivity.

Table 3.3 Concentrations of defect species under different neutrality conditions

Charge Neutrality Conditions: $[V_{Li}^{'}]+n+[Al_{Zr}^{'}]=2[V_O^{\bullet\bullet}]+p+2[Al_{Li}^{\bullet\bullet}]$; No lithium loss: $\varepsilon=[V_{Li}^{'}]+[V_{Li}^{X}]$			
	Region N: $p(O_2)$ = *low* $n=2[V_O^{\bullet\bullet}]$	Region I: $p(O_2)$ = *Intermediate* $[V_{Li}^{'}]=2[V_O^{\bullet\bullet}]+2[Al_{Li}^{\bullet\bullet}]$	Region P: $p(O_2)$ = *high* $[V_{Li}^{'}]=2[V_O^{\bullet\bullet}]+p+2[Al_{Li}^{\bullet\bullet}]$
n	$(2K_{red})^{1/3}pO_2^{-1/6}$	$(K_{red})^{1/2}(\frac{[V_{Li}^{'}]-2[Al_{Li}^{\bullet\bullet}]}{2})^{-1/2}pO_2^{-1/4}$	Non-trapping ($T > T_{trapping}$): $(\frac{K_i^{\,2}}{K_{ox}})^{1/2}[V_O^{\bullet\bullet}]^{-1/2}pO_2^{-1/4} \propto pO_2^{-1/6}$
p	$(\frac{K_i^{\,3}}{2K_{red1}})^{1/3}pO_2^{1/6}$	$(\frac{K_i^{\,2}}{K_{red}})^{1/2}(\frac{[V_{Li}^{'}]-2[Al_{Li}^{\bullet\bullet}]}{2})^{1/2}pO_2^{1/4}$	Non-trapping ($T > T_{trapping}$): $K_{ox}^{1/2}[V_O^{\bullet\bullet}]^{1/2}pO_2^{1/4} \propto pO_2^{1/6}$ Trapping ($T < T_{trapping}$): $\frac{\varepsilon-[V_{Li}^{'}]}{K_l[V_{Li}^{'}]} \propto pO_2^{1/10}$
$[V_O^{\bullet\bullet}]$	$(\frac{K_{red}}{4})^{1/3}pO_2^{-1/6}$	$\frac{[V_{Li}^{'}]-2[Al_{Li}^{\bullet\bullet}]}{2}$	$V_O^{\bullet\bullet} \propto pO_2^{-1/6}$
$[V_{Li}^{'}]$	$\sim \varepsilon$	$\sim \varepsilon$	Non-trapping ($T > T_{trapping}$): $\sim \varepsilon$ Trapping ($T < T_{trapping}$): $\propto pO_2^{-1/10}$
$[V_{Li}^{X}]$	$\rightarrow 0$	$\rightarrow 0$	Non-trapping ($T>T_{trapping}$): $\rightarrow 0$ Trapping ($T < T_{trapping}$): $\varepsilon-[V_{Li}^{'}]$

The total conductivity (bulk + grain boundary) as a function of pO_2 is provided in Figure S3.3 (see Appendices). If we ignore the last two data points at extremely high pO_2 based on the discussion above, the pO_2 response of grain boundaries are close to that of bulk conductivity in all regions. According to Maier *et al.*,[92] when a space charge layer is the origin of blocking grain boundaries, different grain and grain boundary partial pressure dependencies are usually observed. On the other hand, if current restriction is the origin for

resistive grain boundaries, the activation energy for the conductivity of bulk and grain boundary will be comparable. Therefore, we suggest that depletion of charge carriers in space charge region and presence of discontinuous impurity phases are not the main origins for the blocking effect of grain boundaries, but the role of a continuous and relatively "insulating" layer at the grain boundaries is highly possible. Since Li_2ZrO_3 impurity phase observed in our HR-XRD is a poor Li-ion conductor with activation energies close to the one measured for the GBs of c-LLZO, we suggest it as the major cause for the blocking character of grain boundaries.

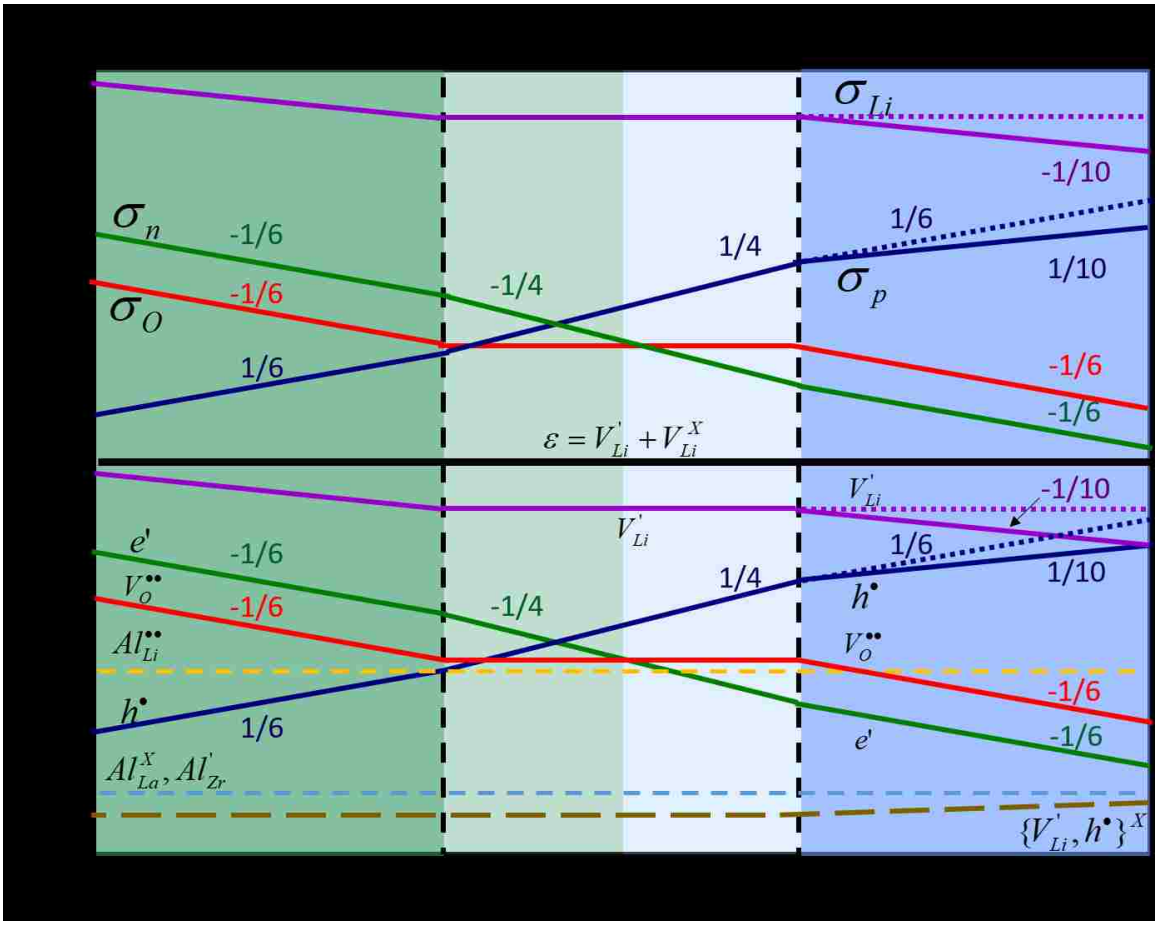

Figure 3.13 Derived defect and carrier concentration as a function of oxygen partial pressure. The lines on the top is an approximated trend curves for fractional conductivities in log scale. For lithium vacancies and holes in region P, the solid line depicts the case of trapping while the dashed line for non-trapping. Numbers denote line slopes of pO_2 dependencies.

Table 3.3 summarizes concentrations of defect species in different regions. Figure 3.13 demonstrates the Brouwer-type diagram constructed based on our experimental findings and the boundary conditions discussed above. Since mobility of charge carriers is generally independent,[93] we assume conductivity and charge carrier concentration follow similar trends. While the defect model and experimental observations are largely in good agreement, two points might be worthy of notice. Firstly, in ionic region (I) and highly reduced region (N), for simplicity of the model and emphasis on the trapping region P, the charged lithium vacancy concertation ($[V_{Li}^{'}]$) is estimated as ~ε (Table 3.3). However, based on Eq. 3.5b, in a more accurate consideration $[V_{Li}^{'}]$ should increases accordingly as hole concertation (p) gradually decreases from region P to region N. This rise in $[V_{Li}^{'}]$ and in electronic conductivity with decreasing pO_2 jointly contributes to the observed trend for total conductivity in region N. Secondly, oxygen vacancies might facilitate the conduction of lithium ions through elastically deforming of the c-LLZO lattice or/and reducing the Li stoichiometry, as suggested by Kubicek *et al*.[60] Positive effect of oxygen vacancies on ionic conductivity was reported in the Na_2ZrO_3 system, too, where the Y-doped Na_2ZrO_3 with more oxygen vacancies exhibits higher Na-ion conductivity compared to undoped Na_2ZrO_3.[94] However, the migration barrier for bulk transport (Figure 3.12), at least in the scenario of this study, is not lowered when introducing more oxygen vacancies. Most probably, oxygen vacancies benefits Li-on conductivity in c-LLZO mainly by acting as a donor and reducing the lithium composition during the phase formation.[60] Our defect chemistry study, as stated in previous sections, is carried out for as-sintered c-LLZO samples at lower temperatures with frozen Li stoichiometry, and is thus free of such effect.

3.5 Conclusions

The composition, structure and transport properties of cubic $Li_7La_3Zr_2O_{12}$ were systematically studied and consistent dependencies of ion conduction, electronic conductivity, and defect reactions with temperature and oxygen activity were observed and discussed in details. A defect diagram is proposed that is in good agreement with the experimental findings and modeling discussions and provides a tool useful in identifying dominant point defects in Li-ion conducting LLZO as a function of ambient conditions. Of particular importance is the association effect between lithium vacancies and holes at

intermediate or low temperatures regions even though the electronic conductivity seems to be negligible. The role of lithium vacancy-hole pairs is particularly important since solid-state ion conductors are often prepared in air and function at room- or near room-temperature devices. In solid-state Li-ion conductors like c-LLZO, in addition to the abovementioned positive effect of oxygen vacancies on Li-ion migration from the respect of lattice deformation or lithium stoichiometry, we suggest that oxygen vacancies might also benefit the Li-ion conductivity by reducing the amount of electron holes and thus mitigating their association with lithium vacancies. Final sintering or post-annealing in inert atmospheres with relatively low oxygen partial pressures might help, but should be carried out without costing relative density, phase stability and appropriate lithium composition, which are also necessary for high Li-ion conductivity.

In addition, the intrinsic formation of lithium vacancy-hole pairs could explain why mixed lithium-ion conducting compounds, unlike mixed oxygen-ion conducting compounds, are scarce. We think design of mixed lithium-ion conducting compounds could be of interest, as well as a challenge, to tailoring materials for emerging ionic devices. For example, utilization and performance of composite cathodes in solid-state batteries can improve if one single mixed lithium-ion conducting compound provides both electronic and ionic path for transport.

Chapter 4. Lithium-Ion Transport in Doped Li_2ZrO_3: The Role of Oxygen Vacancies[1]

4.1 Summary

Understanding Li-ion migration mechanisms and enhancing Li-ion transport in Li_2ZrO_3 (LZO) is important to its role as solid absorbent for reversible CO_2 capture at elevated temperatures, as ceramic breeder in nuclear reactors, and as electrode coating in high voltage lithium-ion batteries (LIBs). Although defect engineering is an effective way to tune the properties of ceramics, the defect structure of LZO is largely unknown. This paper reports the defect structure and electrical properties of undoped LZO and a series of cation-doped LZOs: (1) depending on their charge states, cation dopants can control the oxygen vacancy concertation in doped LZOs; (2) the doped LZOs with higher oxygen vacancy concentrations exhibit better Li^+ conductivity, and consequently faster high-temperature CO_2 absorption. In fact, the Fe (II)-doped LZO shows the highest Li-ion conductivity reported for LZOs, reaching 3.3 mS/cm at ~300 °C that is more than one order of magnitude higher than that of the undoped LZO.

4.2 Introduction

LZO is an attractive material to both energy and environmental applications. It has been extensively studied as a solid absorbent for reversible CO_2 capture at elevated temperatures,[95] and as a ceramic breeder for nuclear reactors.[96] It can also be employed in LIBs as a coating for both anode (i.e., carbon and silicon[97]) and high voltage cathode materials (i.e., $LiMn_2O_4$, $LiNi_{0.4}Co_{0.2}Mn_{0.4}O_2$, and $LiNi_{0.7}Co_{0.15}Mn_{0.15}O_2$[98-99]). Recently, a $70Li_2S$-$30P_2S_5$/LZO glass-ceramic electrolyte is reported to have a high ionic conductivity of 3 mS/cm at room temperature.[100]

For CO_2 adsorption, Li-ion diffusion is a critical factor that determines both the surface absorption and high-temperature CO_2 release process.[101-102] For LIBs, a thin LZO coating can help enhance Li-ion conductivity, chemically inertness, and electrochemical stability of electrodes.[78, 98, 103] For nuclear fusion, Li^+ migration through vacant sites inside LZO grains is closely related to tritium (^3H) release, which is a key performance indicator of a

[1] Reproduced from *Zhan, X.; Cheng Y.-T.; Shirpour, M.; Nonstoichiometry and Li-ion transport in lithium zirconate: The role of oxygen vacancies. J Am Ceram Soc. 2018, 101, 4053, DOI: .10.1111/jace.15583*

breeder material.[101, 104-105] Therefore, understanding Li^+ migration mechanisms, and enhancing Li^+ transport in LZO are important to its many technological applications.

An effective way to tune the Li^+ conductivity in Li-based oxides is via defect engineering, which requires knowledge in the defect chemistry, i.e., types and concentrations of point defects and their effects on Li^+ conductivity. Previous experimental and computational studies have shown that Li^+ hopping through vacant sites is responsible for Li^+ migration in LZO. Generally, a higher lithium vacancy concentration would lead to higher Li^+ conductivity and lower migration barrier.[78, 101] Oxygen vacancies, while less studied, are another source of ionic defects in LZO. In Li-based oxides, oxygen vacancies can form during synthesis due to the evaporation of Li in the form of Li_2O at elevated temperatures:[106-107]

$$2Li_{Li}^{X} + O_{O}^{X} \rightarrow 2V_{Li}' + V_{O}^{\bullet\bullet} + Li_2O\ (g). \tag{4.1}$$

When aliovalent dopants are introduced, the defect formation becomes more complicated. For instance, trivalent dopants M^{3+} (M=Al, Ga, etc.) in Zr^{4+} site generate positively charged oxygen vacancies to maintain charge balance:

$$M_2O_3 \xrightarrow{Li_2ZrO_3} 3O_{O}^{X} + 2M_{Zr}' + V_{O}^{\bullet\bullet}. \tag{4.2}$$

According to DFT calculations by Kordatos *et al*., the dopants will strongly bind with the nearest neighbor oxygen vacancies.[108] Oxygen vacancies induced by cation doping or lithium loss will have an impact on the Li^+ diffusion in LZO. Recently, Fleig *et al*. confirmed the existence of oxygen vacancies in multiple doped cubic $Li_7La_3Zr_2O_{12}$ structures, and suggested these oxygen vacancies can influence Li^+ conductivity by reducing Li concentration, and by elastically deforming the lattice to affect lithium migration pathways.[109] The former scenario associates directly with the concentration and the later links to the mobility of Li^+, and these two factors jointly governs Li^+ conductivity. Defect chemistry, i.e., the comprehensive effects of oxygen and lithium vacancies, is therefore critical to the understanding of Li^+ transport in LZO and should be further explored.

It has been reported that K-doped LZO exhibits faster CO_2 absorption reactions than undoped LZO owing to the improved lithium and oxygen conduction, however, the ionic conductivity was not reported.[110] The Li^+ dynamics in Nb, Y, and Ta-doped LZO was recently studied by solid-state NMR and DFT calculations.[111] They suggested that the introduction of Nb or Ta would lead to formation of Li vacancies and reduce the activation barrier, while yttrium introduces lithium interstitials resulting in a higher activation barrier for Li^+ migration. Since this study assumes stoichiometric oxygen composition, oxygen vacancies, potentially affecting Li^+ transport,[108-109] are not considered. The importance of oxygen vacancies has been emphasized in Y-doped monoclinic-structured Na_2ZrO_3, where Y^{3+} substituting Zr^{4+} was suggested to create oxygen vacancies thereby improving Na^+ conductivity as confirmed by impedance measurements.[94] However, to the best of our knowledge, the influence of oxygen vacancies on the electrical conductivity of doped LZO has not be reported.

Herein, we systematically characterize undoped and a series of cation-doped LZO materials. The relationship between their Li^+ conductivities and oxygen/lithium nonstoichiometries is established. We demonstrate that oxygen vacancies in doped LZOs are vital to their ionic conductivities and thus CO_2 absorption. The method and approach may be applicable to other lithium oxides.

4.3 Experimental

Material synthesis. For making LZOs, Li_2CO_3 (Sigma-Aldrich ≥99%) and ZrO_2 (Aldrich 99%) were first mixed in an agate mortar, where a 5 wt% extra Li_2CO_3 was added to compensate for Li loss at high temperatures. For doped LZOs, Li_2CO_3, ZrO_2 and MO_x (Nb_2O_5, TiO_2, CeO_2, and Fe_2O_3: Alfa, 99.9%; Al_2O_3, Sigma-Aldrich, 99.5%; Ga_2O_3 and MgO Alfa, 99.99%) were first mixed with a molar ratio of Li: Zr: M= 2.1: 0.9: 0.1. The mixture was preheated in an alumina crucible at 350 °C for 6 h (ramp rate: 5 °C/min). The powder was then hand-ground and pressed into pellets using a uniaxial press at 542 MPa and calcined at 950 °C for 10 h (ramp rate: 3 °C/min) in air. Each calcined pellet was crushed into powder and milled at 300 rpm for 6 h in acetone. The obtained powder was pressed into a dense pellet using cold isostatic pressure (200 MPa, 6-min hold) and finally sintered at 1000 °C for 12 h (ramp rate: 5 °C/min) in air or under controlled Ar/O_2 flow.

During the abovementioned calcination steps, the pellets were placed over a powder bed of identical composition in the bottom of the crucible to prevent reactions with alumina crucible and covered by the same powder to reduce lithium loss. The density of pellets was derived using Archimedes method. The final sintered pellets were either polished for conductivity measurements or crushed into powders for further analysis. The pellets were stored in a glovebox under argon.

Characterization. Phase analysis was conducted using powder X-ray diffraction (Siemens D5000, CuKα, 40 kV, 30 mA). Synchrotron-based high-resolution X-ray diffraction (HR-XRD) patterns were collected on beamline 11-BM at the Advanced Photon Source at Argonne National Laboratory. The samples were loaded into Kapton capillaries and rotated during the experiment. The measurement conditions were 295.0 K, a wavelength of 0.414563 Å, and a 2θ step-size of 0.001° from -6.0° to 28.0°. The atomic compositions were measured using inductively coupled plasma/optical emission spectrometry (ICP-OES; Varian Vista Pro). Powder samples were dissolved in aqua regia and a clear solution was obtained after further digestion of the powder at 95 °C for 3 hours. The surface composition of as-sintered pellets was studied using X-ray photoelectron spectroscopy (XPS; Thermo Scientific K-Alpha). To avoid interferences from impurities such as LiOH and Li_2CO_3 formed on the surface, the samples were polished inside Ar-filled glovebox and transferred into XPS chamber with a vacuum sample holder. Characterization of microstructure was conducted by scanning electron microscopy (SEM; Quanta 250) and grain size distribution was estimated using ImageJ.

Conductivity measurements were performed in Ar with minimal traces of CO_2 and moisture (both <1 ppm). Ionic conductivity was determined by AC impedance method using a Solatron 1260 analyzer in the frequency range of 1 Hz to 1 MHz. Electronic conductivity was measured by DC polarization approach with ion-blocking Au electrodes using a Keithley 2400 source meter. Conductivity measurements were carried out during a cooling process. Data were recorded after allowing enough holding time (2-3 hours depending on the temperature) at each temperature in order to reach equilibrium conditions. The impedance spectra were fitted by equivalent circuits using the Z-View2 software (Scribner).

The CO_2 absorption behavior of the samples was investigated using thermal gravimetric analysis (TGA; NETZSCH STA 449 F3 Jupiter). In each measurement, 20 mg of powder was heated to 600 °C with a heating rate of 10 K min^{-1} and held at 600 °C for 40 hours. The protective gas was N_2 and the reactive gas was pure CO_2, with a flow rate of 10 mL min^{-1} and 50 mL min^{-1}, respectively.

4.4 Results and Discussion

Undoped LZO

Phase, composition, and microstructure. In the previous conductivity studies of LZO, the final sintering was carried out either in O_2 or in inert gas (i.e., He)[78, 103], while the effect of atmospheres on phase stability and electrical properties of LZO were unclear. Figure 4.1a compares XRD patterns of samples sintered in three different atmospheres with 5% Li excess. For samples sintered in Ar and O_2 (herein after called LZO-Ar and LZO-O_2), single monoclinic phase formed since no impurity phases were detected. In the highly reducing atmosphere (5% H_2 balanced Ar), the $Li_6Zr_2O_7$ and Li_2CO_3 secondary phases appear.

Based on the XRD full-pattern fittings (using GSAS software[65-66]) lattice parameters are a=5.412 Å, b=9.008 Å, c=5.409 Å, β=112.695 ° for LZO-Ar (Figure 4.1b), and a=5.422 Å, b=9.022 Å, c=5.419 Å, β=112.690 ° for LZO-O_2 (see Figure S4.1a in Appendices). The lattice parameters extracted for the powder obtained after calcination at 950 °C/10 h in air and before final sintering (see Figure S4.1b in Appendices) are a=5.421 Å, b=9.025 Å, c=5.418 Å, and β=112.699 °, which are very close to those of LZO-O_2 and are consistent with reported values.[78, 112] Unlike LZO-O_2, the LZO-Ar sample showed shrinkage in lattice size after sintering. Considering that both samples have very similar lithium compositions and relative densities (summarized in Table 4.1), extra oxygen vacancies were most likely created in LZO-Ar during final sintering at 1000 °C in Ar (pO_2~10^{-6} bar).

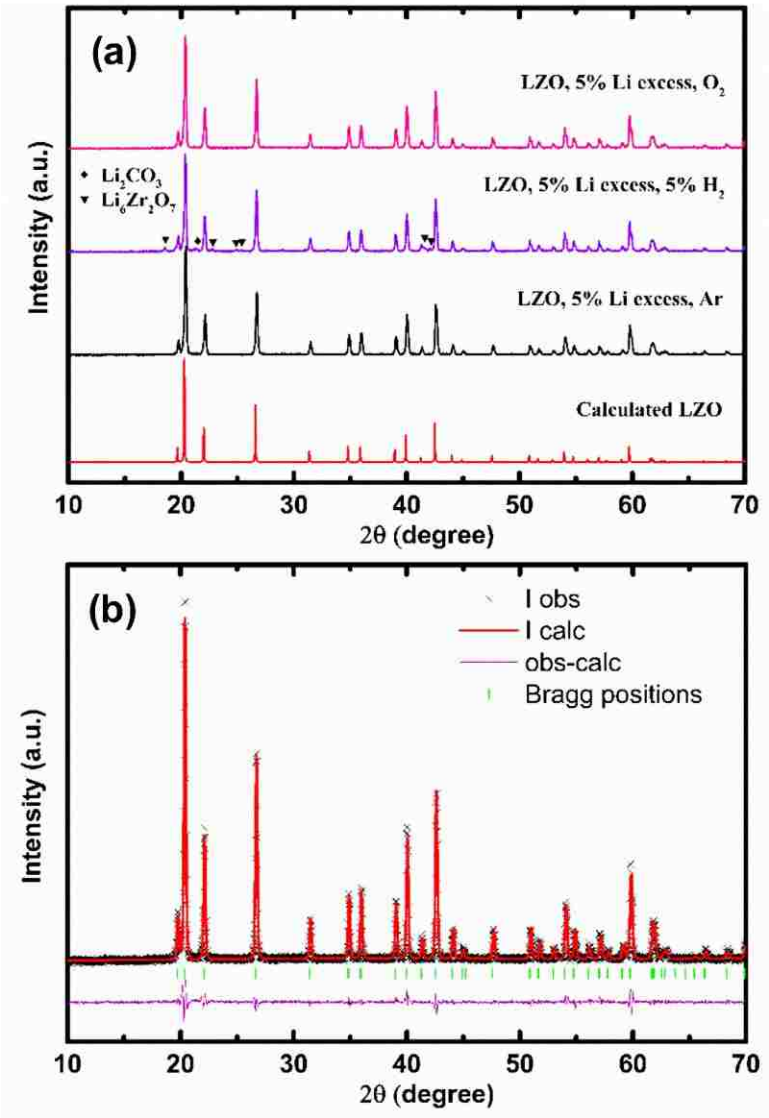

Figure 4.1 (a) XRD patterns of pulverized pellets sintered in different atmospheres with 5% Li excess. (b) Full-pattern fitting on the XRD pattern of pulverized LZO-Ar pellet.

As shown in Figure 4.2, LZO-Ar and LZO-O_2 have similar microstructures. The average grain size of LZO-Ar (4.5 μm) is slightly larger than that of LZO-O_2 (3.8 μm). The EDX element mappings are collected in Figure S4.2 (see Appendices), where a uniform distribution of Zr over grains and grain boundaries is observed for both samples. The effect of microstructure on their electrical properties is thus negligible.

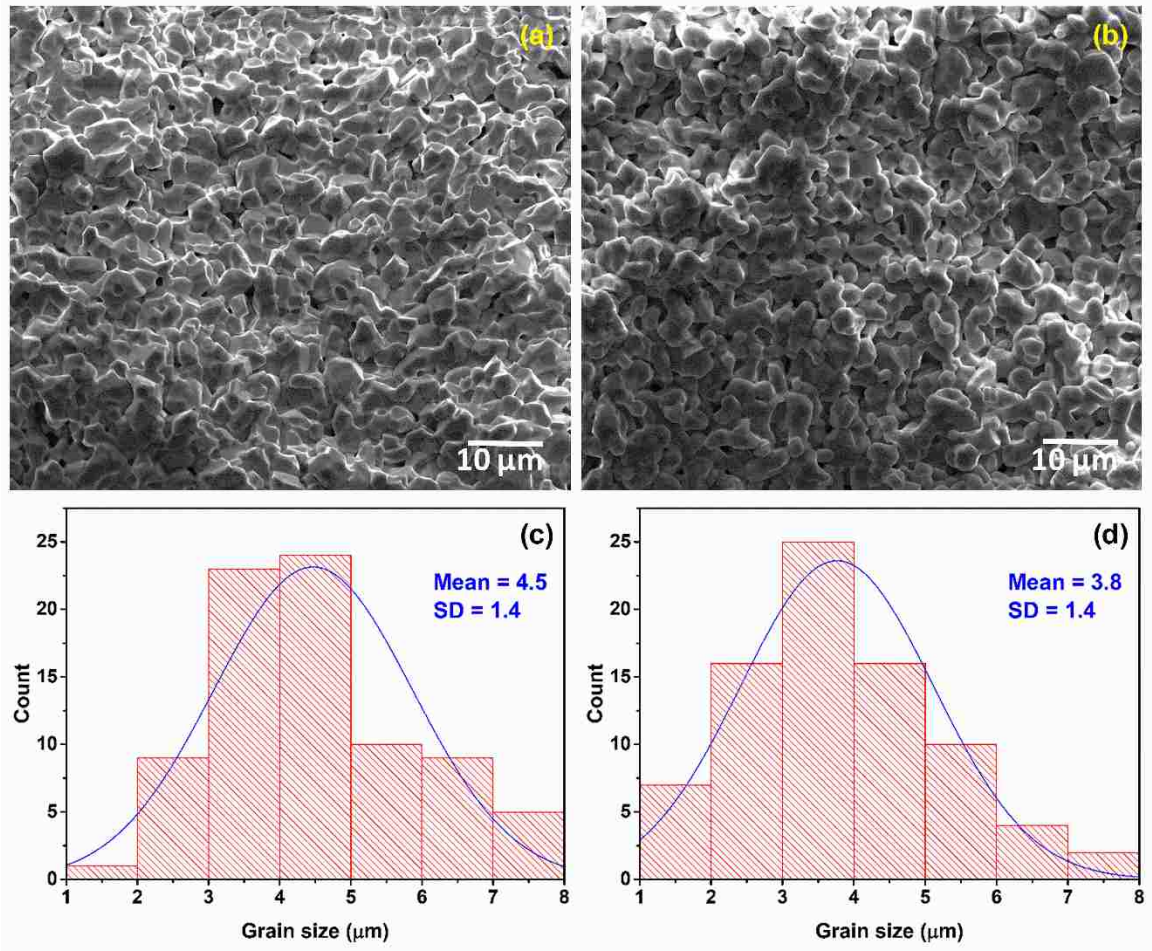

Figure 4.2 SEM fracture surface image of (a) LZO-Ar, and (b) LZO-O_2. Grain size distribution for (c) LZO-Ar, and (d) LZO-O_2.

Transport properties. Impedance spectra of LZO-Ar measured at different temperatures are displayed in Figure 4.3a. Below 450 °C, the spectra is fitted with a typical equivalent circuit $(R_{bulk}Q_{bulk})(R_{gb.}Q_{gb.})(Q_{el})$. Q is the constant phase element and C is calculated based on $C = (QR)^{1/n}/R$, where n=1 corresponds to a perfect capacitor.[74] The first semicircle at high frequencies corresponds to bulk contribution and the second (not fully revealed) at intermediate frequencies is from grain boundary contribution. The low frequency tail (Q_{el}) corresponds to the non-faradic behavior of the interface between the sample and the gold current collector (electrode). At higher temperatures (450 °C-600 °C), the bulk and grain boundary contributions can no longer be distinguished, and the intersection of the high frequency semicircle with the real axis Z' is attributed to the total resistance. Based on the assignments, bulk, grain boundary, and total conductivities, are calculated based on σ =

L/*RA*, where *L* is the thickness, *A* the surface area, and *R* the resistance of the pellet. The Arrhenius plots of LZO-Ar and LZO-O_2 are depicted in Figure 4.3b and the transport properties measured in this study and from literature are summarized in Table 4.1.

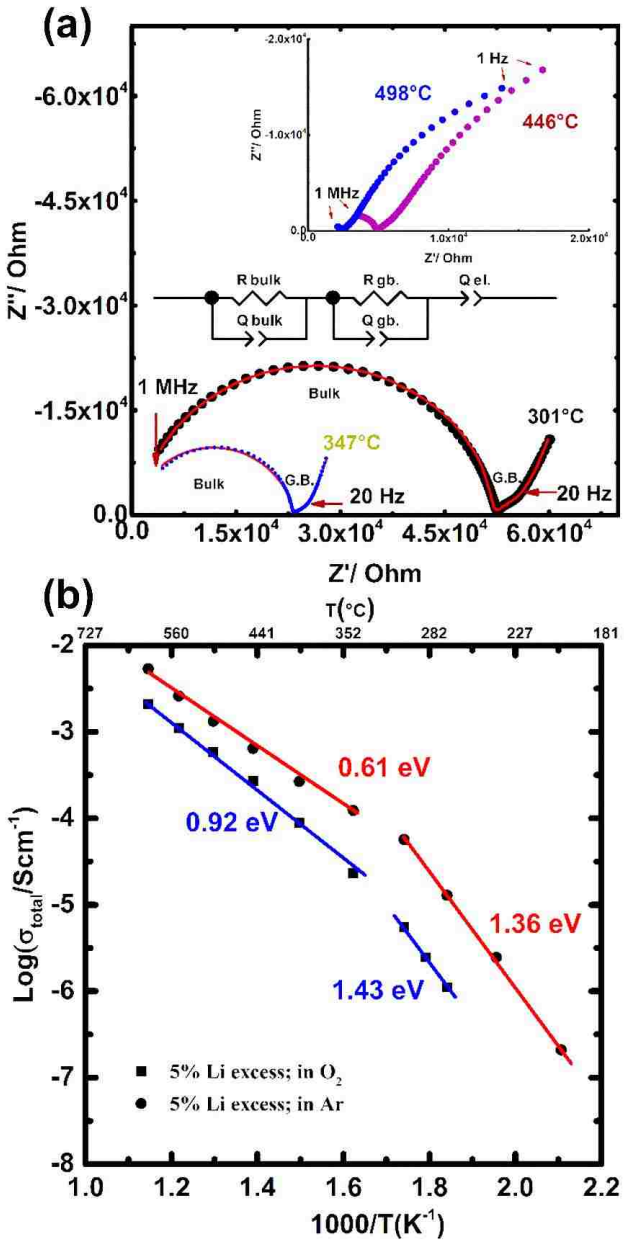

Figure 4.3 (a) Nyquist plots obtained at different temperatures for LZO-Ar. The red lines represent the fitting of the equivalent circuit. (b) A comparison between Arrhenius plots of LZO-Ar and LZO-O_2.

Table 4.1 Summary of transport properties for LZO-Ar and LZO-O_2

Sample /reference	Lithium composition[1]	Relative density (%)	$\sigma_{ion,\ bulk}$ / $\sigma_{ion,\ g.b.}$ (S /cm)	$\sigma_{ion,\ total}$ (S /cm)	E_a (eV)	Temperature range (K)	$\sigma_{electronic}$ (S /cm)
LZO-Ar	1.86	83	$6.0\cdot10^{-5}$ / $1.2\cdot10^{-3}$ (301 °C)	$5.7\cdot10^{-5}$ (301 °C)	0.71 ±0.02	301-600 °C	$2.5\cdot10^{-7}$ (301 °C)
Ref. [78] (sintered in He)	-	69	$\sim10^{-4}$ / $\sim10^{-4}$ (325 °C)	$5.7\cdot10^{-5}$ (325 °C)	0.68 ±0.02	350-465 °C	[+]$\sim10^{-7}$ (301 °C)
LZO-O_2	1.85	84	$2.2\cdot10^{-5}$ / $1.5\cdot10^{-4}$ (343 °C)	$1.9\cdot10^{-5}$ (343 °C)	0.92	343-600 °C	$1.0\cdot10^{-7}$ (343 °C)
Ref. [103] (sintered in O_2)	-	-	-	[2]$\sim10^{-6}$ (343 °C)	0.94	113-457 °C	-

The electronic contribution for both samples is less than 1 %. The activation energy and conductivity values of our LZO-Ar sample are comparable with those reported by Sherstobitova *et al.*[78] However, several differences should be noted. The LZO-Ar sample in this study exhibit negligible grain boundary resistance compared to the bulk resistance, while the reported sample shows blocking grain boundaries ($\sigma_{ion,\ bulk} \approx \sigma_{ion,\ g.b}$) as can be seen in Table 4.1. According to Fleig *et al.*,[74] such blocking grain boundaries are possibly caused by current constriction, which is usually expected in insufficiently sintered samples with poor grain-to-grain contacts. This is consistent with the reported lower relative density (69%) when compared to that (83%) of our sample. In addition, we do not observe an obvious jump-like transition from ionic to superionic conduction at around 467 °C, which is suggested to be caused by redistribution of lithium ions over Li1 and Li2 lattice sites at elevated temperatures.[78] The jump-like behavior is closely related to the Li deficiency in Li_2ZrO_3-type compounds, which can largely be affected by synthesis method and the heat treatment protocol.[113-114] There is a clear discontinuity in the Arrhenius plot of our sample at ~300 °C, below which a higher activation energy (1.36 eV) was extracted. The LZO-O_2

[1] Results from ICP-OES by normalizing Zr to 1.
[2] The conductivity values are approximately estimated from the reported Arrhenius plots.

sample sintered in O_2 experiences a similarly higher activation barrier at lower temperatures (1.43 eV). At higher temperatures, the activation energy is reduced to 0.92 eV, which is consistent with that reported by Hellstrom *et al*. for a LZO sample sintered in O_2.[103]

To conclude, the LZO-Ar sample demonstrates superior ionic conductivity and lower migration barrier compared to LZO-O_2 that is due to the improved Li-ion transport facilitated by additional oxygen vacancies generated during sintering in Ar. To be specific, the oxygen vacancies reduce the unit cell size, and could open faster Li-ion pathways. Naturally, the Ar sintering was used for the synthesis of doped LZO samples.

Doped LZO

Having known that oxygen vacancies benefit Li^+ transport, introducing trivalent or even divalent dopants could be effective strategies to create oxygen deficiency (see Eq. 4.1) and improve the Li^+ conductivity. To prove this hypothesis on the influence of doping, and in turn, oxygen vacancies on Li^+ conduction, we studied the effect of a series of dopant cations (from divalent to pentavalent) introduced to the Zr^{4+} site in LZO.

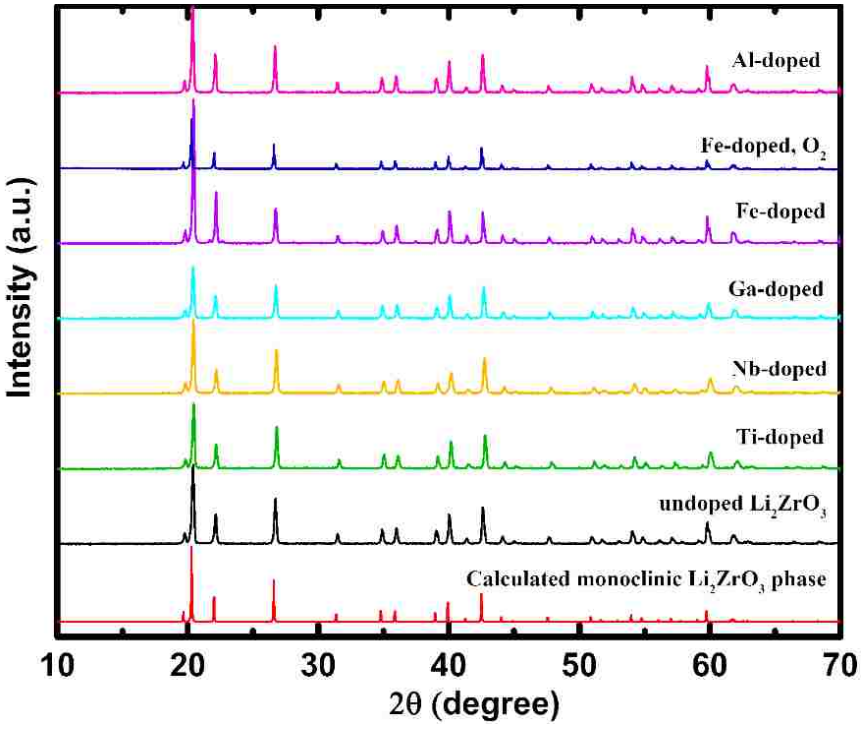

Figure 4.4 XRD patterns of undoped LZO-Ar compared to different cation-doped samples.

Composition and structure. Cations including Nb, Ti, Ga, Fe, Al, and Mg were selected since they have ionic radii smaller than or close to that of 6-coordinated Zr^{4+} (0.72 Å), also their binding energies with oxygen vacancies are relatively high as calculated by Kordatos *et al*.[108] Additionally, Ce^{4+} with 21% larger ionic radius was studied. The doping level for all was 0.1 per formula, and a 5 wt% extra Li was added to compensate the Li loss during synthesis and sintering. The final sintering was always carried out at 1000 °C for 12 hours in Ar flow, unless otherwise stated. Mg and Ce failed to form a single phase, as illustrated in Figure S4.3 (see Appendices). For Ce, obvious peaks from CeO_2 appear in the pattern, indicating the unsuccessful incorporation of Ce into the LZO matrix. However, for Mg the impurity peaks reveal the formation of $Li_6Zr_2O_7$ phase, which implies that Mg entered the LZO lattice but could not stabilize the monoclinic structure of LZO.

Table 4.2 Composition, density, mean grain size, and ionic radii of cation dopants for LZO pellets in this study

Sample	Composition[1]	Relative density[2]	Grain size (μm)	Ionic radius (Å)
LZO-Ar	$Li_{1.865}Zr_{1.000}O_{2.932}$	83.0±0.3	4.5	-
Nb-doped LZO	$Li_{1.928}Zr_{0.900}Nb_{0.101}O_{3.015}$	81.0±0.2	1.5	0.64
Ti-doped LZO	$Li_{1.895}Zr_{0.900}Ti_{0.101}O_{2.950}$	84.7±0.2	4.9	0.61
Ga-doped LZO	$Li_{1.850}Zr_{0.900}Ga_{0.100}O_{2.875}$	85.5±0.2	7.8	0.62
Al-doped LZO	$Li_{1.847}Zr_{0.900}Al_{0.102}O_{2.876}$	85.2±0.3	5.4	0.54
Fe-doped LZO	$Li_{1.867}Zr_{0.900}Fe_{0.099}O_{2.833}$	85.6±0.1	6.8	0.61/0.78[3]

The atomic compositions of both undoped and doped LZO samples measured with ICP-OES are listed in Table 4.2. The ratio between Zr and each doping element is 9:1 as expected from the nominal compositions. Figure 4.4 presents XRD patterns of doped samples, where no impurity peaks were found when compared with the calculated pattern

[1] Calculated ratios by normalizing Zr to 1.00 or 0.90. Oxygen compositions are estimated based on charge balance.
[2] Averaged value from measurements on three pellets for each sample.
[3] Low-spin/high-spin values for six-coordinated Fe (II).

or that of our undoped LZO-Ar sample. Full-pattern fittings of XRD patterns for both undoped and doped samples are provided in Figure S4.4 (see Appendices). Their lattice parameters, unit cell volumes, and ionic radii are also compared in Figure S4.5 (see Appendices). One can see that for the doped LZO samples, their unit cell parameters and volumes are primarily affected by the ionic radii of the doping cations. The amount of lithium deficiencies and oxygen compositions can also contribute to the lattice parameter changes. For example, from Figure S4.5, Nb+5 and Ti+4 have much smaller ionic radii compared to Zr+4, but their lattice sizes are comparable to those of undoped LZO-Ar because they have fewer lithium and oxygen vacancies as demonstrated in Table 4.2.

To confirm the charge states of Ti, Zr, and Fe, XPS spectra were collected for undoped LZO, Ti-doped LZO and Fe-doped LZO pellets as shown in Figure 4.5a-f. The Fe-doped LZO sample sintered in O_2 was also examined for the purpose of comparison. All pellets were polished inside an Ar-filled glovebox before being transferred in vacuum to the XPS chamber to avoid near-surface effects. Depth profiling was not performed as Ar ion etching could cause reduction of Zr^{4+}, Ti^{4+} and Fe^{3+}. The spectra were calibrated against the major C-C peak at 284.68 eV in C1s scan (Figure 4.5b). The other two C1s contributions are assigned to adventitious O-C=O (288.38 eV) and C-Si (281.98 eV) contaminations. For pellets sintered in Ar, besides the major Zr3d doublet corresponding to Zr^{4+} in LZO, there are small peaks at lower binding energies indicating slight reduction of Zr^{4+}, and they disappear as expected in Fe-doped sample sintered in O_2. Similarly, Ti2p scans reveal slight contributions from Ti^{3+}/Ti^{2+} in addition to the dominant $Ti^{4+}2p_{1/2}$ and $Ti^{4+}2p_{3/2}$ peaks. For Fe-doped samples (Figure 4.5f), the one sintered in O_2 shows Fe2p doublet at higher binding energies (711.68 eV and 724.78 eV) corresponding to Fe^{3+}. This two peaks and the satellite contributions shift to higher binding energies for the sample sintered in Ar, because of the reduction to Fe^{2+}. Despite the inevitable noisy photoelectron signals for Fe2p scan, it is still obvious that Fe^{2+} ions are dominant in Fe-doped LZO sample sintered in Ar. The color difference between two powder samples can be seen in Figure S4.6 (see Appendices) where the one sintered in Ar is in light yellow while the one sintered in O_2 is in dark brown. This indirectly reflects the difference in charge state of iron.

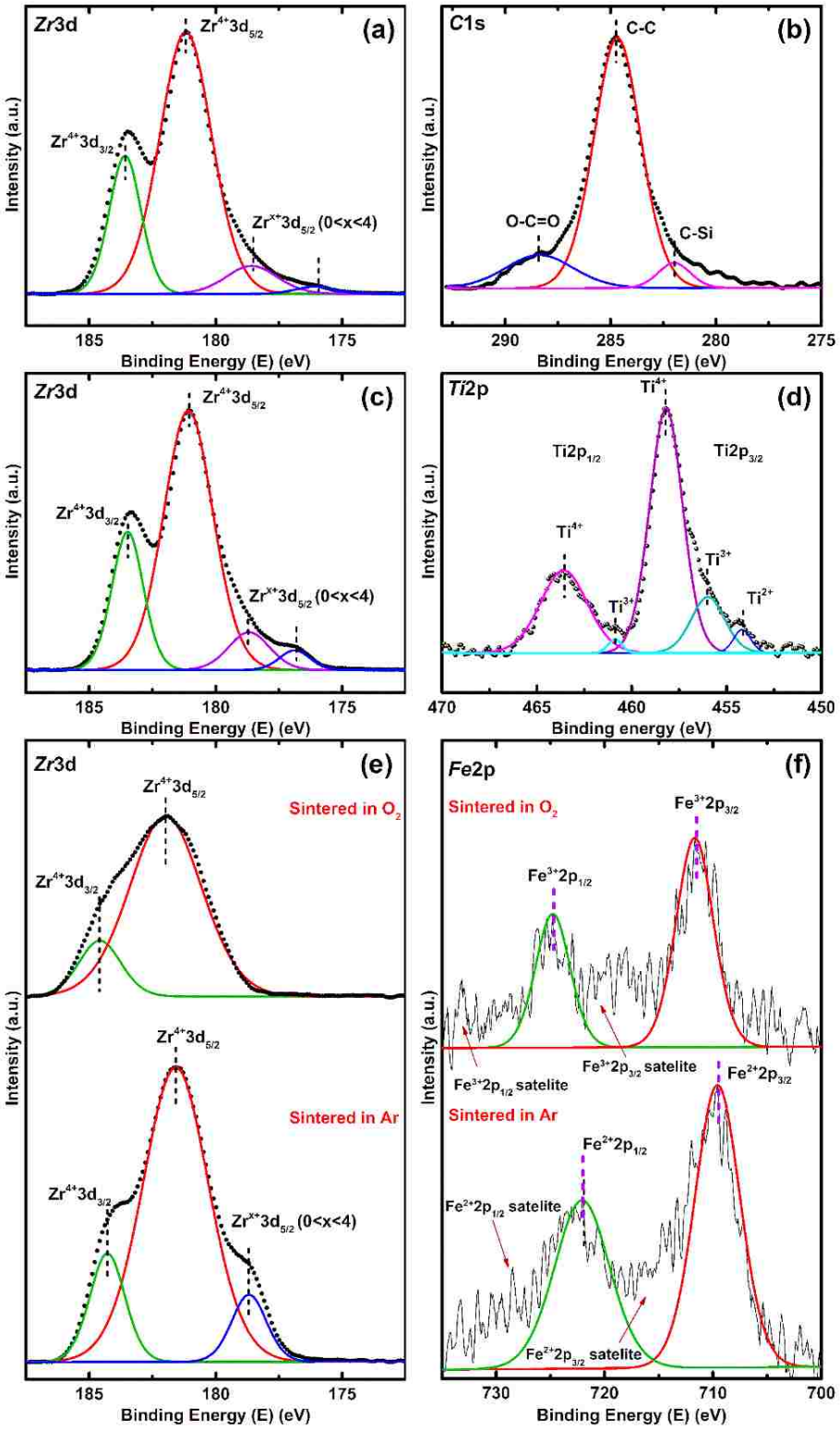

Figure 4.5 XPS spectra of (a-b) undoped LZO-Ar, (c-d) Ti-doped LZO sintered in Ar, and (e-f) Fe-doped LZO pellets sintered in Ar and O_2.

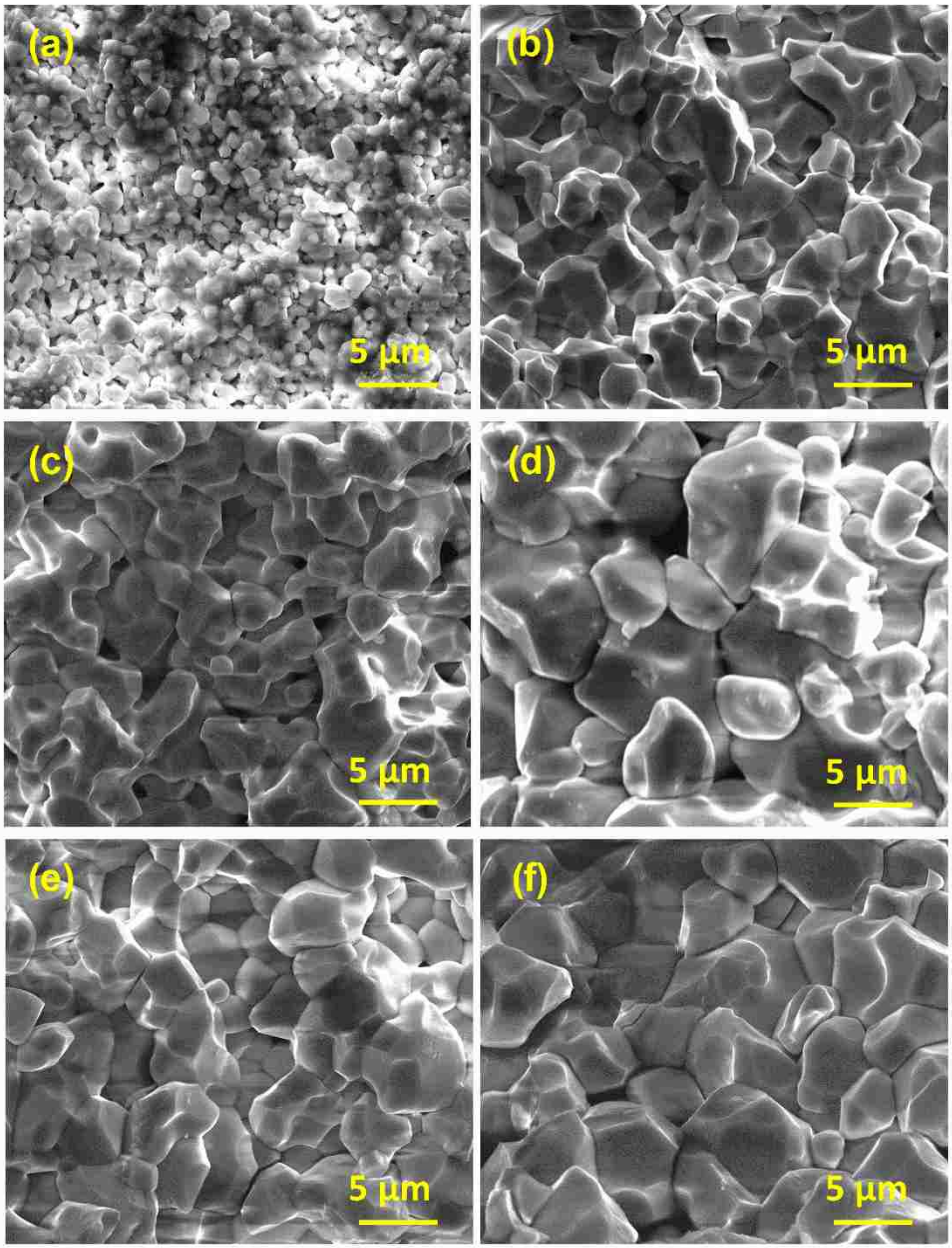

Figure 4.6 SEM fracture surface image of (a) Nb-doped LZO, (b) undoped LZO, (c) Ti-doped LZO, (d) Ga-doped LZO, (e) Al-doped LZO, and (f) Fe-doped LZO.

Figure 4.6 shows the SEM fracture surface micrographs of various sintered pellets. The normal distribution of grain size for each sample is shown in Figure S4.7 (see Appendices), with the mean grain size values listed in Table 4.2. The doped samples, except Nb-doped LZO, have relatively larger grain size than the undoped one. The relative density values show similar trend (summarized in Table 4.2). The Nb-doped LZO with the smallest grain

size exhibits the lowest density, while the other doped samples more or less show rises in relative density. Doping may improve the sintering process of lithium oxides since it can facilitate diffusion through point defects (i.e., lithium vacancies).[73] This possibility is in good agreement with the ionic conductivity data discussed in the following section. In addition, dopants can segregate to grain boundaries and reduce grain boundary mobility. To clarify, EDX maps of undoped LZO-Ar and doped LZOs are shown in Figure S4.8 (see Appendices). Clearly, for every sample, all elements are widely distributed over grains and grain boundaries, and no obvious enrichment of the doping element is found at grain boundaries. However, one interesting phenomenon is that both Al and Ga show some segregation into certain grains where Zr is depleted (Figure S4.8c-d, see Appendices). We suspected that this originates from a small amount of $LiAlO_2$ or $LiGaO_2$ impurities beyond the detection limit of powder XRD. To confirm, we examined the formation of $LiAlO_2$ (PDF# 018-0714) with Al content in samples with 0.2 and 0.3 Al per formula (Figure S4.9, see Appendices). Further investigations are needed to study the effect of such impurities on the matrix phase, which is however out of scope of present study. We did not observe any contributions from a second phase in the impedance spectra of Al- and Ga-doped pellet samples, therefore, such effect, if exist, are negligible for the transport properties.

Transport properties and defect process. The Nyquist plots of Nb/Ti/Al/Fe-doped LZO pellets at 301 °C are presented in Figure 4.7a-d. They show similar features to spectra shown in Figure 4.3a. The equivalent circuit $(R_{bulk}Q_{bulk})(R_{gb.}Q_{gb.})(Q_{el})$ was used to fit all the spectra. A fitting example using Zview2 is given in Figure S4.10 (see Appendices) for Ga-doped LZO and calculated bulk and grain boundary capacitance values are included. As can be seen in Figure 4.7a, the Nb-doped LZO has a grain boundary resistance comparable to the bulk contribution due to its small gain size and thus large grain boundary concentration. The high-frequency response from the sample (bulk + grain boundary) is clearly separated from the low-frequency electrode blocking effect at the frequency of 20 Hz except for Fe-doped LZO. Besides the bulk interception at the highest frequency, the other two semicircles are most probably contributions from different types of grain boundaries (Figure 4.7d). A similar observation was reported for Al-doped $Li_7La_3Zr_2O_{12}$ by Djenadic *et al.*,[115] and they suggested that the presence of different phases could be the reason. To explore the possibility, we collected the high-resolution synchrotron XRD

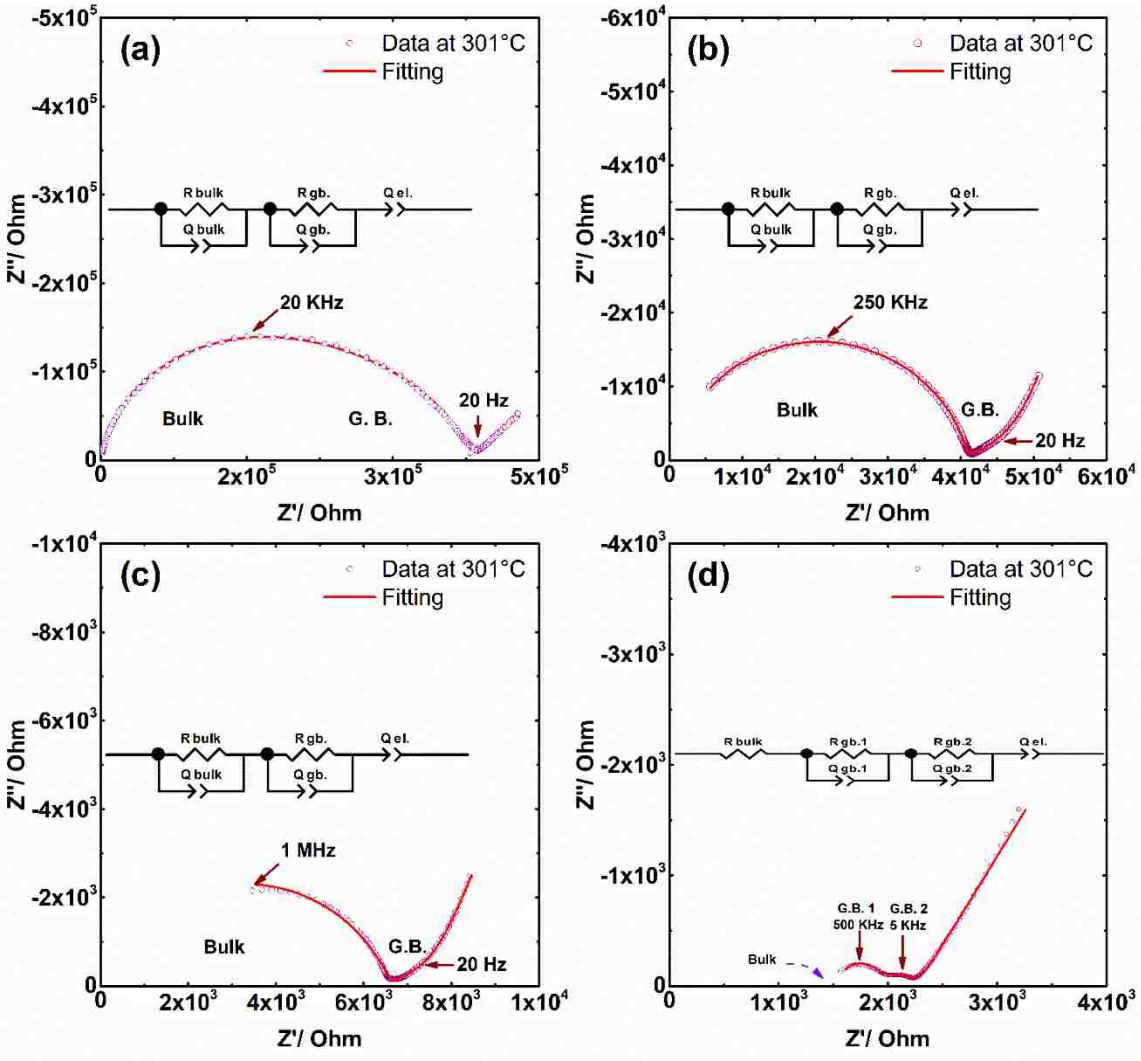

Figure 4.7 Impedance spectra measured at 301 °C in Ar for (a) Nb-doped LZO, (b) Ti-doped LZO, (c) Al-doped LZO, and (d) Fe-doped LZO pellets sintered in Ar.

pattern of the Fe-doped LZO sample as shown in Figure S4.11 (see Appendices). It exhibits a single monoclinic phase (Figure S4.11a) with high-intensity peaks matching perfectly with the calculated Bragg positions. As we plot the cubic root of the intensity versus two theta values (Figure S4.11b), two very weak reflection peaks can be observed at 25.8° and 28.0° matching that of ZrO_2 (PDF# 018-0714) and $Li_6Zr_2O_7$ (PDF# 02-0536) phase, respectively. Additionally, in Fe-doped LZO sample, Fe seems to show enrichments in certain grains (Figure S4.8e, see Appendices) where Zr remains. Therefore, we suggest that the Fe-enriched nonstoichiometric phase and/or the impurity traces (i.e., ZrO_2 and $Li_6Zr_2O_7$) could be the reason for the extra contribution in the impedance spectrum.

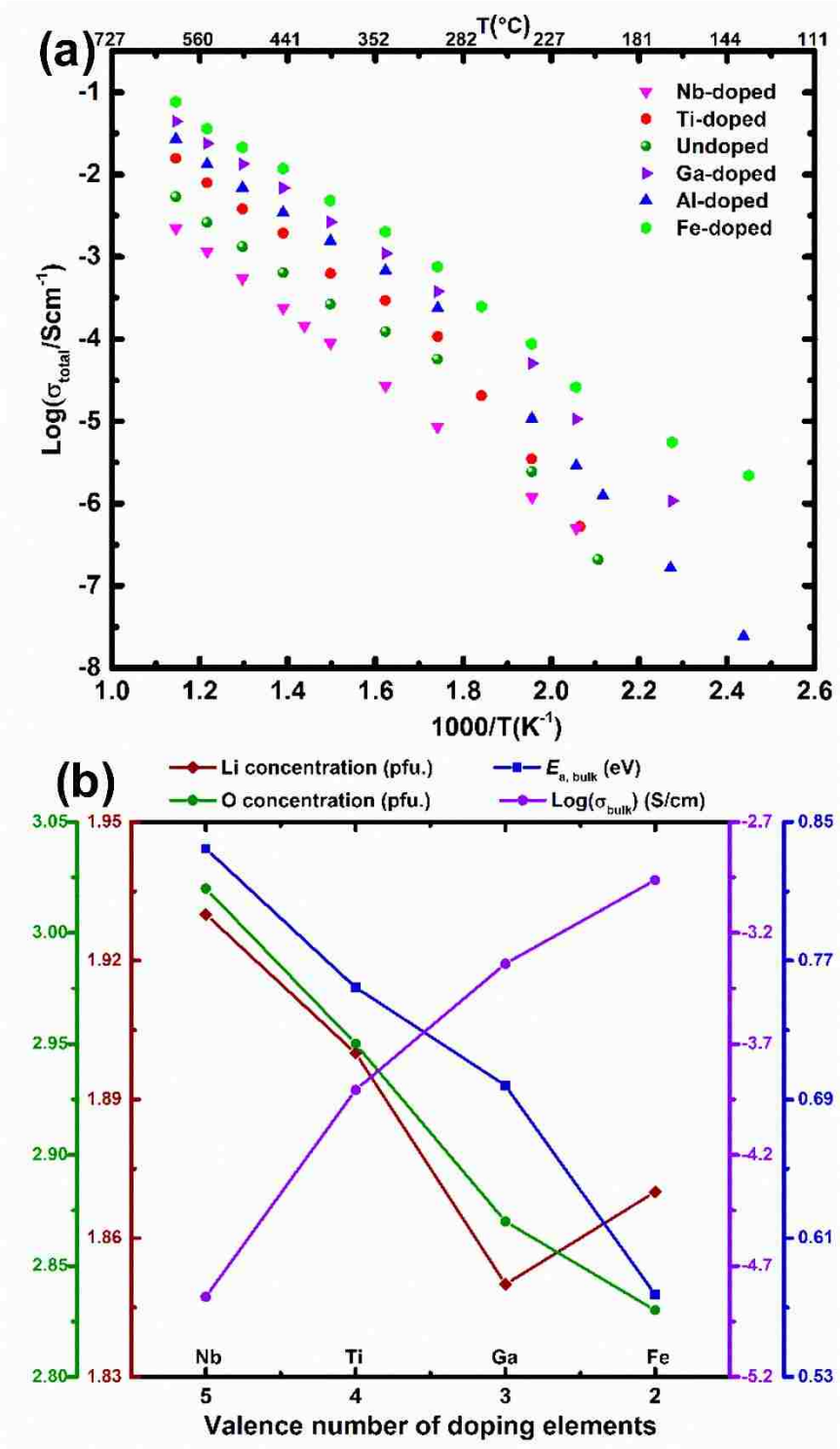

Figure 4.8 (a) Arrhenius plots of total conductivities of undoped and doped LZO pellets. (b) Li and O concentration, bulk ionic conductivities (at 301 °C), and the corresponding activation energies of doped LZO pellets.

The temperature dependences of total ionic conductivities for doped LZOs are plotted in Figure 4.8a. The measured values for undoped LZO-Ar sample are also included to enable comparisons. The total resistance in low-temperature range (below 301 °C) cannot be consistently extracted from AC impedance spectra due to high impedances and thus unavoidable low-frequency noises. The lowest temperature at which conductivity can be reasonably obtained by fitting impedance spectra varies from one sample to another. As previously mentioned for undoped LZO, there is a transition at ~301 °C where the Li^+ migration mechanism changes. This phenomenon can also be seen in the Arrhenius plots of doped samples. Therefore, we focus on the high-temperature range in the following analysis. As can be seen in Figure 4.8a, total ionic conductivities of doped samples follow the order of the valence numbers, as Nb (V)-doped LZO exhibits the lowest and Fe (II)-LZO the highest values. Meanwhile, the migration barrier for total conductivity declines as the valence number decreases. To exclude the effect of grain boundaries particularly for Nb-doped LZO that has the largest portion of grain boundary resistance, the bulk ionic and total conductivities are compared in Table 4.3, where the same trend is revealed. Bearing in mind that the lithium vacancies and oxygen vacancies are important factors in terms of Li-ion transport, the bulk conductivity, the corresponding activation energy, and Li/O concentrations (Table 4.2) are plotted versus the valence number of doping elements in Figure 4.8b. The oxygen concentrations in Table 4.2 are calculated based on Li and Zr compositions measured with ICP-OES with the assumption of charge balance. The comparisons in calculated oxygen concentrations are valid for two reasons. Firstly, all samples considered here were sintered in Ar, therefore the effect of sintering atmosphere on oxygen nonstoichiometry discussed for undoped LZO-Ar and LZO-O_2 samples can be neglected. In addition, electronic conductivities of all samples are very close and are less than 1 % of corresponding bulk ionic conductivities; therefore, electron-holes are minor defects compared to lithium and oxygen vacancies, and their contribution to the charge compensation for lithium loss are comparable and meanwhile negligible. Al-doped LZO is not included since Al+3 and Ga+3 has the same valence number, and their Li, O compositions, bulk conductivities and activation energies of the two samples are very close. Clearly, oxygen vacancy concentration decreases gradually from divalent cation (Fe^{2+}) to pentavalent cation (Nb^{5+}) doping as indicated by the green line.

The defect reactions for doping process with different cations are given as below:

$$Nb_2O_5 \xrightarrow{Li_2ZrO_3} 5O_O^X + 2Nb_{Zr}^{\bullet} + 2V_{Li}' \quad (4.3a)$$

$$TiO_2 \xrightarrow{Li_2ZrO_3} 2O_O^X + Ti_{Zr}^X \quad (4.3b)$$

$$M_2O_3 \xrightarrow{Li_2ZrO_3} 3O_O^X + 2M_{Zr}' + V_O^{\bullet\bullet} \text{ (M = Al or Ga)} \quad (4.3c)$$

$$Fe_2O_3 \xrightarrow{Li_2ZrO_3} 2O_O^X + 2Fe_{Zr}'' + 2V_O^{\bullet\bullet} + \frac{1}{2}O_2\ (g) \quad (4.3d)$$

Kordatos *et al*. calculated via DFT the binding energies between theses substitutional defects (i.e., $Ga_{Zr}^{'}$) and their nearest neighbor oxygen vacancies. This DFT study shows that the formation of oxygen vacancies when divalent and trivalent are incorporated into the Zr site in LZO are energetically favorable. They also showed that the binding of dopant cations with oxygen vacancies becomes weaker from divalent to tetravalent cations.[108] For example, dopant-$V_O^{\bullet\bullet}$ binding is much weaker for tetravalent Ti dopant (~-0.2 eV) than for trivalent Al/Ga dopant (~-4 eV), and divalent Mg dopant has the strongest binding (~-7 eV).[108]. Based on Eq. 4.3a-d, two oxygen vacancies are created when a divalent iron ion replaces a tetravalent zirconium ion, and this number reduces to one for trivalent ions like Ga^{3+} and Al^{3+}, and to zero for tetravalent ions like Ti^{4+}. This can readily explain the rise of oxygen vacancies with lowering valence number of dopants shown in Figure 8b. Considering the usually large formation energy of oxygen interstitial defects in oxides, the lithium vacancies rather than the oxygen interstitials are more likely generated according to Eq. 4.3a to compensate the charge when introducing Nb into Zr sites in LZO. This is agreed by the composition determined for Nb-doped LZO (Table 4.2).

In addition to the doping process discussed above, oxygen vacancies can also be generated during high-temperature synthesis of LZO as shown in Eq. 4.1, where the loss of Li_2O can result in the formation of lithium and oxygen vacancies.[111] Defect interactions, involved in doping and lithium evaporation, can affect the final lithium and oxygen concentrations in the doped LZO materials. However, the valence number of dopants is dominant in determining the oxygen composition, which in turn influences the extent of lithium loss (or the amount of lithium vacancies) that is vital to the Li-ion conductivity.

This is supported by the fact that lithium stoichiometry differs significantly from one doped sample to another with different valence numbers (Figure 4.8b), even though the same 5% lithium compensation and synthesis route are used. On the other hand, Ga and Al resemble each other in terms of Li/O concentration and Li-ion transport properties. Generally, more lithium is lost for Fe, Al, and Ga doping that induces more oxygen vacancies compared to Ti and Nb doping. From a viewpoint of defect chemistry, oxygen vacancies, as a donor, can change the Li stoichiometry of lithium oxides.[109]

Table 4.3 Parameters for electrical conductivities of doped LZO pellets at 301 °C

Sample	$\sigma_{ion,\ bulk}$ (S/cm)	$r=R_{g.b.}/R_{total}$	σ_{ion} (S/cm)	[1]$E_{a,\ bulk}$; $E_{a,\ total}$ (eV)	$\sigma_{eon.}$(S/cm)
LZO-Ar	$5.7\cdot10^{-5}$	4.6%	$6.0\cdot10^{-5}$	0.64; 0.71	$2.5\cdot10^{-7}$
Nb-doped LZO	$2.3\cdot10^{-5}$	40.5%	$8.6\cdot10^{-6}$	0.83; 0.86	$1.8\cdot10^{-7}$
Ti-doped LZO	$1.2\cdot10^{-4}$	13.4%	$1.1\cdot10^{-4}$	0.75; 0.78	$2.4\cdot10^{-7}$
Ga-doped LZO	$7.7\cdot10^{-4}$	17.7%	$3.8\cdot10^{-4}$	0.70; 0.74	$3.3\cdot10^{-7}$
Al-doped LZO	$7.2\cdot10^{-4}$	6.6%	$2.2\cdot10^{-4}$	0.71; 0.75	$3.0\cdot10^{-7}$
Fe-doped LZO	$3.3\cdot10^{-3}$	30.7%	$7.6\cdot10^{-4}$	0.58; 0.70	$3.6\cdot10^{-7}$

As shown in Figure 4.8b, the bulk Li-ion conductivity increases from Nb^{5+} to Fe^{2+}, and the conductivity increase is accompanied by the increase in oxygen and lithium vacancy concentrations for Nb^{5+}, Ti^{4+}, and Ga^{3+}, except for Fe^{2+} where lithium vacancy concentration is lower. From Ga^{3+} to Fe^{2+}, the activation barrier continues to drop (0.71 to 0.58 eV) and the bulk Li-ion conductivity increases, too. Here, lithium vacancy concentration is no longer dominant in Li^+ transport as it falls into the optimized range (~1.85-1.87 Li per formula), and oxygen vacancies play a direct and more determining role by inducing lattice deformation and altering the Li-ion migration pathways. As shown in Fig S5 lattice parameters change with the ionic radii of the doping elements (yellow line), however, there is no clear correlations between the lattice dimensions and Li-ion conductivities of doped LZO samples. For example, the lattice size of Ga-doped LZO is

[1] Extracted from data in the temperature range of 301- 450 °C for bulk and 301- 600 °C for total (bulk + grain boundaries).

different from that of Al-doped LZO, while their Li-ion conductivities are almost in the same level. We previously reported a constructive effect of oxygen vacancies on Li-ion conductivity of the cubic $Li_7La_3Zr_2O_{12}$, where we ascribed it mainly to the trapping between electron-holes and lithium ion vacancies.[116] However, such trapping should only be considered at lower temperatures,[61, 84] as the associated pairs will be released at elevated temperatures, i.e., 200-600 °C in the present study. Further structure analyses (i.e., via DFT modeling, Li NMR, and neutron diffraction) are necessary to fully understand the role of oxygen vacancies in determining the Li-ion mobility.

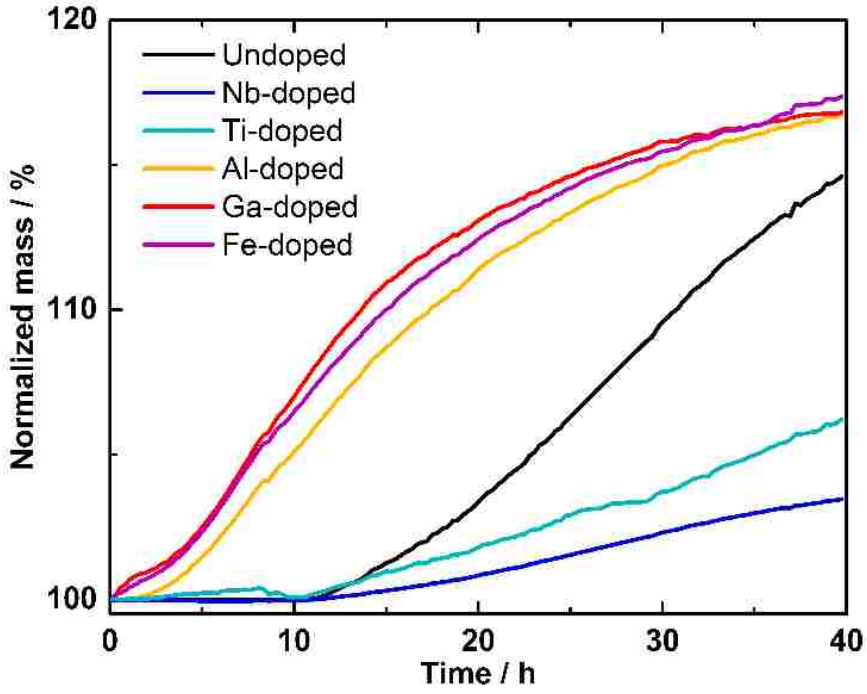

Figure 4.9 Normalized mass traces for both undoped and the Nb-, Ti-, Al-, Ga-, and Fe-doped LZO samples, heated isothermally at 600 °C for 40 h under constant flow of CO_2.

CO_2 absorption. Previous studies on CO_2 capture behaviors of LZO materials have suggested that lower barriers for Li-ion diffusion often lead to higher CO_2 absorption rates in LZO.[102, 111] Here, we examine the carbonation performance of our doped LZO samples at 600 °C under a constant flow of CO_2. The microstructure and phase analysis indicate that impurity traces (i.e., $LiAlO_2$/$LiGaO_2$, and $Li_6Zr_2O_7$) or nonstoichiometric phases can exist in doped samples. They might segregate into grain boundaries and influence the Li-ion diffusion and clearly this will influence CO_2 absorption that also primarily occurs at

surfaces and along grain boundaries., as suggested by Dunstan *et al*.[111] In this case, total conductivity values, compared to bulk ones, are better indicators to look at since Li-ion diffusion through both bulk and grain boundaries should be considered in the CO_2 absorption behaviors of the powder samples. As can be seen in Figure 4.9, CO_2 absorption rates of doped LZOs show dependency on their total conductivities (Figure 4.8a) and the corresponding migration barriers (Table 4.3). Al-, Ga-, and Fe-doped LZO samples exhibit much faster CO_2 absorption than Nb and Ti-doped LZO samples. The Fe-doped LZO sample shows similar absorption rate to those of Ga- and Al-doped LZO materials, which agrees well with their closeness in total conductivities and corresponding activation energies (Table 4.3).

It is noteworthy that the Li-ion diffusion or conduction alone could not determine the CO_2 absorption performance considering the carbonation equilibria:

$$Li_2ZrO_3 + CO_2 \longrightarrow Li_2CO_3 + ZrO_2 . \quad (4.4)$$

Doping can affect the stability of LZO relative to ZrO_2 and Li_2CO_3 and thus will cause the equilibrium to shift. Dunstan *et al*. also observed minimal absorption of CO_2 at 600 °C for Ta- and Nb-doped LZO powders, similar to our cases of Ti- and Nb-doped. It is likely that the Nb/Ta/Ti-doping improves the stability of LZO, which results in shift of the equilibrium in Eq. 4.4 to the left.[111] However, in their study the Y-doped LZO showing the best CO_2 absorption among the three doped samples (Ta-, Y-, and Nb-doped LZO) exhibits the highest activation barrier for Li^+ diffusion estimated from ^7Li relaxation measurements. We propose that the introduction of Y+3 into the Zr+4 sites of LZO, similar to our scenarios of introducing Fe, Al, or Ga dopants, generates oxygen vacancies rather than lithium interstitials indicated by the composition ($Li_{2.05}Zr_{0.95}Y_{0.05}O_3$[111]) they adopted. As a result, Y-doped LZO should have easier Li-ion motion and thus faster CO_2 absorption than Ta/Nb-doped LZO samples.

4.5 Conclusions

In this study, the defect chemistry and transport properties of a series of LZO-based compounds were systematically analyzed. It is shown that oxygen vacancy content is critical to the Li-ion transport in the LZO structure, since it favors the lithium loss and

promotes the formation of lithium vacancies (during synthesis or sintering) that are beneficial for Li-ion conductivity. In addition, oxygen vacancies can by inducing lattice deformation and distortion, lead to the formation of Li migration pathways with lower energy barriers.

In summary, we demonstrate that doping Zr sites with Ti, Al, Ga, and Fe improves the Li-ion conductivity of LZO. Fe-doped LZO shows the highest Li-ion conductivity so far reported for the family of LZO compounds, reaching 3.3×10^{-3} S/cm at 300 °C. Furthermore, our findings from CO_2 absorption measurements suggest that Fe-, Ga-, and Al-doped LZO materials have both superior Li-ion transport properties and higher CO_2 absorption efficiency than pure LZO, and are potentially better candidate absorbents for high-temperature CO_2 capture.

Besides, these doped LZO materials developed here might be also suitable for the other applications, i.e., as coatings for cathodes in Li-ion batteries and as components for glass-ceramic electrolytes, where Li^+ transport is known to be critical.

Chapter 5. Li_2ZrO_3 Modified $LiNi_{0.6}Co_{0.2}Mn_{0.2}O_2$ Cathodes for Lithium-Ion Battery: The Influence of Annealing Atmosphere[1]

5.1 Summary

Layered Ni-rich oxides have attracted much attention for the positive electrode in lithium-ion batteries due to their low cost and high capacity. However, they still suffer from poor cycling and rate performance, especially at high voltage. In this work, $LiNi_{0.6}Co_{0.2}Mn_{0.2}O_2$ powders are surface-modified by a Li_2ZrO_3 coating prepared under either dry air or oxygen. The effect of the coating atmosphere on the electrochemical properties of $Li_2ZrO_3/LiNi_{0.6}Co_{0.2}Mn_{0.2}O_2$ are systematically investigated by multiple structural characterization (synchrotron HRXRD, SEM, TEM, and XPS) and electroanalytical (EIS, SSCV, and GITT) techniques. The Li_2ZrO_3 coating prepared in oxygen is largely amorphous. It not only provides surface protection against the electrolyte corrosion but also enables faster lithium-ion transport at the interfacial regions. Additionally, oxygen atmosphere facilitates Zr diffusion from the surface coating to the bulk of $LiNi_{0.6}Co_{0.2}Mn_{0.2}O_2$, which stabilizes the crystal structure and enhances lithium-ion diffusion. Consequently, $LiNi_{0.6}Co_{0.2}Mn_{0.2}O_2$ cathodes coated with Li_2ZrO_3 in oxygen achieves a significant improvement in high-voltage cycling stability and high-rate performance.

5.2 Introduction

Developing electrode materials for lithium-ion batteries with higher energy density, faster charging, safer operation, lower cost, and longer life is vital for successful implementation of lithium-ion batteries in hybrid, plug-in hybrid, and all-electric vehicles (EV).[3, 117-118] Layered $LiNi_xCo_yMn_{1-x-y}O_2$ materials are surpassing the commercial $LiCoO_2$ material due to their high capacity, relatively low cost (less Co), good cycling stability, and improved safety.[98, 119-120] Although $LiNi_{1/3}Co_{1/3}Mn_{1/3}O_2$ has been commercialized, its capacity of 155 m Ah/g is still low for many EV applications.[121] Layered Ni-rich $LiNi_{1-x-y}Co_xMn_yO_2$ (1-x-y≥0.5) materials have been shown to have even higher reversible capacity (>200 m Ah/g) and high operating voltage (>3.5 V vs. Li/Li^+).[98, 122] For example,

[1] This chapter has been submitted to Electrochimica Acta.

$LiNi_{0.6}Co_{0.2}Mn_{0.2}O_2$ is being commercialized because of its higher Ni content and, therefore, lower cost compared to the commercially available $LiNi_{1/3}Co_{1/3}Mn_{1/3}O_2$ and $LiNi_{0.5}Co_{0.2}Mn_{0.3}O_2$.[123-124] Unfortunately, Ni-rich layered oxides still suffer from many intrinsic structural instabilities brought by high Ni content. Cation disorder between Li^+ and Ni^{2+} ions (Ni^{2+} partially residing in the lithium layers) can block lithium diffusion pathways during the cell operation.[125-126] Additionally, Ni-rich layered oxides tend to lose lattice oxygen in highly delithiated states and transform to the NiO rock-salt phase due to the chemical instability of highly oxidized Ni^{4+}.[127-129] Furthermore, Ni^{4+} formed, especially at high voltages (>4.5 V), can react aggressively with the organic electrolyte and form undesirable side-reaction products, leading to high surface impedance and performance degradation.[130-131] To achieve the long-term cyclability, modifications towards stabilizing the surface and bulk of nickel-rich layered oxides, and facilitating lithium-ion diffusion are needed.[98, 132]

Li_2ZrO_3 has been widely studied as a coating material for high-voltage Ni-rich layered cathode materials due to its relatively high Li-ion conductivity[79, 107] and a good combination of thermal, chemical, and electrochemical stability.[133-135] Wang *et al*.[135] and Xu *et al*.[133] showed enhanced high-voltage (4.6 V vs. Li/Li^+) electrochemical performance of $LiNi_{0.5}Co_{0.2}Mn_{0.3}O_2$ cathode material by Li_2ZrO_3 coating. Sun *et al*.[136] and Liang *et al*.[137] introduced Li_2ZrO_3 as a coating material for $LiNi_{0.6}Co_{0.2}Mn_{0.2}O_2$ and $LiNi_{0.8}Co_{0.1}Mn_{0.1}O_2$, respectively, and reported improvements in rate capability and cycling performance of both cathode materials. Recently, Song *et al*. improved the long-term capacity retention of $LiNi_{0.7}Co_{0.15}Mn_{0.15}O_2$ using Li_2ZrO_3 as the coating agent.[98] In these studies, the heat-treatment of the coating process was conducted in either air[133, 135-136] or oxygen.[98, 137] However, the effect of the atmosphere on the composition/structure of the Li_2ZrO_3 and, subsequently, the electrochemical performance of the cathode materials is still unclear.

The present study aims to explore the effect of coating atmosphere for Li_2ZrO_3 on the electrochemical behavior of the Ni-rich $LiNi_{0.6}Co_{0.2}Mn_{0.2}O_2$ cathode material. A recent work by Schipper *et al*. demonstrated that considerable Zr doping occurs when coating $LiNi_{0.8}Co_{0.1}Mn_{0.1}O_2$ with ZrO_2 by annealing the material at ≥700 °C.[138] The Zr^{4+} ions residing in the bulk can stabilize the layered structure and improve cell performance.[139-140]

Therefore, it is of particular interest for the present study to determine whether the coating atmosphere also affects the Zr diffusion process, and explore the transition from surface Li_2ZrO_3 coating to bulk Zr doping for $LiNi_{0.6}Co_{0.2}Mn_{0.2}O_2$. In the abovementioned work by Sun *et al*., the Li_2ZrO_3 coating on $LiNi_{0.6}Co_{0.2}Mn_{0.2}O_2$ was prepared at 500 °C, which is too low for Zr to diffuse into the $LiNi_{0.6}Co_{0.2}Mn_{0.2}O_2$ lattice according to previous studies,[138, 141] and is also lower than the optimal coating temperatures (650-800 °C[98, 135, 137-138]) used in most studies. We thus pursue two coating atmospheres (dry air and oxygen) at a fixed annealing temperature of 700 °C. Comprehensive studies with the help of multiple phase/structure analysis tools and electrochemical characterization techniques are conducted to address the complex relationships between the coating atmosphere, the structure and composition of Li_2ZrO_3, and their impacts on the electrochemical properties of $LiNi_{0.6}Co_{0.2}Mn_{0.2}O_2$.

5.3 Experimental

Material synthesis. The $LiNi_{0.6}Co_{0.2}Mn_{0.2}O_2$ powders were synthesized by the conventional solid-state method. Li_2CO_3 (Sigma-Aldrich, ≥99%), NiO (Alfa Aesar 99%), Co_3O_4 (Alfa Aesar, ≥99%), and MnO_2 (Alfa Aesar, 98%) in molar ratios of Li: Ni: Co: Mn = 1.08: 0.60: 0.20: 0.20 were uniformly mixed in a mortar. The mixture was calcined at 800 °C for 12 h to decompose fully the carbonates. The calcined powders were milled at 300 rpm for 12 h and dried overnight at 80 °C, and then uniaxially pressed using a pressure of 350 MPa. The pressed pellets were fired at 900 °C for 12 h in air, crushed into powder, and milled and pelletized again for a final annealing at 900 °C for 12 h under oxygen flow. The repeated calcination and milling procedures were used to improve the sample purity. The annealed pellets were crushed and milled at 300 rpm for 3 h to obtain the fine powders for the surface modification or characterizations.

Surface Modification. To prepare Li_2ZrO_3-coated $LiNi_{0.6}Co_{0.2}Mn_{0.2}O_2$ samples, $ZrO(NO_3)_2{\cdot}xH_2O$ (Alfa Aesar, 99.9%; x=1.3 derived with thermogravimetric analysis) and $CH_3COOLi{\cdot}2H_2O$ (Alfa Aesar, 99.9%) with a Li/Zr molar ratio of 2 were used as starting materials. In a typical experiment, 0.083 g $ZrO(NO_3)_2{\cdot}xH_2O$ and 0.067 g $CH_3COOLi{\cdot}2H_2O$ were separately dissolved in 40 mL absolute ethanol, respectively. 5 g $LiNi_{0.6}Co_{0.2}Mn_{0.2}O_2$ powder was first dispersed into the $CH_3COOLi{\cdot}2H_2O$ solution, then the $ZrO(NO_3)_2{\cdot}xH_2O$

solution was slowly dropped into the dispersion. The resultant product was maintained at 70 °C under vigorous stirring until most of the solvent was evaporated. The obtained black powders were collected, dried, and finally calcined at 700 °C for 6 hours under dry air or oxygen flow (both at 10 ml/min) to obtain 1 wt% Li_2ZrO_3-coated $LiNi_{0.6}Co_{0.2}Mn_{0.2}O_2$ samples (herein after referred to LZO-Air or LZO-O_2). Pristine Li_2ZrO_3 powders were synthesized following the same route to examine the formation of Li_2ZrO_3 under different atmospheres.

Structure and composition characterization. Synchrotron-based high-resolution x-ray diffraction (HR-XRD) patterns were collected on beamline 11-BM at the Advanced Photon Source at Argonne National Laboratory. The samples were loaded into Kapton capillaries and rotated during the experiment. The measurement conditions were 295.0 K, a wavelength of 0.41272 Å, and a 2θ step-size of 0.001° from -6.0° to 28.0°. Phase analysis was also conducted using powder x-ray diffraction (Siemens D5000, Cu Kα, 40 kV, 30 mA). The atomic composition of as-synthesized $LiNi_{0.6}Co_{0.2}Mn_{0.2}O_2$ powders was measured to be Li:Ni:Co:Mn = 0.99:0.59:0.20:0.21 using inductively coupled plasma/optical emission spectrometry (ICP-OES; Varian Vista Pro). Powder samples were dissolved in aqua regia and a clear solution was obtained after further digestion of the powder at 95 °C for 3 hours. Same ICP-OES procedures were used to determine the Li/Zr atomic ratios of the pristine Li_2ZrO_3 powders. The surface compositions of the as-prepared and cycled $LiNi_{0.6}Co_{0.2}Mn_{0.2}O_2$ samples were studied using x-ray photoelectron spectroscopy (XPS; Thermo Scientific K-Alpha). XPS samples were prepared inside an Ar-filled glovebox and transferred into XPS chamber without exposing to air using a sample transfer holder. Microstructure was characterized using scanning electron microscopy (SEM; Quanta 250) and transmission electron microscopy (TEM; JOEL 2010F).

Electrochemical testing. The cathode was prepared by mixing the active material, carbon black, and polyvinylidene fluoride (PVDF) homogenously in N-methyl-2-pyrrolidone (NMP) solution in an 80:10:10 weight ratio. Subsequently, the slurry was cast onto an aluminum foil using a doctor blade and dried at 120 °C overnight in vacuum before being punched into small electrode disks. A typical loading of the as-prepared cathode was

4 mg/cm^2. The prepared cathode was assembled with a lithium metal anode (Alfa Aesar), Celgard 2500 separator, and electrolyte (1M LiPF6 in EC: DMC = 1: 1 in volume) into a CR2032 coin-type cell in an Ar-filled glove box. Cyclic voltammetry, charge-discharge cycling (3.0-4.7 V), and electrochemical impedance spectroscopy were carried out using a BioLogic VSP potentiostat. Impedance measurements were conducted using a frequency range from 1 MHz to 0.01 Hz with an AC voltage amplitude of 10 mV. The cell impedance was monitored after the 1st, 10th, and 100th cycles. Before the EIS measurements, all cells were charged to 4.7 V and held for 3 h to reach a quasi-equilibrium state.

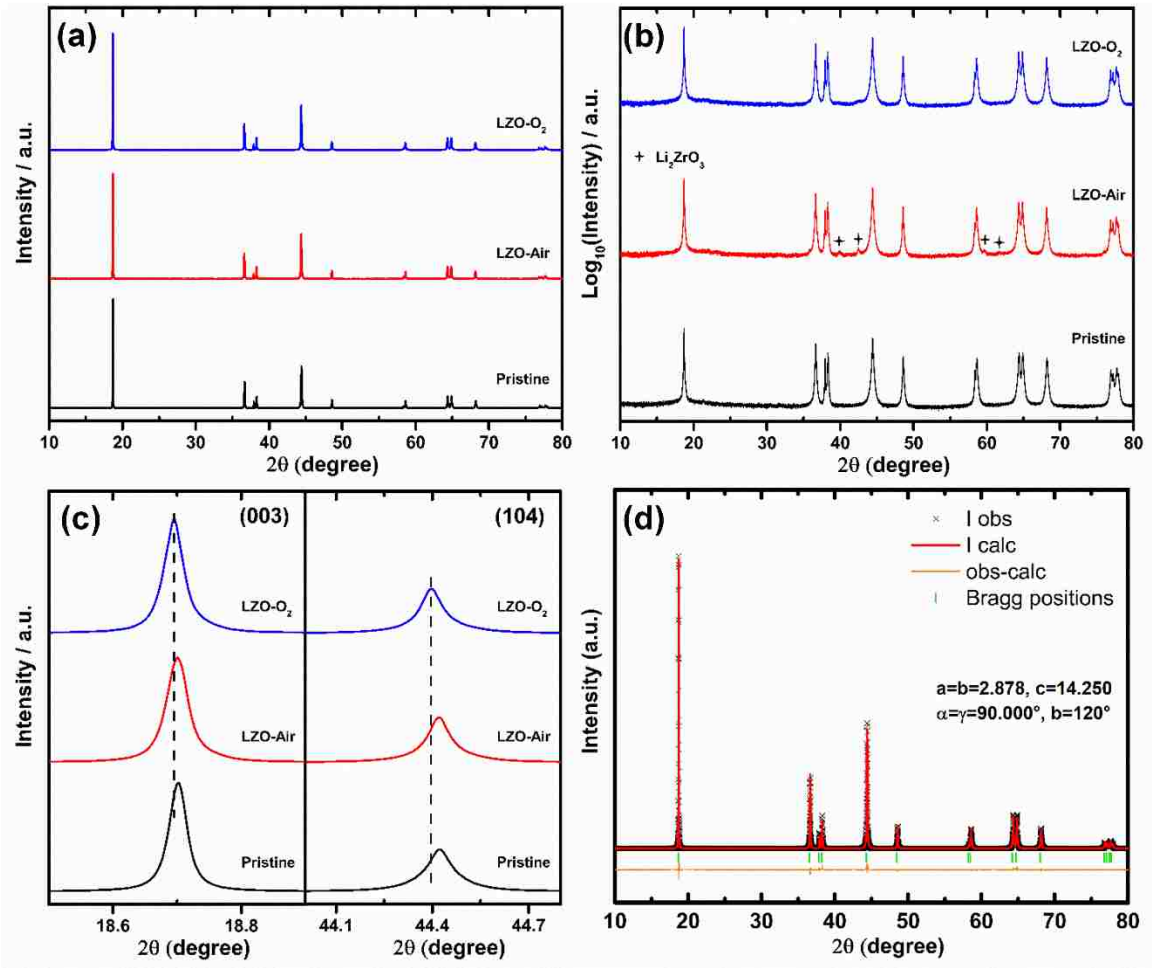

Figure 5.1 (a-c) Synchrotron XRD patterns of the pristine and coated samples. (d) Refinement for the synchrotron XRD pattern of the pristine sample.

5.4 Results and Discussion

Physicochemical characteristics. Figure 5.1 shows the high-resolution synchrotron XRD patterns of the pristine and coated samples. The two-theta values are converted to those corresponding to Cu Kα source (λ=1.54056 Å), while the calibrated wavelength used for synchrotron XRD is 0.412720 Å. The three samples show similar diffraction patterns (Figure 5.1a) with the major peaks matching with those of a layered rhombohedral structure in the space group $R\bar{3}$m. The clear splitting of (006)/(102) and (108)/(110) peaks indicates a well-ordered layered structure. The intensity ratio of (003) and (104) peaks can serves as an indicator of the extent of cation disorder that is critical to the electrochemical properties of layered oxides.[142] Here, the ratios are 2.328, 2.394, and 2.618, respectively for the pristine, LZO-Air, and LZO-O_2 sample, which (I_{003}/I_{104} >1.2) suggests that they each has a good layered structure with low degree of cation mixing.[143] To identify extra crystalline phase(s) from the coating and any impurities, we plot the synchrotron XRD patterns in log scale. As shown in Figure 5.1b, several diffraction peaks corresponding to monoclinic Li_2ZrO_3 phase appear in the pattern of LZO-Air while none is observed for LZO-O_2, informing the coating on the surface of LZO-O_2 is relatively amorphous.

Table 5.1 Lattice parameters obtained from refinement of synchrotron XRD patterns

Sample	Pristine	LZO-Air	LZO-O_2
a (Å)	2.878	2.879	2.882
c (Å)	14.250	14.252	14.268
R_p (%)	7.99	7.24	7.81
R_{wp} (%)	11.57	10.34	10.48

As illustrated in Figure 5.1c, LZO-O_2 shows a slight peak shift to the left, implying its lattice structure has been changed by the surface modification; in contrast, no noticeable peak shift occurs for LZO-Air, indicating little effect of coating on the host structure of LZO-Air. To obtain more insights into this difference, Rietveld refinement using GSAS software [65-66] was performed. The refinement for the pristine samples is shown in Figure 5.1d as an example, with the results for the coated samples displayed in Figure S5.1 (see Appendices). From refinement results summarized in Table 1, the lattice parameters of the

pristine and LZO-Air sample are identical, and they are smaller than those of LZO-O_2. This can be interpreted as that some of the larger Zr^{4+} ions (0.72 Å) have occupied the smaller transition metal ion sites (i.e., Ni^{3+}, 0.56 Å; Co^{3+}, 0.53 Å) in the $LiNi_{0.6}Co_{0.2}Mn_{0.2}O_2$ lattices of LZO-O_2, leading to an enlarged interlayer distance as reflected by the rise in *c*-lattice parameter. Additionally, that LZO-O_2 shows the largest I_{003}/I_{104} ratio among the three samples can be ultimately attributed to the Zr incorporation into the $LiNi_{0.6}Co_{0.2}Mn_{0.2}O_2$ host lattice, which has been suggested to improve structure ordering of Ni-rich layered oxides by lowering Li/Ni cation mixing.[139]

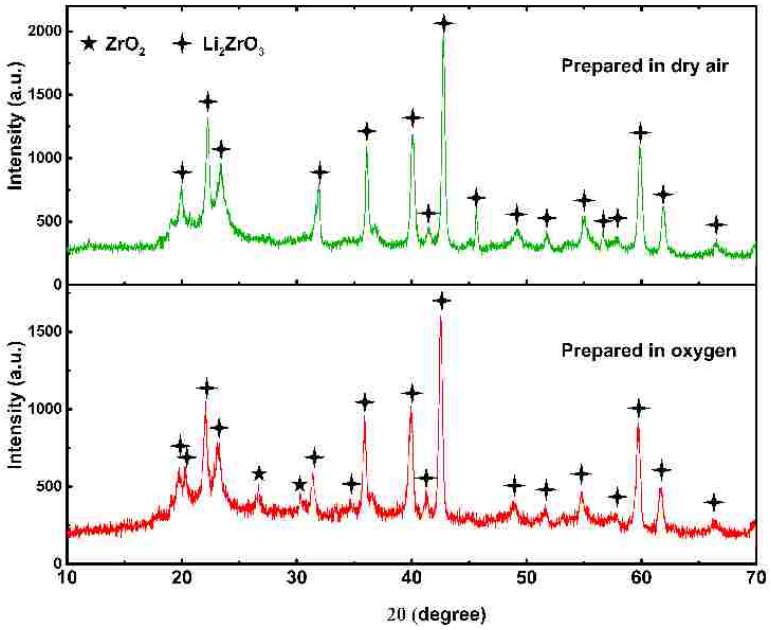

Figure 5.2 XRD patterns of stoichiometric amounts of $CH_3COOLi{\cdot}2H_2O$ and $ZrO(NO_3)_2{\bullet}xH_2O$ mixture heated at 700 °C for 6 hours under (a) dry air and (b) oxygen.

To account for the differences between LZO-Air and LZO-O_2 in the crystallinity of coating and the extent of Zr incorporation, Figure 5.2 compares powder XRD patterns of Li_2ZrO_3 samples prepared in two different atmospheres following the same synthesis route as for coating. The major diffraction peaks for both samples match well with those of the Li_2ZrO_3 phase. However, the sample annealed in dry air shows well-defined Li_2ZrO_3 peaks with higher intensities, while the one treated in oxygen reveals obvious impurity peaks at 26.7° and 30.4° corresponding to ZrO_2 (PDF# 00-002-0464). The ZrO_2 impurity phase most likely rises from the more pronounced lithium loss in the form of Li_2O when synthesizing Li_2ZrO_3 in oxygen atmosphere.[141] To clarify, we conducted ICP-OES

measurements, from which the Li/Zr atomic ratios were determined to be 1.96:1.00 and 1.85:1.00 respectively for Li_2ZrO_3 powders synthesized in dry air and oxygen. We thus propose that lithium deficiency can lead to formation of amorphous phase in the coating, while the intermediate Zr-enriched product (i.e., ZrO_2) can facilitate the incorporation of Zr^{4+} into the $LiNi_{0.6}Co_{0.2}Mn_{0.2}O_2$ underneath via solid-state diffusion. This statement agrees with a recent work by Schipper *et al*., where they found considerable Zr doping occurred in ZrO_2-coated $LiNi_{0.8}Co_{0.1}Mn_{0.1}O_2$ prepared with a similar wet chemical approach followed by annealing the material at ≥700 °C under oxygen.[138] In fact, oxygen, unlike air or inert gases, can facilitate sintering of ceramics by filling pores with pure oxygen that could disappear easily by oxygen migration via lattice diffusion or vacancy transport.[144-145] Moreover, the annealing temperature of 700° C is sufficiently high to enable oxygen-ion migration via the highly mobile vacancies.[86, 146-147] Therefore, the Zr diffusion from the coating to the host can benefit from the oxygen atmosphere where the motions of point defects are accelerated.

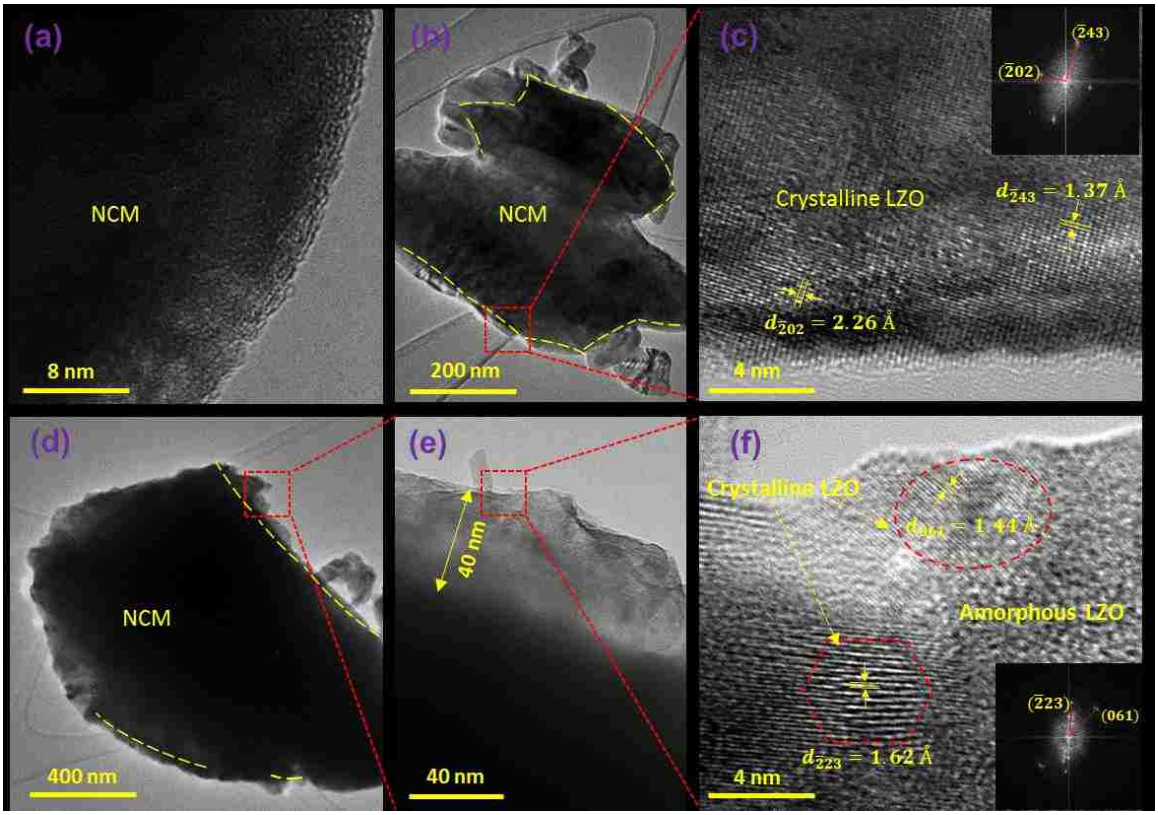

Figure 5.3 TEM images of the (a) pristine, (b-c) LZO-Air, and (d-f) LZO-O_2 sample.

To probe the nano-scale microstructures and collect crystallographic information, TEM investigation was conducted. The pristine sample shows smooth surface (Figure 5.3a), while both coated samples have relatively uniform coating with joined Li_2ZrO_3 agglomerates (~100 nm) as shown in Figure 5.3b and 5.3d. Similar features were observed in $LiNi_{0.7}Co_{0.15}Mn_{0.15}O_2$ samples coated with Li_2ZrO_3 at 650 °C.[98] The high-magnification image (Figure 5.3c) with Fast Fourier Transformation (FFT; inset of panel c) show highly crystalline Li_2ZrO_3 in the coating layer for LZO-Air. However, the surface layer (~40 nm, Figure 5.3e) for LZO-O_2 is largely amorphous, with only some inconspicuous crystallinities completely wrapped by the amorphous regions as can be seen in Figure 5.3f. This agrees well with the synchrotron XRD results (Figure 5.1b) where reflection peaks corresponding to Li_2ZrO_3 crystals appear only in the pattern of LZO-Air. Presumably, such structure configuration with the crystalline domain located within amorphous lattice can potentially facilitate Li-ion transport at the surface considering the faster ion transport through amorphous than crystalline phases.[98, 148]

The surface morphologies of the pristine and coated samples are shown in Figure S5.2a-e (see Appendices). All samples have similar particle shapes with sizes ranging from 1 to 3 microns. The surfaces of the coated samples are obviously different from that of the pristine one, and EDX spectra presented in Figure S5.2d-e reveal the existence of surface coating. In particular, the surface coating of LZO-Air looks fuzzier (Figure S5.2b) while that of LZO-Air (Figure S5.2c) seems relatively more flat and denser. It is likely that the oxygen flow assisted the densification of the surface layer during the annealing process as discussed above.

As shown in Figure 5.4a, the Zr $3d_{3/2}$ (184.28 eV) and Zr $3d_{5/2}$ (181.98 eV) peaks of the coated samples confirm the presence of a Zr coating layer.[134, 149] The peak intensity in the spectrum of LZO-O_2 is significantly lower than that of LZO-Air. To quantify this difference, the surface Zr content for all three samples determined by XPS is shown in Figure 5.4b. LZO-O_2 has a Zr content of 0.14 at.% at the surface, which is close to that reported by Schipper *et al.* for a ZrO_2 coating formed at 700 °C in oxygen,[138] and is much lower than that for LZO-Air (0.37 at.%). The lower surface Zr content of LZO-O_2 is

consistent with the hypothesis that oxygen atmosphere favors the solid-state diffusion of Zr from the surface into the bulk of $LiNi_{0.6}Co_{0.2}Mn_{0.2}O_2$.

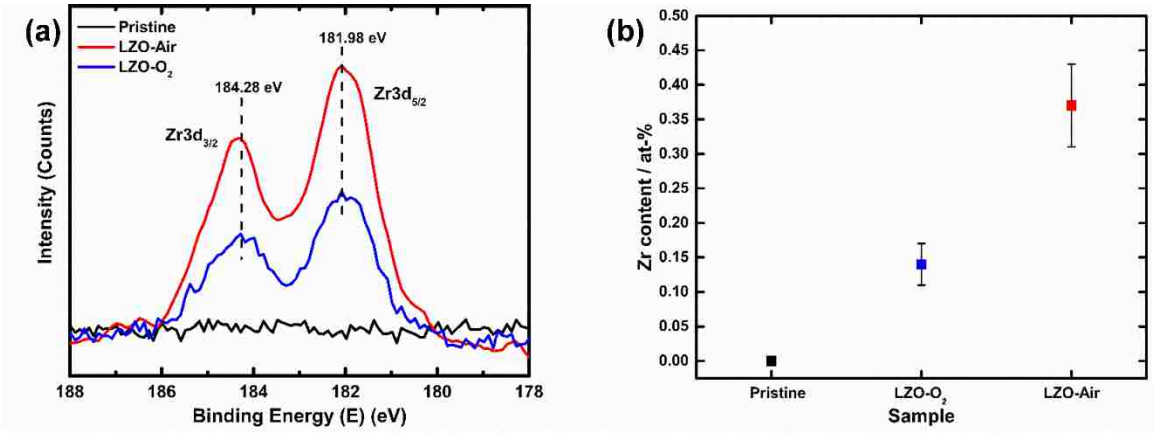

Figure 5.4 (a) XPS Zr 3d scan and (b) the content of zirconium on the surface of the pristine and coated samples measured by XPS.

Electrochemical performances. Figure 5.5a shows the discharge curves of different cycles for all electrodes with their cycling performance compared in Figure 5.5b. From Figure 5.5a, the stability of the discharge voltage plateau during long-term cycling is enhanced by coating. In particular, LZO-O_2 has the least voltage fade in 150 cycles, implying that it suffered the least from electrochemical polarization. At a rate of 0.2C (1C=277 mA/g), each sample delivers an initial capacity over 180 mAh/g. However, after 150 cycles the pristine sample loses almost half of its capacity from 187.9 mAh/g to 95.1 mAh/g. In contrast, the discharge capacity of LZO-O_2 only drops from 211.6 mAh/g to 171.9 mAh/g with the capacity retention of 81.1%, which is also superior to that of the LZO-Air sample (195.8 mAh/g to 131.3 mAh/g, 67.1%). The Li_2ZrO_3 surface coating improves the cycling performance of $LiNi_{0.6}Co_{0.2}Mn_{0.2}O_2$ through stabilizing the interface and facilitating lithium-ion transport at the interfacial regions.[98] This will be further elucidated by the EIS results. Particularly, the better cycling performance of LZO-O_2 can be ascribed to the reduced cation mixing and the stabilized layered structure by Zr incorporation.[139] The rate performances of the pristine and coated samples are shown in Figure 5.5c. The samples were charged and discharged at 0.1C, 0.2C, 0.5C, 1C, 2C, 5C, and then 0.1C again. The discharge capacity decreases with increasing the current density due to the increased polarization at high charge-discharge rates.[150] Most importantly, at all

the current densities tested, LZO-O_2 shows the highest discharge capacity and the best reversibility by delivering a high capacity of 200.0 mAh/g following higher-rate cycling. These significant enhancements in rate capability may originate from the lowered Ni/Li disorder and the improved Li-ion diffusion.

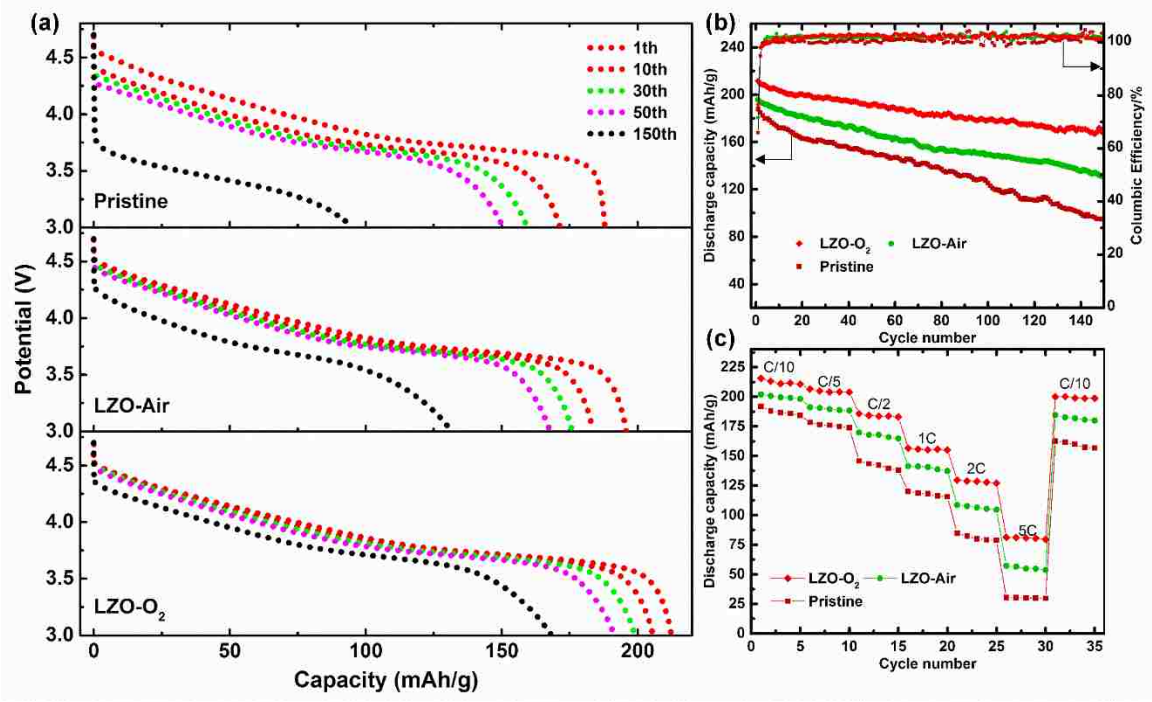

Figure 5.5 (a) Discharge profiles, (b) cycling performances, and (c) rate performances of the pristine, LZO-Air and LZO-O_2 electrode over 3.0-4.7 V (1C = 277 mA/g).

Electroanalytical characteristics. To correlate the electrochemical performance with impedance evolution, EIS measurements were performed. Three semicircles can be observed in each Nyquist plot presented in Figure 5.6a-c, which can be associated, from high frequency to low frequency, with the resistance of solid-electrolyte interphase (R_{SEI}), the electronic resistance of the material (R_e), and the charge-transfer resistance (R_{ct}), respectively.[98, 151] Based on the assignments, the equivalent circuit (Figure 5.6d) was used and fitting values of each component are listed in Table S5.1 (see Appendices). The charge transfer resistances of the coated samples are significantly lower than that of the pristine sample throughout the cycling. This is mainly because of the coating layer that protects the surface from side reactions with the electrolyte thereby reducing the amount of insulating products.[98, 133, 137] More importantly, the sample coated in O_2 has lower resistance values

compared to the LZO-Air sample, which can be explained from two aspects. First, Zr incorporation further stabilizes the surface of $LiNi_{0.6}Co_{0.2}Mn_{0.2}O_2$ and thus mitigates the side reactions with the electrolyte.[139] Also, the more amorphous Li_2ZrO_3 coating suggested by TEM and synchrotron XRD enables faster ion/electronic transport at the interfacial regions.[98] The R_{SEI} follows the same trend as R_{ct}, which implies that (i) the coating layer limits the growth of a resistive SEI layer due to the electrolyte decomposition,[98, 152] and (ii) the SEI components for the LZO-O_2 sample enables the fastest Li^+ transport.[133] Overall, the impedance results are in accordance with the cycling and rate behavior shown in Figure 5.5, and explained, in part, the best electrochemical performance of the LZO-O_2 among the three.

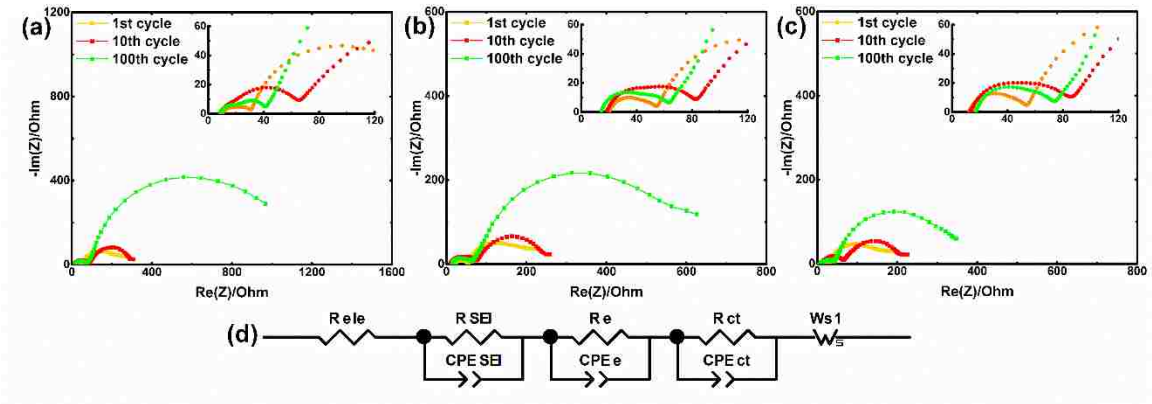

Figure 5.6 Nyquist plots of the (a) pristine, (b) LZO-Air, and (c) LZO-O_2 electrode after different cycles. (d) Equivalent circuit used to fit impedance spectra. R_{ele} is mainly related to the electrolyte solution resistance.

Cyclic voltammetry (CV) was employed to study Li insertion/extraction. Figure 5.7a-c compares the CV profiles of the pristine, LZO-Air, and LZO-O_2 electrode in the first seven scans. The CV curves of each sample show well-defined pairs of anodic (oxidation) and cathodic (reduction) peaks (3.7-3.9 V) corresponding to Ni^{2+}/Ni^{4+} redox couple. The less obvious oxidation peaks at around 4.35 V and reduction peaks at around 4.25 V can be ascribed to the multiphase transitions of hexagonal (H2) to another hexagonal (H3).[136, 153] As summarized in Table S5.2 (see Appendices), the major peaks of the pristine electrode in the first scan appear at 3.896 V and 3.677 V, respectively, giving a potential difference of 0.219 V. This difference drops to 0.138 V in the 2nd scan and rises again to 0.148 V in

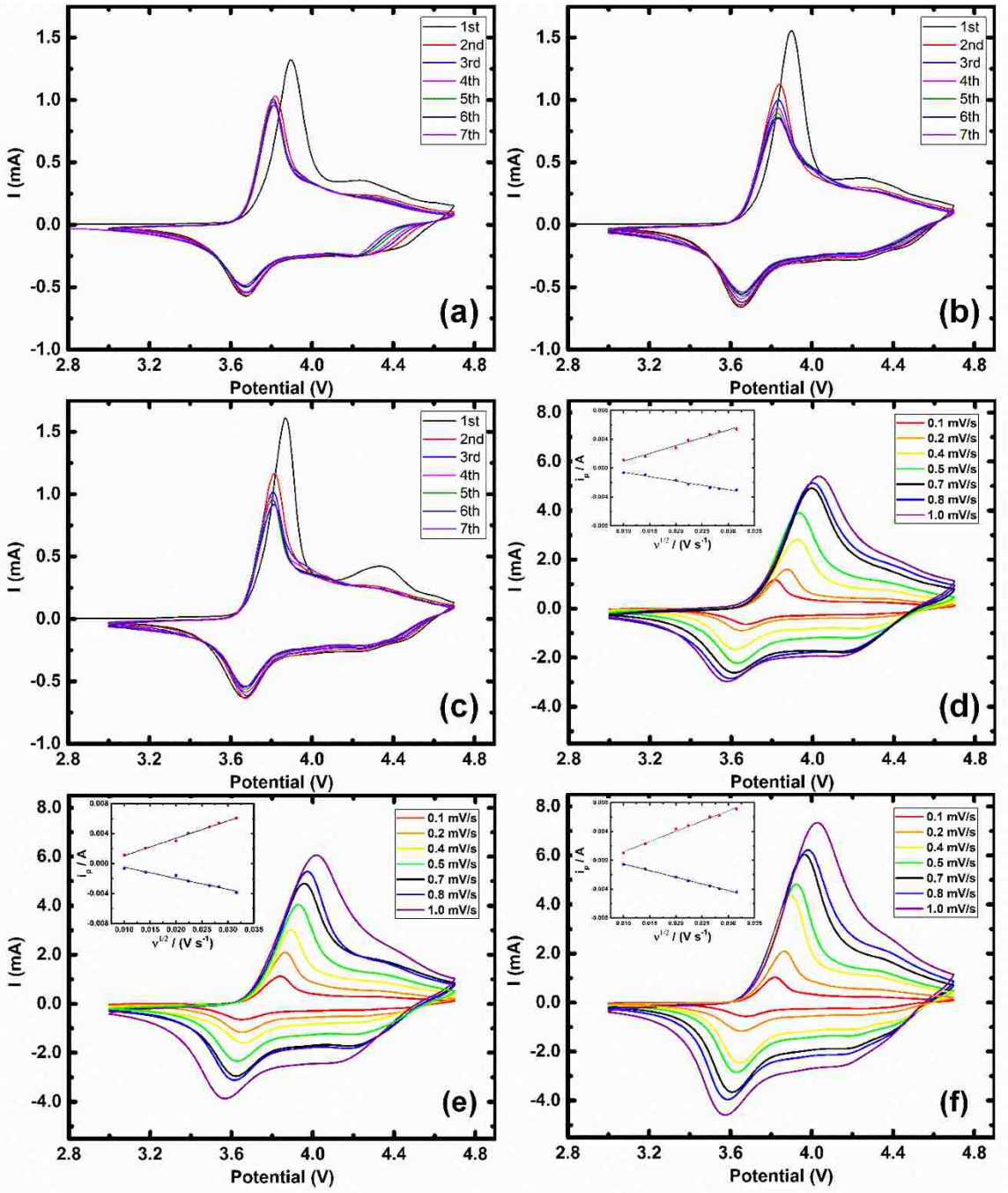

Figure 5.7 Cyclic voltammograms of the (a) pristine, (b) LZO-Air, and (c) LZO-O_2 electrode between 3.0 and 4.7 V at a scan rate of 0.1 mV/s. Cyclic voltammograms of the (d) pristine, (e) LZO-Air, and (f) LZO-O_2 sample at different scan rates (0.1 ~ 1 mV/s) and corresponding voltametric current densities versus square root of scan rate (inset).

the 7th scan. For the LZO-Air sample, the redox peaks continuously shift away from each other, resulting in a large peak difference of 0.174 V in the 7th scan. This informs the

existence of a large electrochemical polarization owing to the low electrical conductivity of the crystalline Li_2ZrO_3 phase. Among the three, LZO-O_2 exhibits the smallest peak differences and the best reversibility during electrochemical cycling, which can be linked to the stabilized electrode surface and fast charge transport through the largely amorphous Li_2ZrO_3 coating layer.[154]

Table 5.2 Lithium diffusion coefficient in the charge and discharge regions

Sample	D_{Li} (cm^2/s) (anodic)	D_{Li} (cm^2/s) (cathodic)
Pristine	4.48×10^{-8}	1.40×10^{-8}
LZO-Air	5.21×10^{-8}	2.10×10^{-8}
LZO-O_2	7.50×10^{-8}	3.25×10^{-8}

To study the electrochemical reaction kinetics, cyclic voltammograms were measured at different scan rates (Figure 5.7d-f). Clearly, for each sample the oxidation peak shifts to the higher potential while the reduction peak shifts to the lower potential with increasing the scan rate. Such peak shifts are indicative of high electrochemical polarization arising when the limited lithium diffusion rates inside the cathode material fail to keep up with the increased CV scan rates.[155] The peak current (I_p) increases with increasing the scan rate (v), and the relationship between I_p and $v^{1/2}$ can be expressed by the following equation:

$$I_p = 2.69 \times 10^5 A n^{3/2} C_{Li^+} D_{Li^+}{}^{1/2} v^{1/2} \quad (1)$$

where n is the charge transfer number, C_{Li^+} is the lithium ion concentration, A is the surface area of the electrode (cm^2), and D_{Li^+} is the chemical diffusion coefficient (cm^2/s) measured by CV. The I_p-$v^{1/2}$ plots presented in Figure 5.7d-f (insets) demonstrate linear relationships as predicted by Eq. (1), and the slope of $dI_p/dv^{1/2}$ can be extracted by fitting the data points. Presuming a homogeneous system and constant D_{Li^+} through the whole phase transition regime, the chemical diffusion coefficients of lithium for the three electrodes can thus be calculated using Eq. (1) and compared in Table 2. The D_{Li^+} values are very close to those evaluated by CV method for $LiNi_{0.6}Co_{0.2}Mn_{0.2}O_2$ in the literature.[155] Lithium diffusion coefficients of the pristine and the coated materials are similar, leading to the conclusion that the coating does not hinder lithium diffusion during the lithiation/delithiation process.

Possible mechanisms for the relatively higher lithium diffusion coefficients of the LZO-O_2 will be discussed in the following section.

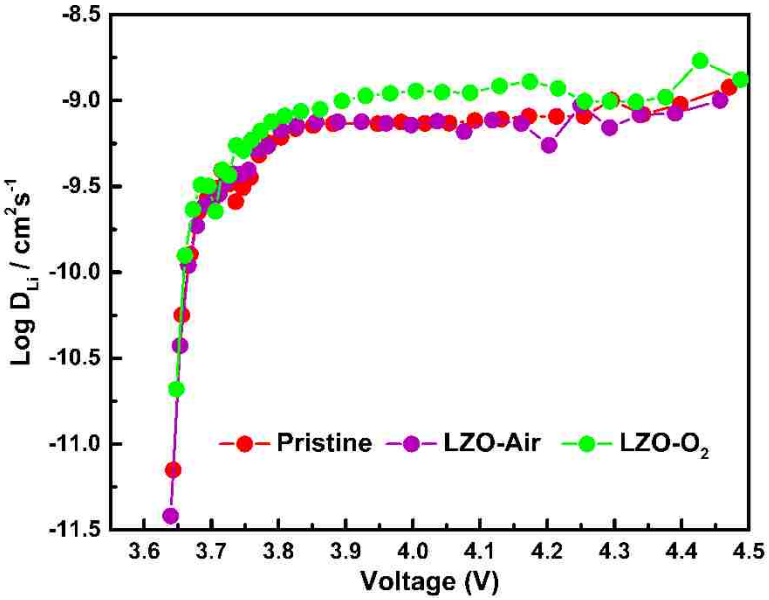

Figure 5.8 The chemical diffusion coefficients of lithium ion derived from GITT measurements.

GITT (galvanostatic intermittent titration technique) was also used to determine the chemical diffusion coefficients of the $LiNi_{0.6}Co_{0.2}Mn_{0.2}O_2$ electrodes. The experimental and analysis details are elaborated in the supplementary (Figure S5.3, see Appendices). As summarized in Figure 5.8, the change of D_{Li}^+ with voltage follows a similar trend for all samples and they vary from 10^{-11} to 10^{-9} cm^2/s, which are close to reported GITT-derived values for $LiNi_{0.6}Co_{0.2}Mn_{0.2}O_2$ materials.[154, 156] In agreement with the results from slow-scan-rate cyclic voltammetry (SSCV) analysis, LZO-O_2 exhibits obviously higher D_{Li}^+ values than the pristine or LZO-Air electrode due to the beneficial effect of Zr doping in facilitating Li-ion migration. Several reasons for such improvement in lithium diffusion coefficients observed for cation (i.e., Na, Mg, and Zr)[138-139, 154, 157] doped $LiNi_{0.6}Co_{0.2}Mn_{0.2}O_2$ materials have been proposed. One is dopants such as Zr and Mg can reduce Li/Ni disorder and stabilize the layered structure. A more important reason could be such larger dopants induce lattice expansion particularly along the *c*-axis, which can enlarge the Li slab space and directly promote the bulk diffusion of lithium ions.[154] As mentioned in the synchrotron XRD analysis, our LZO-O_2 sample had the largest I_{003}/I_{104}

ratio and subsequently the least cation ordering among the three; also, its lattice parameters, particularly *c*, is notably larger than that of the pristine or LZO-Air sample, indicating the expanded interlayer distance. Therefore, we suggest that the superior lithium diffusion behaviors of our LZO-O_2 sample are intrinsically enabled by the Zr-modified $LiNi_{0.6}Co_{0.2}Mn_{0.2}O_2$ structure formed during the coating process.

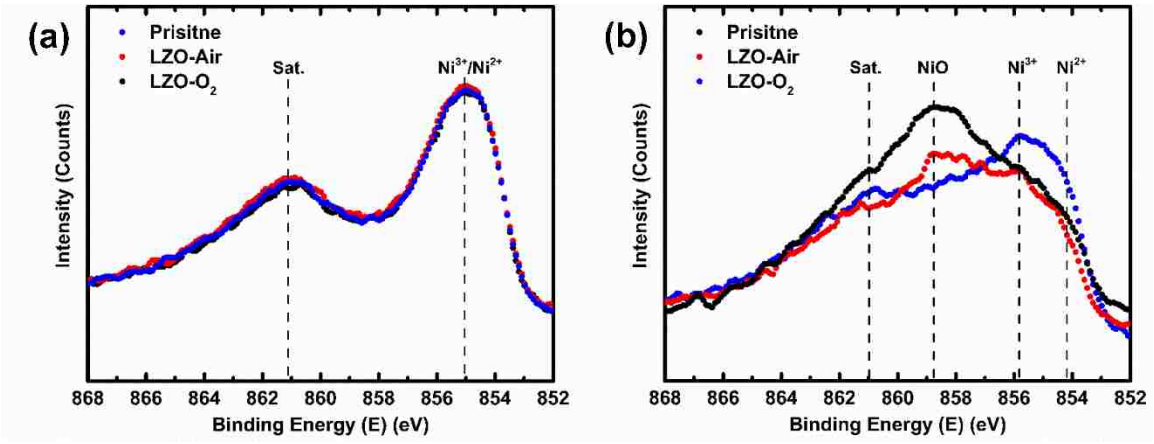

Figure 5.9 XPS spectra (Ni $2p_{3/2}$) of (a) the as-prepared, and (b) 0.2C cycled (150 cycles) electrode samples.

Postmortem XPS analysis. To associate the structural decay during cycling with the degradation in electrochemical performance, surfaces of the cycled electrode materials were analyzed with XPS. The analysis of Co 2p and Mn 2p spectra can be found in the supplementary (Figure S5.4, see Appendices). The Ni 2p spectra of the pristine and coated samples before cycling are shown in Figure 9a, where no obvious differences are observed. The major peak of Ni $2p_{3/2}$ appears at 855.04 eV, which is consistent with that reported in the literature,[134, 137] and indicates that both Ni^{3+} and Ni^{2+} are present.[137] For the cycled electrodes (Figure 5.9b), the two peaks at 854.28 eV and 855.78 eV are attributed to Ni^{2+} $2p_{3/2}$ and Ni^{3+} $2p_{3/2}$, respectively.[158-159] The contribution at 858.88 eV is ascribed to Ni^{2+} in NiO generated from side reactions that occurred due to the chemical instability of highly oxidized Ni^{4+}.[130-131] The fact that NiO constituting the largest proportion of Ni at the surface strongly indicates that the pristine electrode exhibits poor surface stability and has suffered the most from side reactions. Relative to the pristine sample, the NiO contribution is lower in the LZO-Air sample, and is further reduced in the LZO-O_2 sample. Meanwhile, unlike the pristine or LZO-Air sample, the Ni at the surface of LZO-O_2 remains mostly

Ni^{3+}, suggesting that LZO-O_2 possesses the most stable surface structure. This argument is strongly supported by the lowest SEI and charge transfer resistance of LZO-O_2 electrode among the three samples (Figure 5.6). The superior structure stability of LZO-O_2 electrode over LZO-Air further evidences the extra structural stabilization from Zr incorporation besides that provided by the surface coating.

5.5 Conclusions

The $LiNi_{0.6}Co_{0.2}Mn_{0.2}O_2$ cathode materials were synthesized, and a 1 % Li_2ZrO_3 surface coating layer was successfully applied in two different atmospheres. Both surface-modified samples exhibited higher initial capacity, more stable cycling performance, and improved rate capability relative to the pristine one. In particular, the sample coated in oxygen delivered a higher initial capacity (211.6 mAh/g) with better capacity retention (81.1%) after 150 cycles at C/5 and better rate performance than the sample coated in dry air (195.8 mAh/g, 67.1%).

The coating layer prepared in oxygen was largely amorphous while that in dry air contained more crystalline Li_2ZrO_3, as identified by both high-resolution synchrotron XRD and TEM. The former allowed faster lithium-ion transport at the interfacial regions from EIS analysis. More importantly, XPS results revealed that more Zr diffused from the surface into the bulk of $LiNi_{0.6}Co_{0.2}Mn_{0.2}O_2$ when coated in oxygen, with corresponding peak shift and lattice expansion confirmed by synchrotron XRD results. This partial Zr doping can not only mitigate the Li/Ni disorder and improve the structure stability during high-voltage electrochemical cycling, but also enlarge lithium-ion diffusion tunnels thereby facilitating bulk diffusion of lithium ions as suggested by kinetic analysis with CV and GITT. An important finding of this work is that the atmosphere is an important factor to consider for surface modifications of Ni-rich NMC cathodes made by the wet-chemistry method. Specifically, the Li_2ZrO_3 coating formed under oxygen atmosphere at 700 °C realized the dual functions of bulk Zr doping and surface Li_2ZrO_3 modification and significantly enhanced the electrochemical performance of $LiNi_{0.6}Co_{0.2}Mn_{0.2}O_2$ cathode material for high-voltage lithium-ion batteries.

Chapter 6. Conclusion and Future Work

In this dissertation, I have focused on improving transport properties of several representative solid oxide-based materials through fundamental understandings of their defect structures. My main contributions and conclusions are:

(1) We proposed a defect diagram for garnet-type cubic $Li_7La_3Zr_2O_{12}$ describing dependencies of its ionic conductivity and electronic conductivity on temperature and oxygen activity in terms of fundamental defect reactions. Our results suggested that the lithium vacancy-hole pairs can form at intermediate or low temperatures and high oxygen partial pressures, decreasing the Li-ion conductivity of cubic $Li_7La_3Zr_2O_{12}$. In this regard, oxygen vacancies might indirectly benefit the Li-ion conductivity by reducing the amount of electron holes that associated with lithium vacancies. Besides, the lithium vacancy-hole association could be the major barrier for designing single-phase mixed lithium-ionic and electronic conductors.

(2) We demonstrated that by creating oxygen vacancies via cation doping, one could largely improve the Li-ion conductivity of Li_2ZrO_3. For example, Fe (II)-doped Li_2ZrO_3 shows the highest Li-ion conductivity so far reported for the family of Li_2ZrO_3 compounds, reaching 3.3×10^{-3} S/cm at 300 °C. Oxygen vacancies, while long neglected, are critical to Li-ion transport in that: 1) they favor the lithium loss and promote the formation of lithium vacancies during synthesis or sintering; 2) they may induce lattice deformation/distortion that leads to the formation of easier Li migration pathways.

(3) We surface-modified $LiNi_{0.6}Co_{0.2}Mn_{0.2}O_2$ cathode material with a Li_2ZrO_3 coating prepared under dry air and oxygen, and systematically investigated the effect of coating atmosphere on their electrochemical behaviors. The Li_2ZrO_3 coating prepared in oxygen is mostly amorphous. It not only provided surface protection against the electrolyte corrosion but also enabled faster lithium-ion transport. Additionally, oxygen atmosphere facilitated Zr diffusion from the surface coating to the bulk of $LiNi_{0.6}Co_{0.2}Mn_{0.2}O_2$, which stabilized the crystal structure and enhanced lithium ion diffusion. Consequently, $LiNi_{0.6}Co_{0.2}Mn_{0.2}O_2$ cathodes coated with

Li_2ZrO_3 in oxygen achieved a significant improvement in high-voltage cycling stability and high-rate performance.

The present research opens a future direction in designing mixed Li-ion, electron-conducting materials for emerging ionic devices, i.e., composite cathodes that can provide both electronic and ionic paths in solid-state batteries. Since a single-phase material may suffer from the intrinsic association between electron holes and lithium vacancies, two-phase composites should be considered. Secondly, we demonstrated oxygen vacancies could improve Li-ion transport in Li_2ZrO_3 by increasing lithium vacancy concentration. However, the role of oxygen vacancies in promoting Li-ion mobility, i.e., by opening fast Li-ion migration pathways, is unclear. This might be addressed with the help of atomic-level structure analysis such as DFT modeling, Li NMR, and neutron diffraction. Furthermore, it will be interesting to utilize this defect engineering strategy of tuning oxygen vacancy concentration in improving the Li-ion conductivities of other Li oxides-based solid electrolytes that are promising for all-solid-state lithium-ion battery applications. Since we showed pure oxygen is better than dry air as the atmosphere for applying Li_2ZrO_3 coatings on $LiNi_{0.6}Co_{0.2}Mn_{0.2}O_2$ electrode materials, it may be interesting to further investigate the oxygen partial pressure effect on the effectiveness of Li_2ZrO_3 coatings on high-capacity electrode materials.

Appendices

Supplementary Information for Chapter 3

Figure S3.1 SEM micrographs of the fracture surface of sintered pellets. From left to right: 10LLZO, 15LLZO, and 20LLZO pellet.

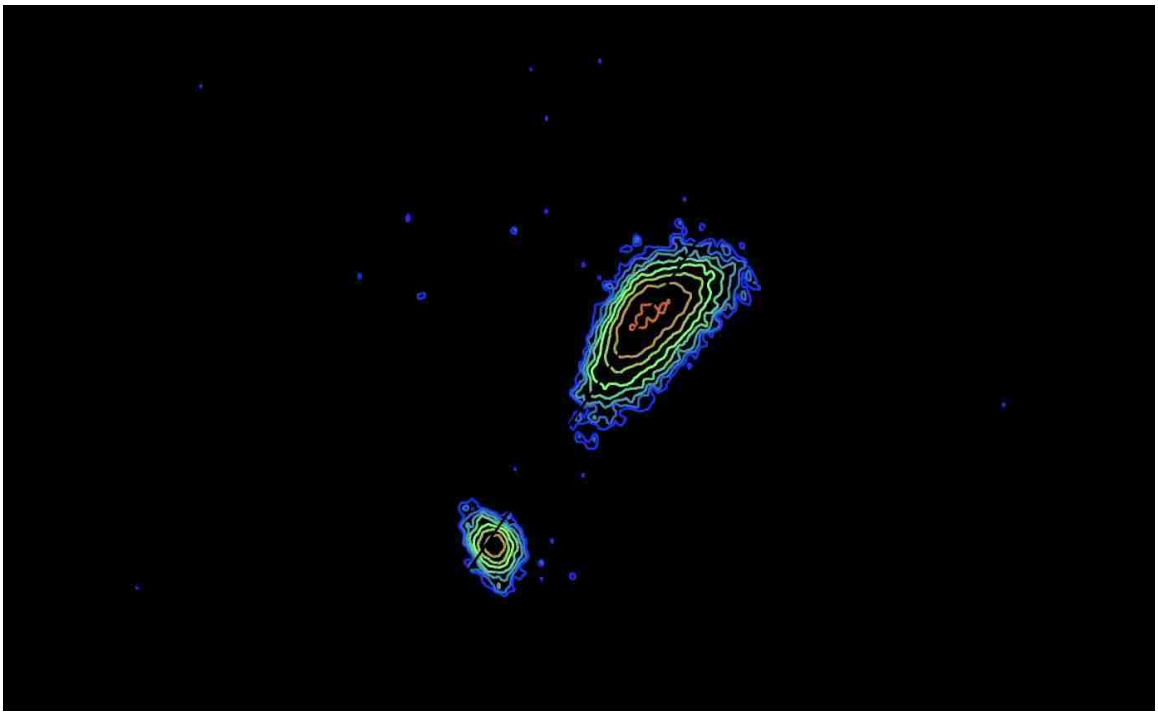

Figure S3.2 ^{27}Al MQMAS NMR spectrum of the 10LLZO sample.

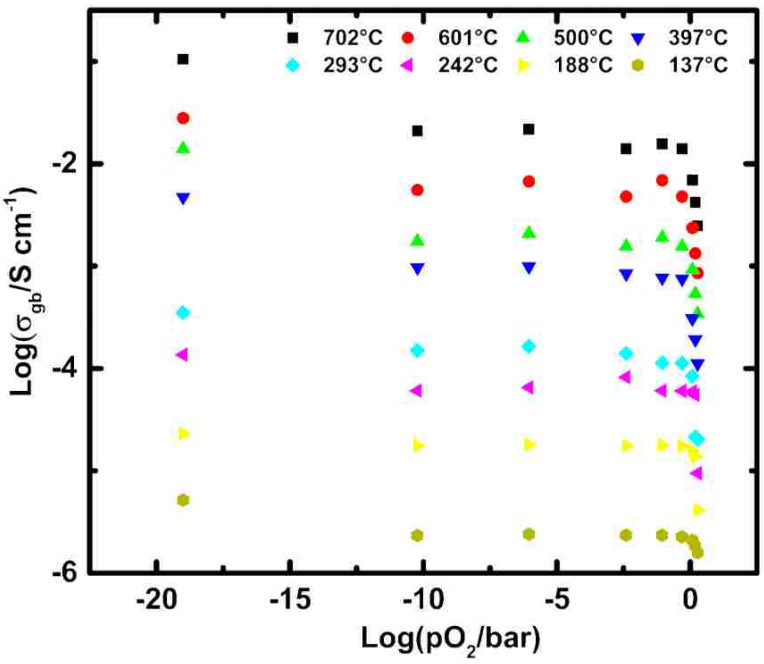

Figure S3.3 The change of total conductivity for the 10LLZO pellet measured with AC impedance spectra as a function of oxygen partial pressure.

Supplementary Information for Chapter 4

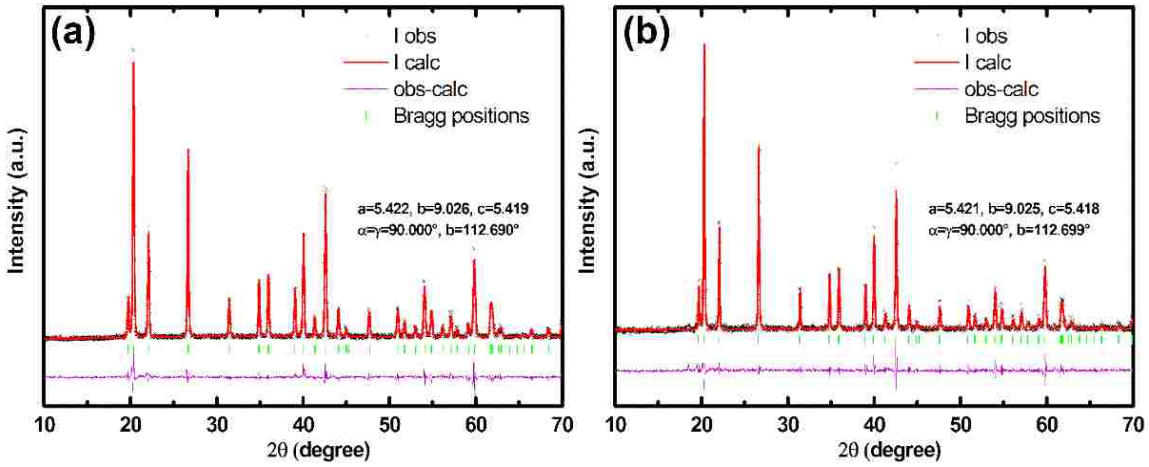

Figure S4.1 Full-pattern fittings for XRD patterns of pulverized (a) LZO-O_2 pellets, and (b) pellets after calcination at 950 °C/10 h in air right before sintering.

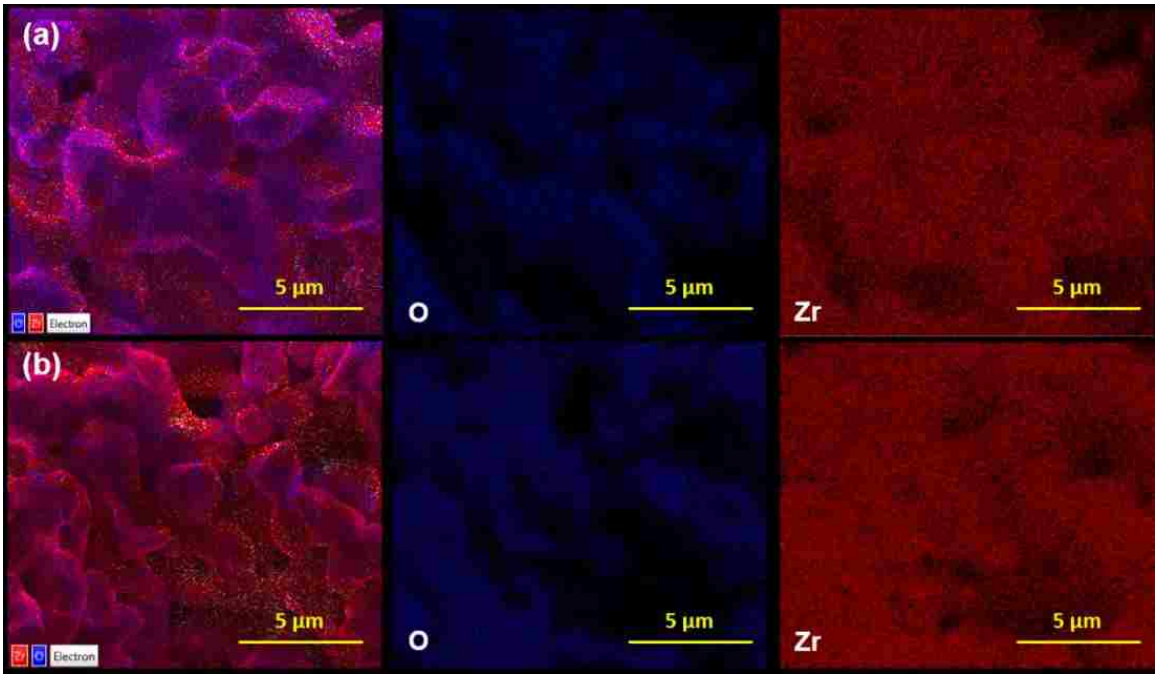

Figure S4.2 EDX composition mappings for (a) LZO-Ar and (b) LZO-O_2.

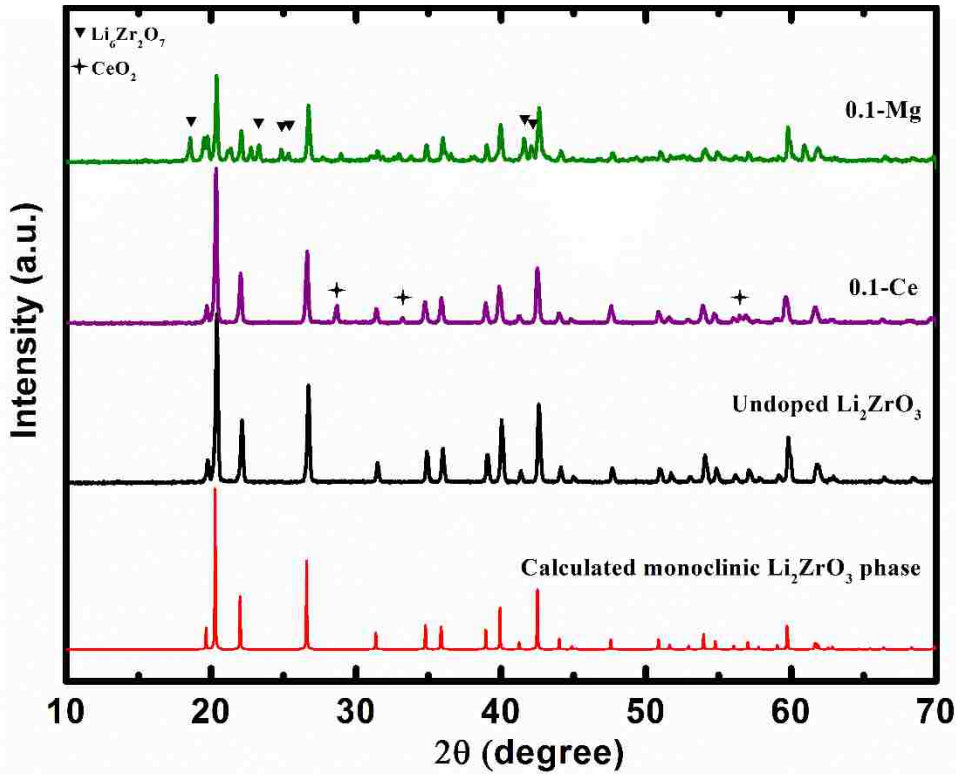

Figure S4.3 XRD patterns of powders from doping attempts using Mg and Ce.

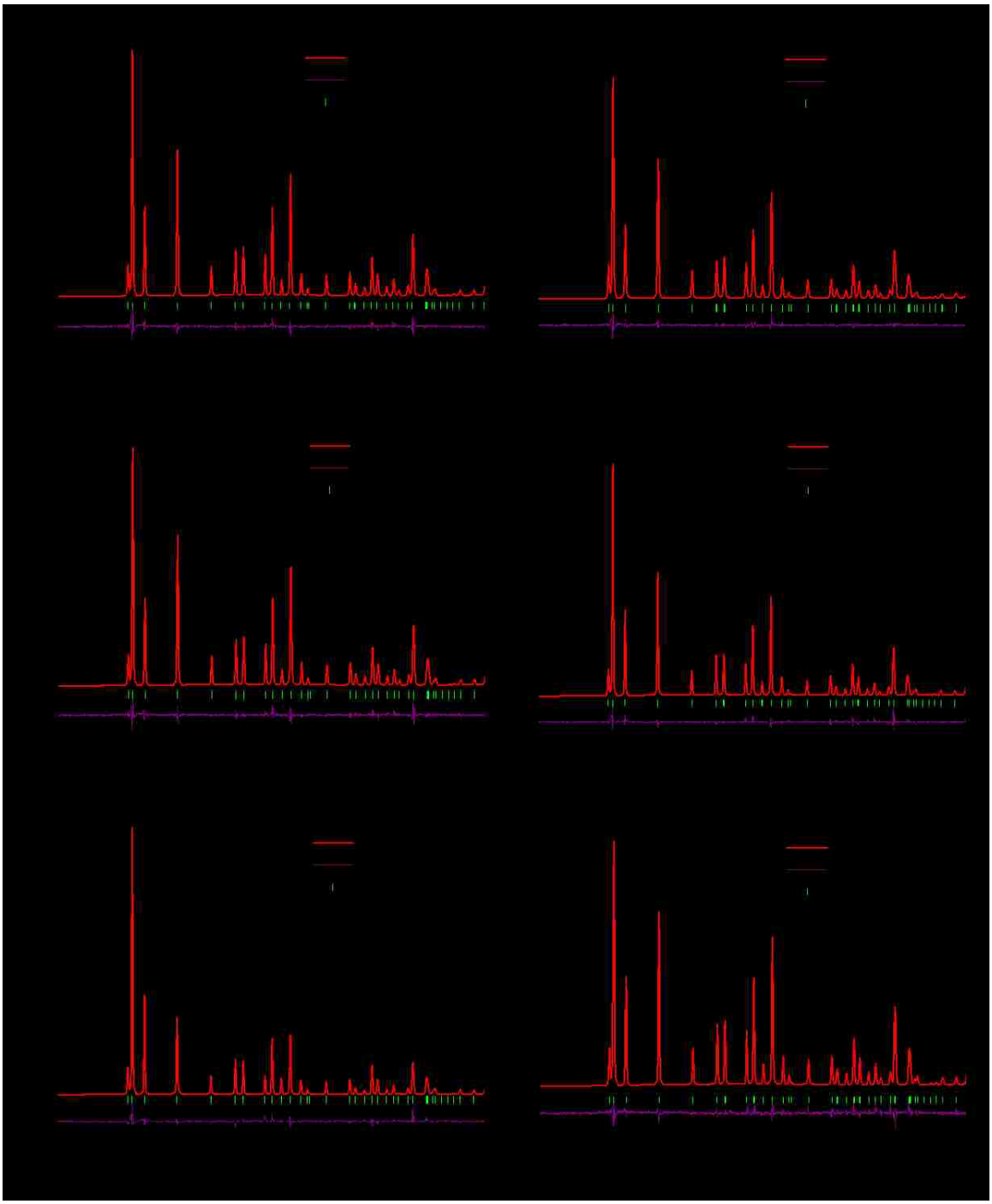

Figure S4.4 Full-pattern fittings for XRD patterns of pulverized (a) LZO-Ar pellets, (b) Nb-doped LZO pellets, (c) Ti-doped LZO pellets, (d) Al-doped LZO pellets, (e) Ga-doped LZO pellets, and (f) Fe-doped LZO pellets.

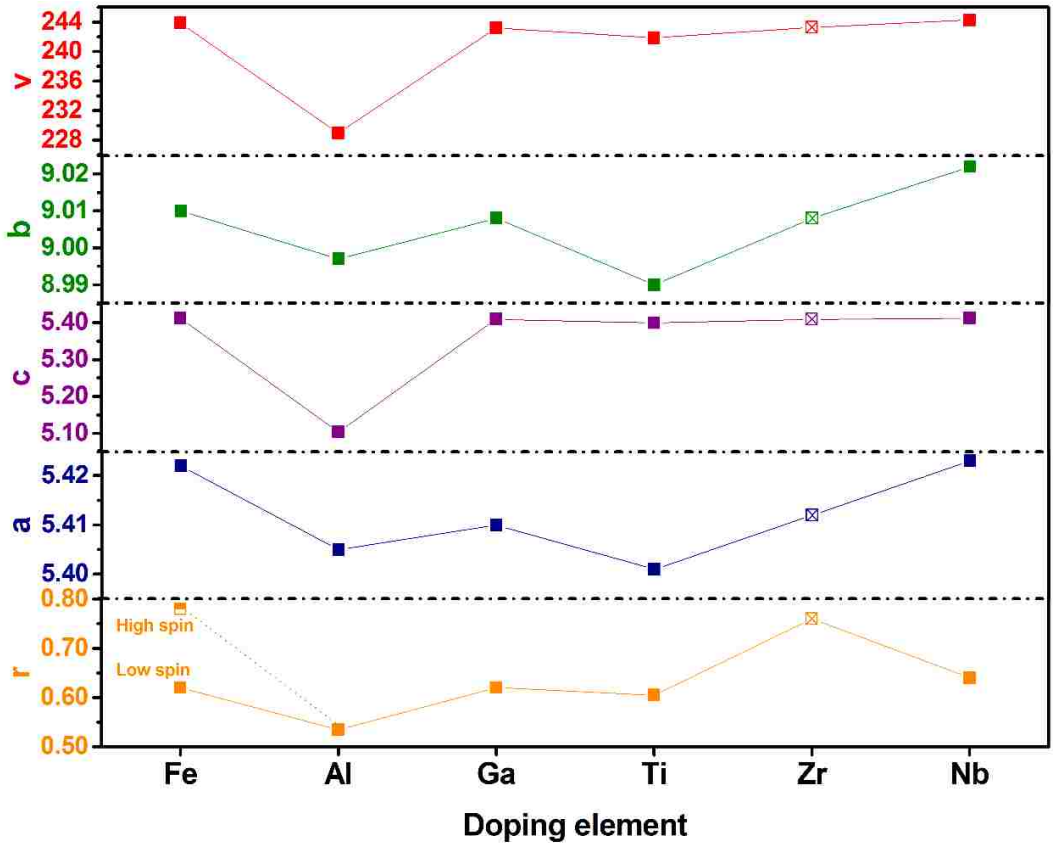

Figure S4.5 Plots of lattice parameters and unit cell volume for different doped LZO samples versus doping elements. The bottom line shows the plot of Shannon ionic radii for Fe^{2+}, Al^{3+}, Ga^{3+}, Ti^{4+}, and Nb^{5+} in 6-coordinated environment. The ionic radius for low spin state is used for Fe^{2+}. The unit for *a*, *b*, *c*, and *r* is angstrom, and for $v=a\cdot b\cdot c\cdot\sin\beta$ is $angstrom^3$.

Figure S4.6 Powders crushed from (a) Fe-doped LZO pellets sintered in Ar, and (b) Fe-doped LZO pellets sintered in O_2.

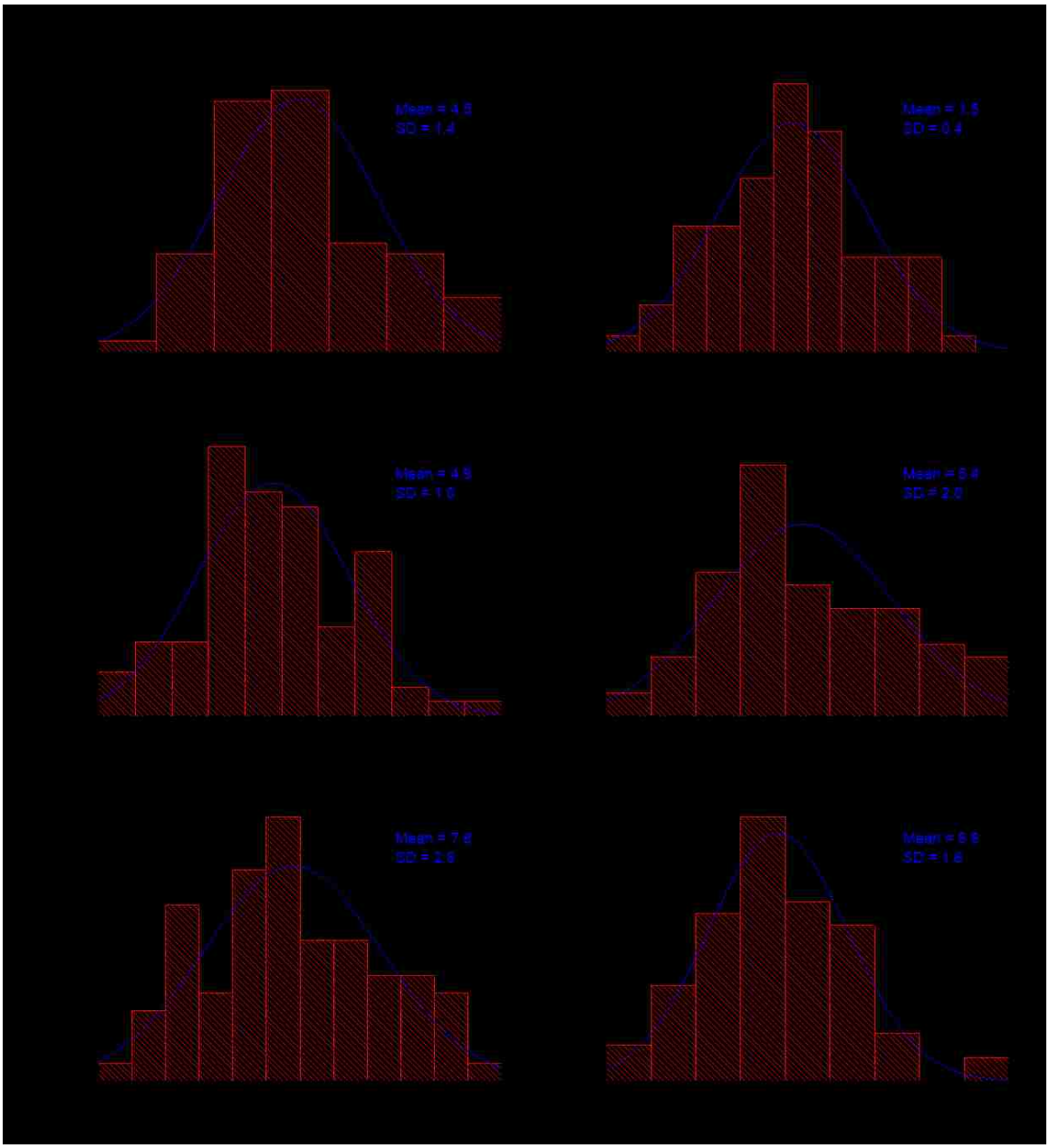

Figure S4.7 Grain size distributions for different doped LZO samples.

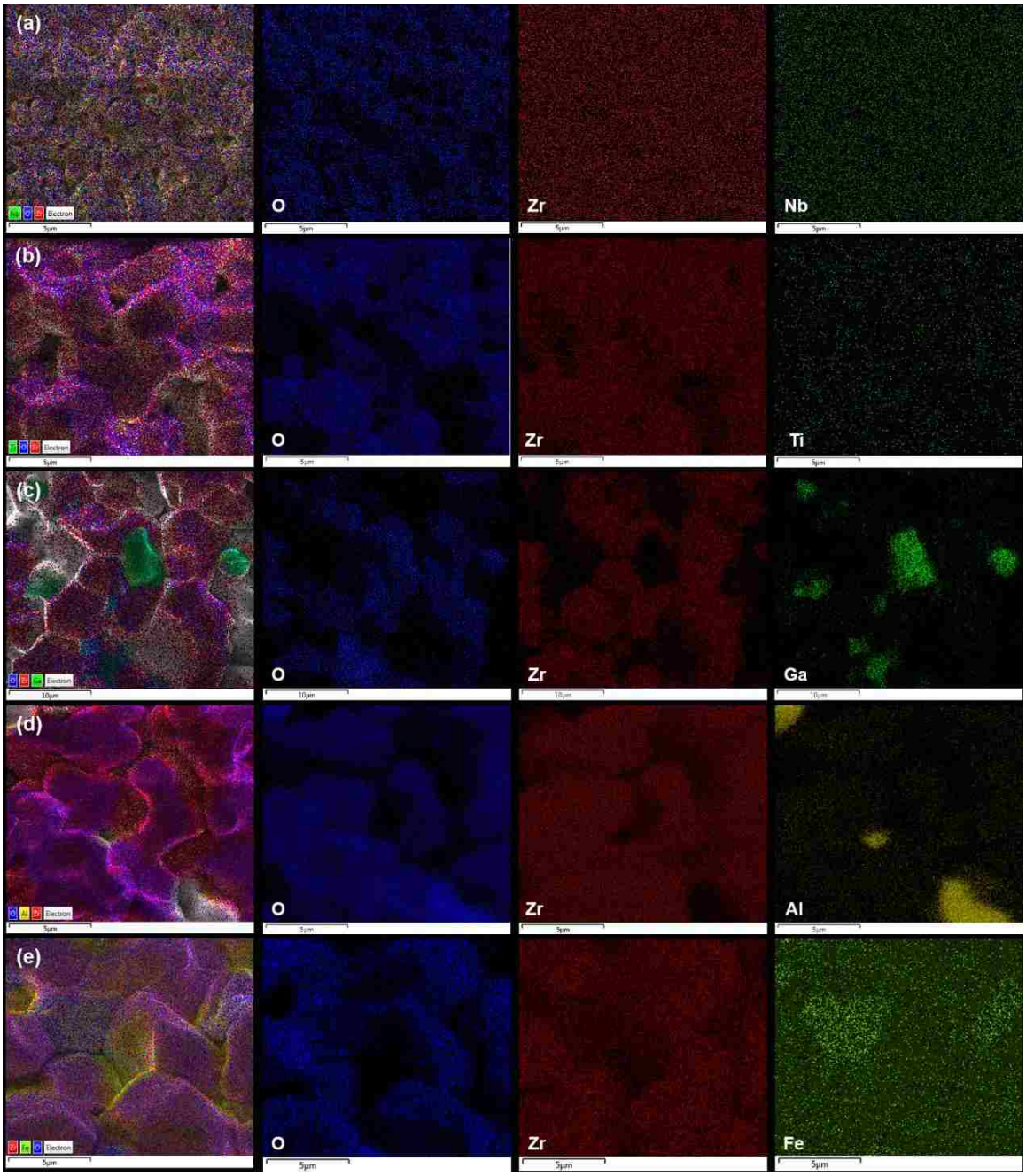

Figure S4.8 EDX composition mappings for (a) Nb-, (b)Ti-, (c) Ga-, (d) Al-, and (e) Fe-doped LZO samples.

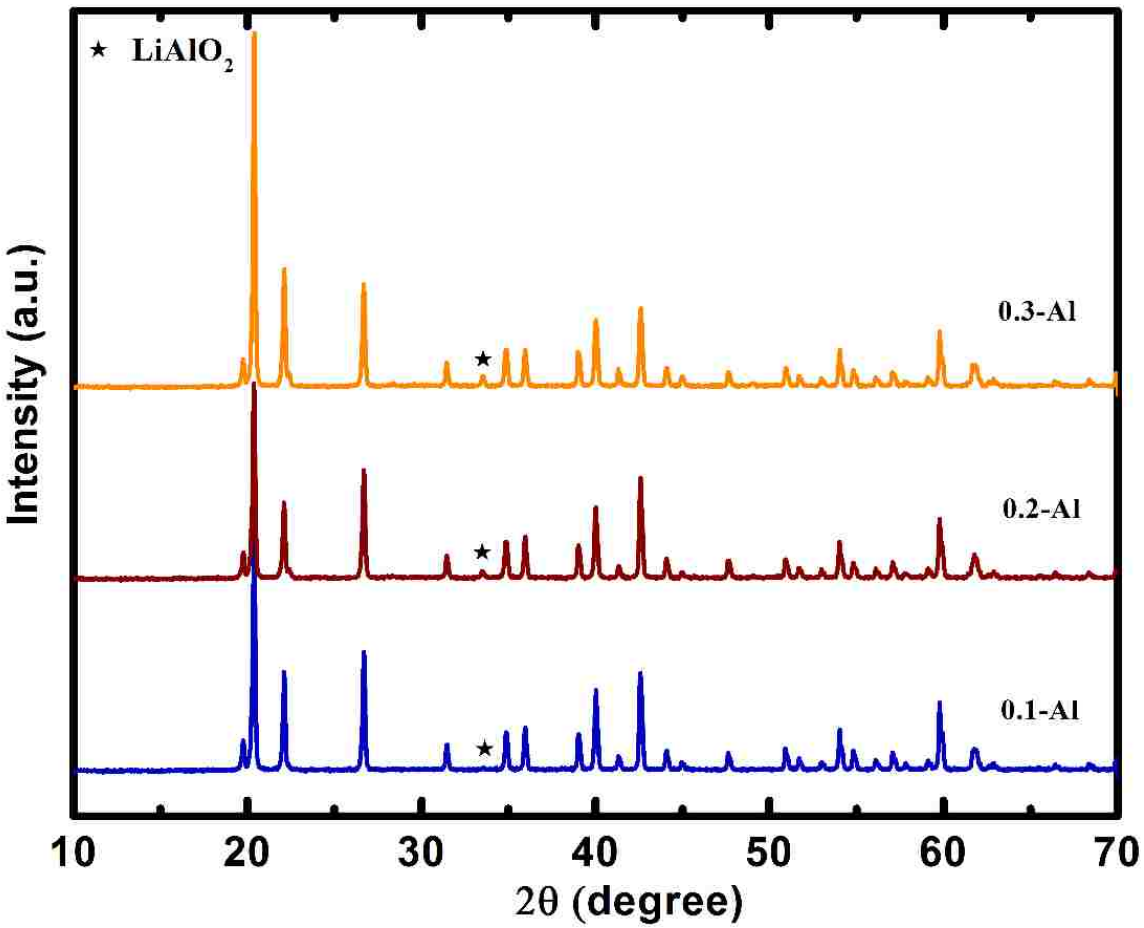

Figure S4.9 XRD patterns of powders crushed from Al-modified LZO pellets after sintering in Ar at 1000 °C/ 12 h. The Al compositions are, from top to bottom, 0.1, 0.2, and 0.3 Al per formula (0.9, 0.8, and 0.7 Zr per formula, respectively).

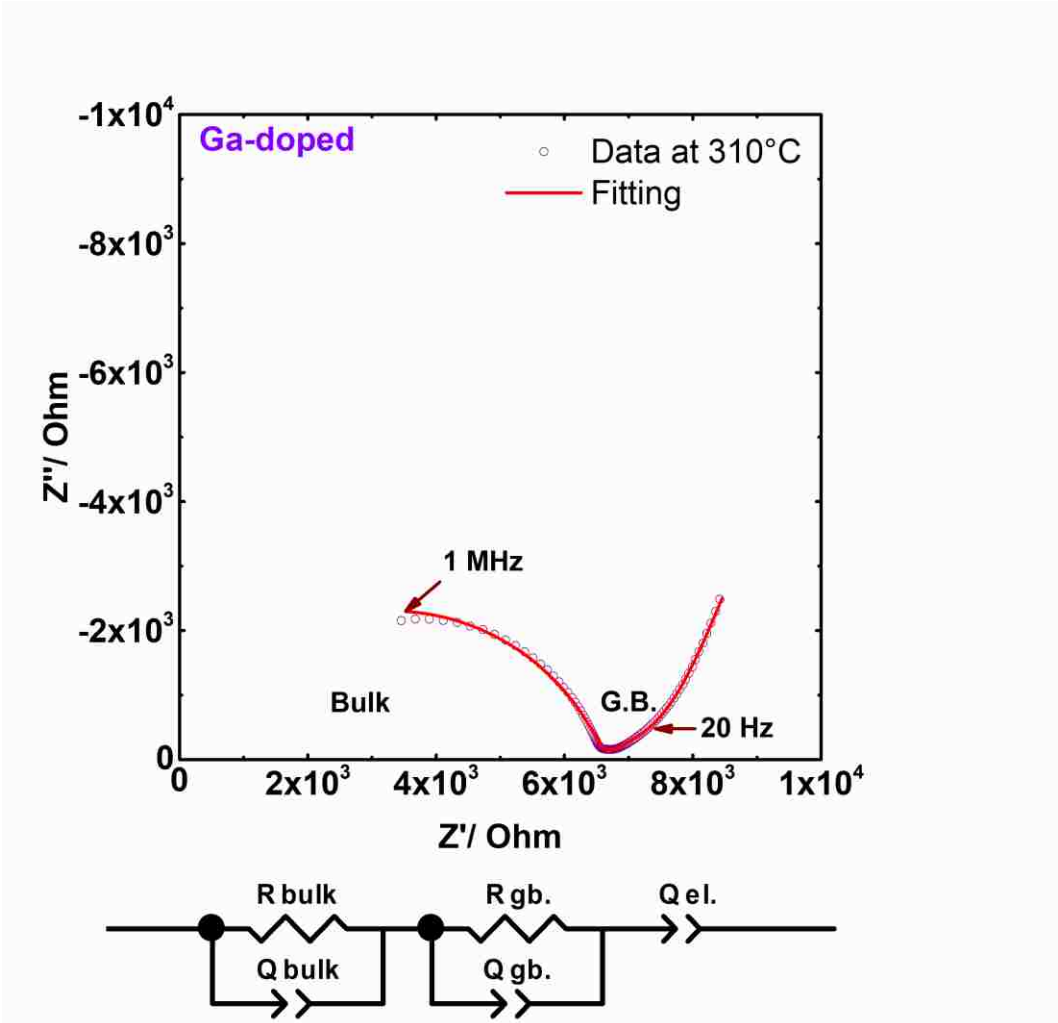

Element	Freedom	Value	Error	Error %
R1	Free(+)	40965	34.605	0.084475
QPE1-Q	Free(+)	2.2992E-12	1.839E-14	0.79984
QPE1-n	Free(+)	0.84774	0.00055028	0.064911
R2	Free(+)	6329	611.35	9.6595
QPE2-Q	Free(+)	3.0924E-10	1.7567E-10	56.807
QPE2-n	Free(+)	0.50842	0.017961	3.5327
QPE3-Q	Free(+)	5.9917E-07	1.8411E-07	30.728
QPE3-n	Free(+)	0.74882	0.016652	2.2238
Chi-Squared:		6.4163E-05		
Weighted Sum of Squares:		0.015014		

Figure S4.10 A representative fitting example of AC impedance spectra for Ga-doped LZO. Based on $C = (Q*R)^{(1/n)}/R$, the bulk capacitance is estimated to be $C_b=1.26\cdot10^{-13}$ F, and the grain boundary capacitance $C_{gb}=9.35\cdot10^{-10}$ F.

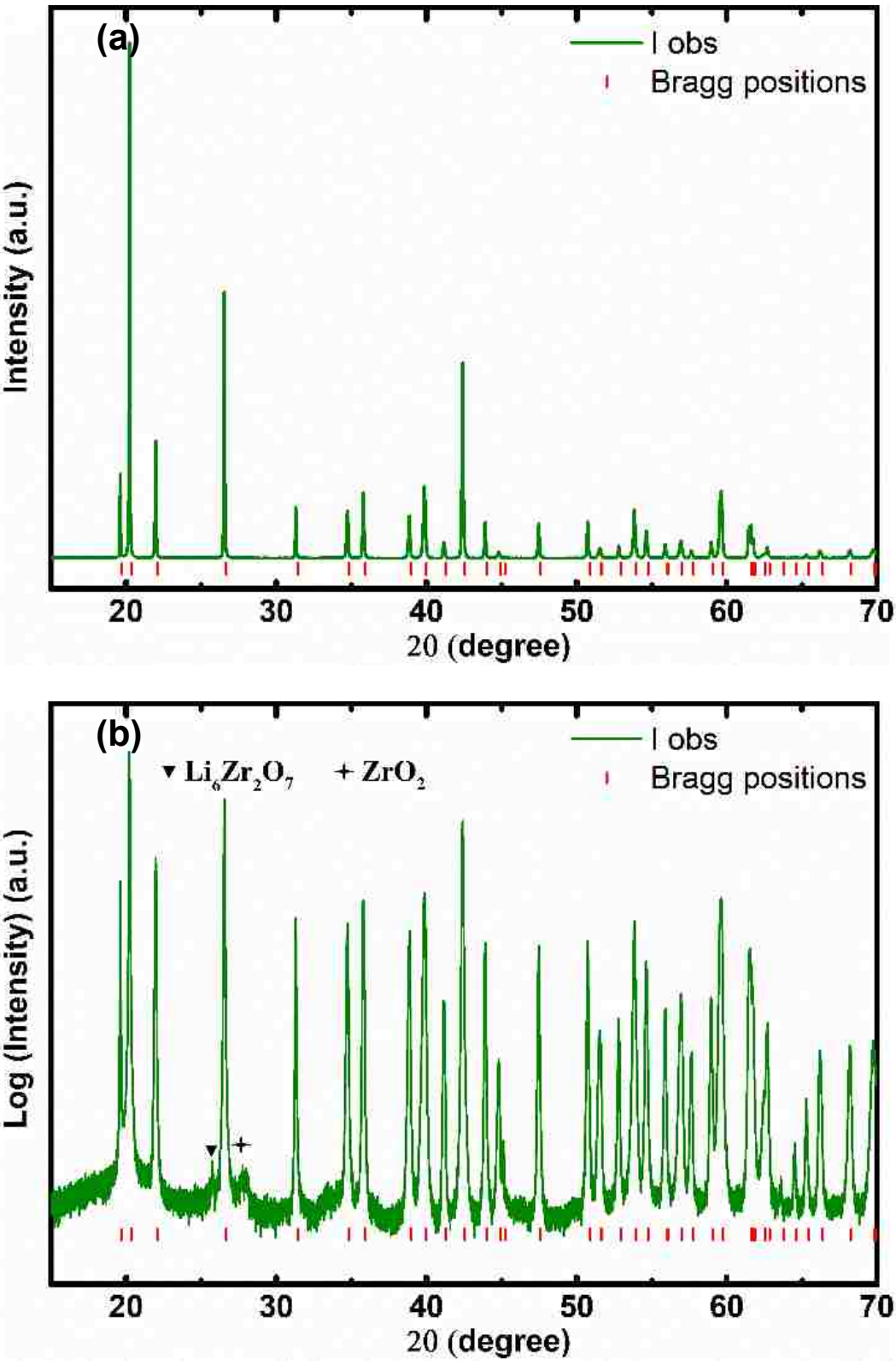

Figure S4.11 Synchrotron high-resolution XRD pattern of pulverized Fe-doped LZO pellets (a) in original intensity scale, (b) in log scale.

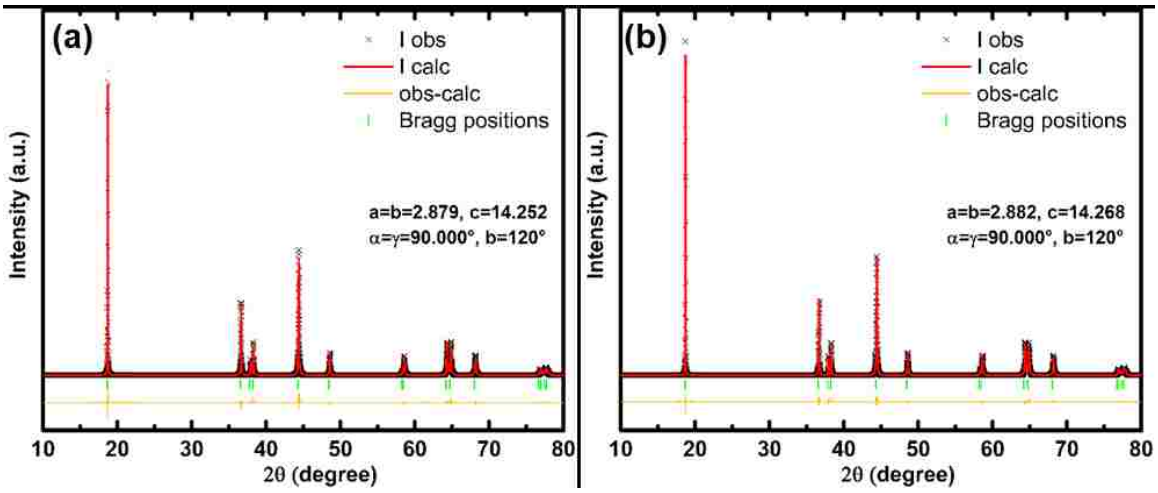

Figure S5.1 Refinement results for synchrotron XRD patterns of (a) LZO-Air and (b) LZO-O_2 sample.

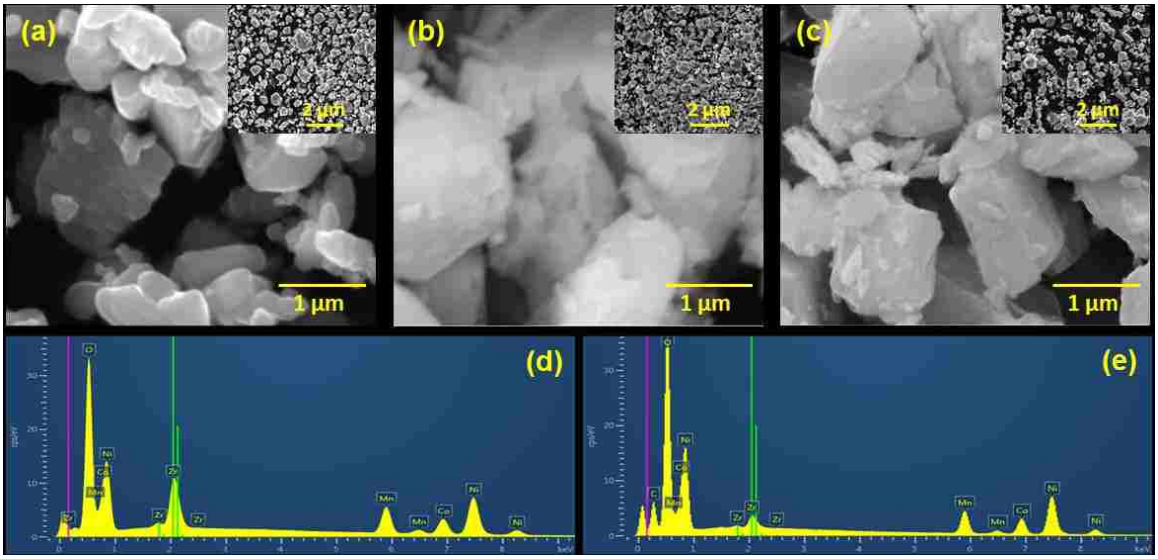

Figure S5.2 SEM images of the (a) pristine, (b) LZO-Air, and (c) LZO-O_2 sample. EDX spectrum of (d) LZO-Air, and (e) LZO-O_2 sample.

Table S5.1 Resistance values of pristine and coated samples after different cycles

	Pristine			LZO-Air			LZO-O_2		
	1st	10th	100th	1st	10th	100th	1st	10th	100th
R_{SEI} (Ω)	28	34	34	23	23	20	14	16	11
R_e (Ω)	14	40	25	12	45	27	8	45	23
R_{ct} (Ω)	184	221	1117	139	180	511	129	148	320

Table S5.2 The potentials of redox peaks in the 1st, 2nd, and 7th scans

Sample	1st Scan			2nd Scan			7th Scan		
	O	R	Δ	O	R	Δ	O	R	Δ
Pristine	3.896	3.677	**0.219**	3.819	3.681	**0.138**	3.815	3.667	**0.148**
LZO-Air	3.901	3.651	**0.250**	3.841	3.649	**0.192**	3.833	3.659	**0.174**
LZO-O_2	3.870	3.667	**0.203**	3.815	3.672	**0.143**	3.813	3.673	**0.140**

GITT (galvanostatic intermittent titration technique) was also used to determine the chemical diffusion coefficients of the $LiNi_{0.6}Co_{0.2}Mn_{0.2}O_2$ electrodes using the following equation:[154]

$$D_{Li^+} = \frac{4}{\pi}\left(\frac{m_B V_m}{M_B A}\right)^2 \left(\frac{\Delta E_s}{\tau(\frac{dE_\tau}{d\sqrt{\tau}})}\right)^2 \qquad (\tau \ll L^2/D_{Li^+}) \tag{2}$$

where m_B is the active material mass, V_m and M_B are respectively the molar volume and molecular weight of the electroactive compound, τ is the time duration in which the current is applied, ΔE_s is the difference in the steady-state voltage at a single-step GITT experiment, and L is the diffusion length of lithium ions. Figure S5.3a shows the GITT profile of the pristine electrode and the inset (top right) demonstrates an example of a single titration step where the value of ΔE_s can be extracted. ΔE_τ denotes the potential change during charging or discharging at the time of current of flux in the absence of the *IR* drop.[154] Each cell was cycled 3 times at 0.1 C in the voltage window 3.0-4.7 V and then charged to 4.7 V at 0.1 C prior to the GITT data collection in the following discharge. In a single GITT step, a constant current flux of 0.1 C was first applied for 12 min, and a 120-min relaxation followed to reach steady state. This procedure was repeated until the 3.0 V potential limit is reached. Figure S5.3b shows the cell potential (E) as a function of $\tau^{1/2}$ for a single GITT curve of the pristine electrode, where a linear relationship can be fitted which implies a diffusion process.[160] The data of the two coated samples can be seen in Figure S5.3c-d. Following procedures described above, the D_{Li^+} values for all electrodes are calculated based on the values of ΔE_s and $dE_\tau/d\sqrt{\tau}$ in Eq. (2) as a function of voltage and they are plotted in Figure 5.8.

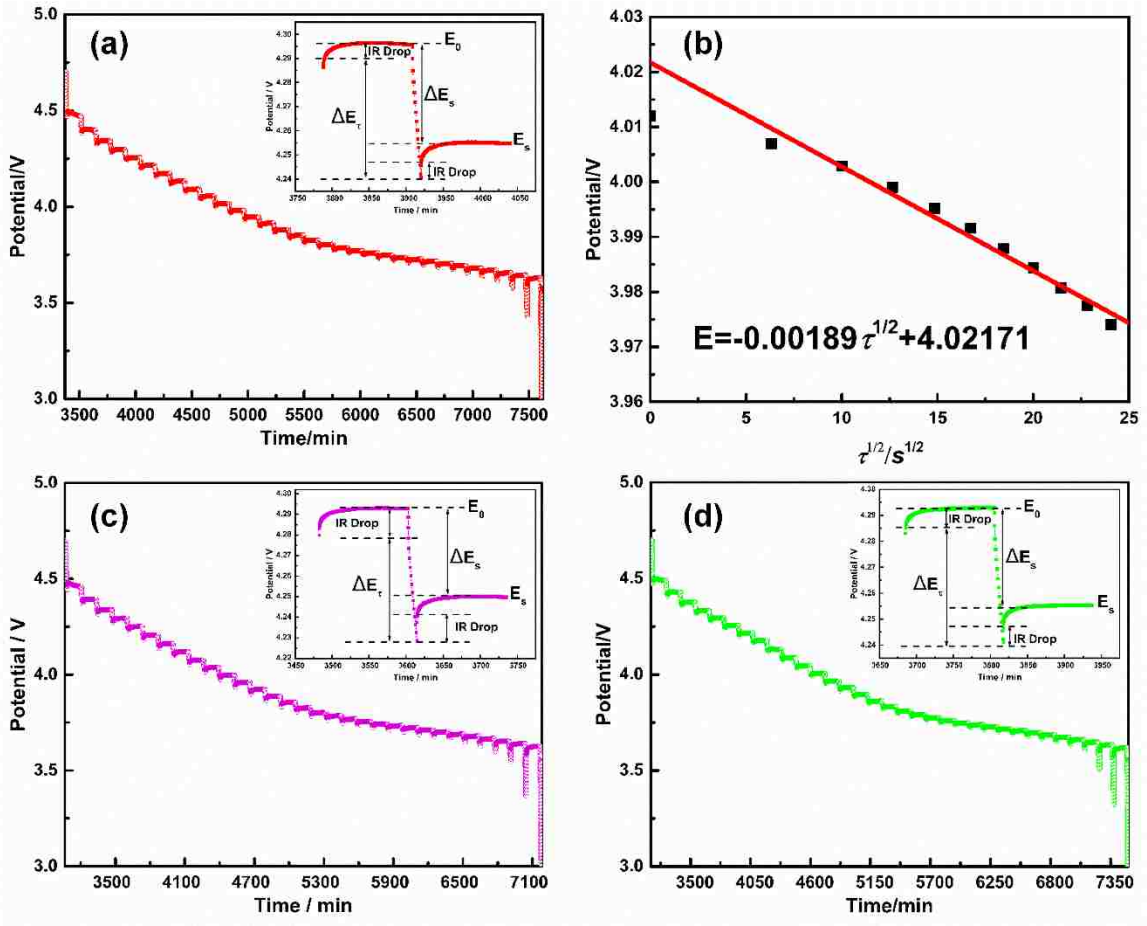

Figure S5.3 (a) GITT curve of the pristine electrode between 3.0 V and 4.7 V. The inset (top right) shows a single titration step, and (b) shows the linear fit of the cell voltage as a function of the square root of time. GITT curve and a single titration step of GITT curve (inset) of (c) LZO-Air, and (d) LZO-O_2.

The Mn 2p and Co 2p XPS spectra of the pristine and coated samples before cycling are about the same as seen in Figure S5.4a-b. The peaks at 779.98 eV and 642.28 eV correspond to Co $2p_{3/2}$ and Mn $2p_{2/3}$, respectively, matching well with those reported in the literature.[134, 137] The Co 2p and Mn 2p scans of the cycled electrodes (Figure S4c-d) are identical to those of the as-prepared samples, suggesting the well retained charge states of Co^{3+} and Mn^{4+} after many cycles.[158]

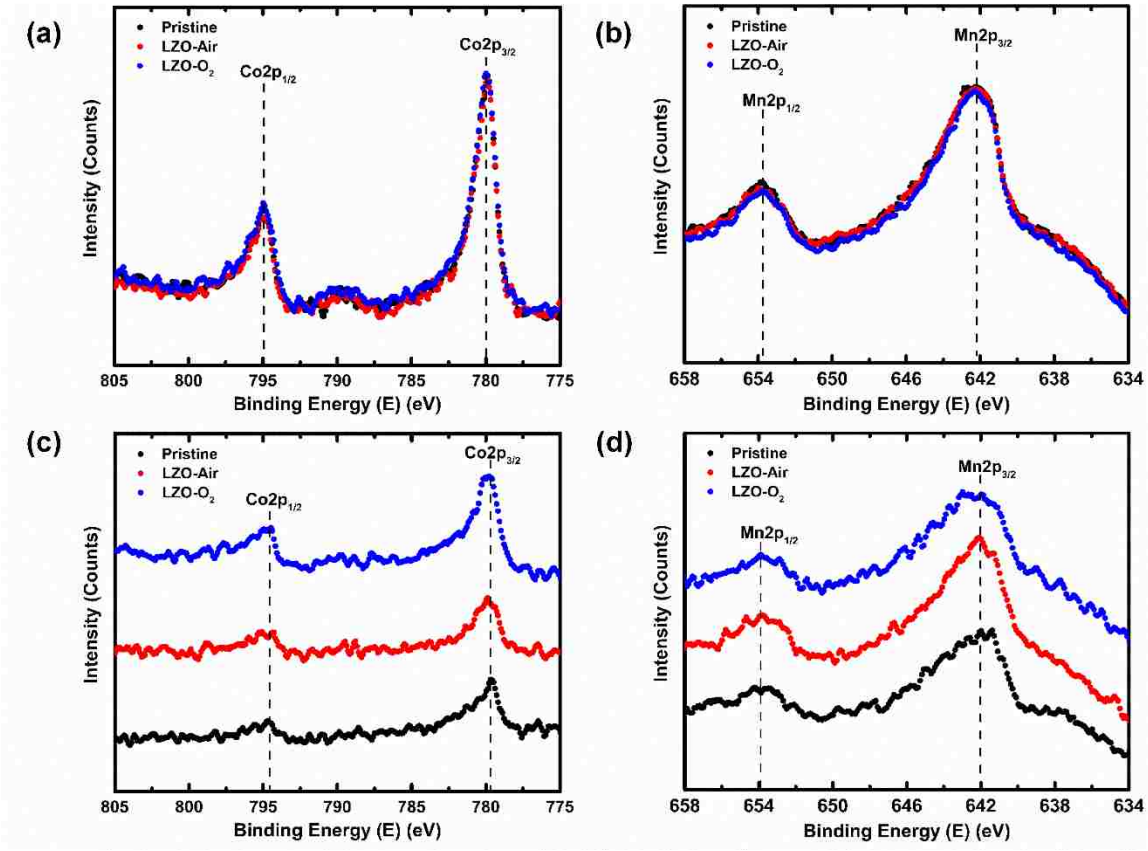

Figure S5.4 XPS Co 2p and Mn 2p scans of (a-b) the as-prepared, and (c-d) 0.2C cycled (150 cycles) electrode samples.

Bibliography

1. Bates, J. B.; Dudney, N. J.; Gruzalski, G. R.; Zuhr, R. A.; Choudhury, A.; Luck, C. F.; Robertson, J. D., Fabrication and characterization of amorphous lithium electrolyte thin films and rechargeable thin-film batteries. *Journal of Power Sources* **1993,** *43* (1–3), 103-110.

2. Zhan, X.; Shirpour, M., Evolution of solid/aqueous interface in aqueous sodium-ion batteries. *Chemical Communications* **2017,** *53* (1), 204-207.

3. Thackeray, M. M.; Wolverton, C.; Isaacs, E. D., Electrical energy storage for transportation—approaching the limits of, and going beyond, lithium-ion batteries. *Energy & Environmental Science* **2012,** *5* (7), 7854-7863.

4. Takada, K., Progress and prospective of solid-state lithium batteries. *Acta Materialia* **2013,** *61* (3), 759-770.

5. Cao, C.; Li, Z.; Wang, X.-L.; Zhao, X.; Han, W.-Q., Recent advances in inorganic solid electrolytes for lithium batteries. *Frontiers in Energy Research* **2014,** *2*, 1.

6. Bachman, J. C.; Muy, S.; Grimaud, A.; Chang, H.-H.; Pour, N.; Lux, S. F.; Paschos, O.; Maglia, F.; Lupart, S.; Lamp, P., Inorganic Solid-State Electrolytes for Lithium Batteries: Mechanisms and Properties Governing Ion Conduction. *Chemical reviews* **2015,** *116* (1), 140-162.

7. Ong, S. P.; Mo, Y.; Richards, W. D.; Miara, L.; Lee, H. S.; Ceder, G., Phase stability, electrochemical stability and ionic conductivity of the Li 10±1 MP 2 X 12 (M= Ge, Si, Sn, Al or P, and X= O, S or Se) family of superionic conductors. *Energy & Environmental Science* **2013,** *6* (1), 148-156.

8. Kamaya, N.; Homma, K.; Yamakawa, Y.; Hirayama, M.; Kanno, R.; Yonemura, M.; Kamiyama, T.; Kato, Y.; Hama, S.; Kawamoto, K.; Mitsui, A., A lithium superionic conductor. *Nat Mater* **2011,** *10* (9), 682-686.

9. Mo, Y.; Ong, S. P.; Ceder, G., First principles study of the Li10GeP2S12 lithium super ionic conductor material. *Chemistry of Materials* **2011,** *24* (1), 15-17.

10. Miara, L. J.; Ong, S. P.; Mo, Y.; Richards, W. D.; Park, Y.; Lee, J.-M.; Lee, H. S.; Ceder, G., Effect of Rb and Ta Doping on the Ionic Conductivity and Stability of the Garnet Li7+ 2 x − y (La3 − x Rb x)(Zr2 − y Ta y) O12 (0⩽ x⩽ 0.375, 0⩽ y⩽ 1) Superionic Conductor: A First Principles Investigation. *Chemistry of Materials* **2013,** *25* (15), 3048-3055.

11. Bohnke, O.; Bohnke, C.; Fourquet, J., Mechanism of ionic conduction and electrochemical intercalation of lithium into the perovskite lanthanum lithium titanate. *Solid State Ionics* **1996,** *91* (1), 21-31.

12. Mei, A.; Wang, X.-L.; Lan, J.-L.; Feng, Y.-C.; Geng, H.-X.; Lin, Y.-H.; Nan, C.-W., Role of amorphous boundary layer in enhancing ionic conductivity of lithium–lanthanum–titanate electrolyte. *Electrochimica Acta* **2010,** *55* (8), 2958-2963.

13. Chen, C. H.; Amine, K., Ionic conductivity, lithium insertion and extraction of lanthanum lithium titanate. *Solid State Ionics* **2001,** *144* (1–2), 51-57.

14. Hartmann, P.; Leichtweiss, T.; Busche, M. R.; Schneider, M.; Reich, M.; Sann, J.; Adelhelm, P.; Janek, J., Degradation of NASICON-Type Materials in Contact with Lithium Metal: Formation of Mixed Conducting Interphases (MCI) on Solid Electrolytes. *The Journal of Physical Chemistry C* **2013,** *117* (41), 21064-21074.

15. Wenzel, S.; Leichtweiss, T.; Krüger, D.; Sann, J.; Janek, J., Interphase formation on lithium solid electrolytes—An in situ approach to study interfacial reactions by photoelectron spectroscopy. *Solid State Ionics* **2015,** *278*, 98-105.

16. Kuwata, N.; Kawamura, J.; Toribami, K.; Hattori, T.; Sata, N., Thin-film lithium-ion battery with amorphous solid electrolyte fabricated by pulsed laser deposition. *Electrochemistry Communications* **2004,** *6* (4), 417-421.

17. Yu, X.; Bates, J. B.; Jellison, G. E.; Hart, F. X., A Stable Thin‐Film Lithium Electrolyte: Lithium Phosphorus Oxynitride. *Journal of The Electrochemical Society* **1997,** *144* (2), 524-532.

18. Kim, J.; Park, G.; Lee, K.; Park, H.; Nam, S.; Song, S., Li–B–O–N electrolytes for all-solid-state thin film batteries. *Journal of Power Sources* **2009,** *189* (1), 211-216.

19. Inaguma, Y.; Liquan, C.; Itoh, M.; Nakamura, T.; Uchida, T.; Ikuta, H.; Wakihara, M., High ionic conductivity in lithium lanthanum titanate. *Solid State Communications* **1993,** *86* (10), 689-693.

20. Morata-Orrantia, A.; García-Martín, S.; Morán, E.; Alario-Franco, M. Á., A New La2/3Li x Ti1-x Al x O3 Solid Solution: Structure, Microstructure, and Li+ Conductivity. *Chemistry of materials* **2002,** *14* (7), 2871-2875.

21. Aono, H.; Sugimoto, E.; Sadaoka, Y.; Imanaka, N.; Adachi, G.-y., Ionic conductivity of solid electrolytes based on lithium titanium phosphate. *Journal of the Electrochemical Society* **1990,** *137* (4), 1023-1027.

22. Aono, H.; Sugimoto, E.; Sadaoka, Y.; Imanaka, N.; Adachi, G. y., The Electrical Properties of Ceramic Electrolytes for LiM x Ti2− x (PO 4) 3+ yLi2 O, M= Ge, Sn, Hf, and Zr Systems. *Journal of The Electrochemical Society* **1993,** *140* (7), 1827-1833.

23. Allen, J. L.; Wolfenstine, J.; Rangasamy, E.; Sakamoto, J., Effect of substitution (Ta, Al, Ga) on the conductivity of Li7La3Zr2O12. *Journal of Power Sources* **2012,** *206*, 315-319.

24. Bernuy-Lopez, C.; Manalastas, W.; Lopez del Amo, J. M.; Aguadero, A.; Aguesse, F.; Kilner, J. A., Atmosphere Controlled Processing of Ga-Substituted Garnets for High Li-Ion Conductivity Ceramics. *Chemistry of Materials* **2014,** *26* (12), 3610-3617.

25. Awaka, J.; Kijima, N.; Hayakawa, H.; Akimoto, J., Synthesis and structure analysis of tetragonal Li 7 La 3 Zr 2 O 12 with the garnet-related type structure. *Journal of solid state chemistry* **2009,** *182* (8), 2046-2052.

26. Murugan, R.; Thangadurai, V.; Weppner, W., Fast Lithium Ion Conduction in Garnet‐Type Li7La3Zr2O12. *Angewandte Chemie International Edition* **2007,** *46* (41), 7778-7781.

27. Thangadurai, V.; Kaack, H.; Weppner, W. J., Novel Fast Lithium Ion Conduction in Garnet‐Type Li5La3M2O12 (M= Nb, Ta). *Journal of the American Ceramic Society* **2003,** *86* (3), 437-440.

28. Wu, J.-F.; Chen, E.-Y.; Yu, Y.; Liu, L.; Wu, Y.; Pang, W. K.; Peterson, V. K.; Guo, X., Gallium-doped Li7La3Zr2O12 garnet-type electrolytes with high lithium-ion conductivity. *ACS applied materials & interfaces* **2017,** *9* (2), 1542-1552.

29. Wolfenstine, J.; Ratchford, J.; Rangasamy, E.; Sakamoto, J.; Allen, J. L., Synthesis and high Li-ion conductivity of Ga-stabilized cubic Li 7 La 3 Zr 2 O 12. *Materials Chemistry and Physics* **2012,** *134* (2), 571-575.

30. Zhou, P.; Wang, J.; Cheng, F.; Li, F.; Chen, J., A solid lithium superionic conductor Li11AlP2S12 with a thio-LISICON analogous structure. *Chemical Communications* **2016,** *52* (36), 6091-6094.

31. Lu, Z. In *A Novel Solid Electrolyte Material (Li 17 Ge 2 P 3 S 20) with High Ionic Conductivity*, PRiME 2016/230th ECS Meeting (October 2-7, 2016), Ecs: 2016.

32. Alpen, U. v.; Rabenau, A.; Talat, G., Ionic conductivity in Li3N single crystals. *Applied Physics Letters* **1977,** *30* (12), 621-623.

33. Boukamp, B.; Huggins, R., Ionic conductivity in lithium imide. *Physics Letters A* **1979,** *72* (6), 464-466.

34. Farrington, G.; Dunn, B.; Briant, J., Li+ and divalent ion conductivity in beta and beta ″ alumina. *Solid State Ionics* **1981,** *3*, 405-408.

35. Briant, J.; Farrington, G., Ionic Conductivity in Lithium and Lithium‐Sodium Beta Alumina. *Journal of The Electrochemical Society* **1981,** *128* (9), 1830-1834.

36. Seino, Y.; Ota, T.; Takada, K.; Hayashi, A.; Tatsumisago, M., A sulphide lithium super ion conductor is superior to liquid ion conductors for use in rechargeable batteries. *Energy & Environmental Science* **2014,** *7* (2), 627-631.

37. Ohta, S.; Kobayashi, T.; Seki, J.; Asaoka, T., Electrochemical performance of an all-solid-state lithium ion battery with garnet-type oxide electrolyte. *Journal of Power Sources* **2012,** *202*, 332-335.

38. Kotobuki, M.; Kanamura, K.; Sato, Y.; Yoshida, T., Fabrication of all-solid-state lithium battery with lithium metal anode using Al 2 O 3-added Li 7 La 3 Zr 2 O 12 solid electrolyte. *Journal of Power Sources* **2011,** *196* (18), 7750-7754.

39. Wolfenstine, J.; Allen, J.; Read, J.; Sakamoto, J., Chemical stability of cubic Li7La3Zr2O12 with molten lithium at elevated temperature. *Journal of Materials Science* **2013,** *48* (17), 5846-5851.

40. Xu, M.; Park, M. S.; Lee, J. M.; Kim, T. Y.; Park, Y. S.; Ma, E., Mechanisms of Li+ transport in garnet-type cubic Li 3+ x La 3 M 2 O 12 (M= Te, Nb, Zr). *Physical Review B* **2012,** *85* (5), 052301.

41. Li, Y.; Han, J.-T.; Wang, C.-A.; Vogel, S. C.; Xie, H.; Xu, M.; Goodenough, J. B., Ionic distribution and conductivity in lithium garnet Li 7 La 3 Zr 2 O 12. *Journal of Power Sources* **2012,** *209*, 278-281.

42. Xie, H.; Li, Y.; Goodenough, J. B., Low-temperature synthesis of Li 7 La 3 Zr 2 O 12 with cubic garnet-type structure. *Materials Research Bulletin* **2012,** *47* (5), 1229-1232.

43. Geiger, C. A.; Alekseev, E.; Lazic, B.; Fisch, M.; Armbruster, T.; Langner, R.; Fechtelkord, M.; Kim, N.; Pettke, T.; Weppner, W., Crystal chemistry and stability of "Li7La3Zr2O12" garnet: a fast lithium-ion conductor. *Inorganic chemistry* **2010,** *50* (3), 1089-1097.

44. Rangasamy, E.; Wolfenstine, J.; Sakamoto, J., The role of Al and Li concentration on the formation of cubic garnet solid electrolyte of nominal composition Li 7 La 3 Zr 2 O 12. *Solid State Ionics* **2012,** *206*, 28-32.

45. Zhang, L.; Zhan, X.; Cheng, Y.-T.; Shirpour, M., Charge Transport in Electronic–Ionic Composites. *The Journal of Physical Chemistry Letters* **2017,** *8* (21), 5385-5389.

46. Buannic, L.; Orayech, B.; López Del Amo, J.-M.; Carrasco, J.; Katcho, N. A.; Aguesse, F.; Manalastas, W.; Zhang, W.; Kilner, J.; Llordés, A., Dual Substitution Strategy to Enhance Li+ Ionic Conductivity in Li7La3Zr2O12 Solid Electrolyte. *Chemistry of Materials* **2017,** *29* (4), 1769-1778.

47. Awaka, J.; Takashima, A.; Kataoka, K.; Kijima, N.; Idemoto, Y.; Akimoto, J., Crystal structure of fast lithium-ion-conducting cubic Li7La3Zr2O12. *Chemistry Letters* **2011,** *40* (1), 60-62.

48. Luntz, A. C.; Voss, J.; Reuter, K., Interfacial Challenges in Solid-State Li Ion Batteries. *The journal of physical chemistry letters* **2015,** *6* (22), 4599-4604.

49. Buschmann, H.; Dölle, J.; Berendts, S.; Kuhn, A.; Bottke, P.; Wilkening, M.; Heitjans, P.; Senyshyn, A.; Ehrenberg, H.; Lotnyk, A., Structure and dynamics of the fast lithium ion conductor "Li 7 La 3 Zr 2 O 12". *Physical Chemistry Chemical Physics* **2011,** *13* (43), 19378-19392.

50. Buschmann, H.; Berendts, S.; Mogwitz, B.; Janek, J., Lithium metal electrode kinetics and ionic conductivity of the solid lithium ion conductors "Li 7 La 3 Zr 2 O 12" and Li 7− x La 3 Zr 2− x Ta x O 12 with garnet-type structure. *Journal of Power Sources* **2012,** *206*, 236-244.

51. Kotobuki, M.; Munakata, H.; Kanamura, K.; Sato, Y.; Yoshida, T., Compatibility of Li7La3Zr2O12 solid electrolyte to all-solid-state battery using Li metal anode. *Journal of the Electrochemical Society* **2010,** *157* (10), A1076-A1079.

52. Shimonishi, Y.; Toda, A.; Zhang, T.; Hirano, A.; Imanishi, N.; Yamamoto, O.; Takeda, Y., Synthesis of garnet-type Li 7− x La 3 Zr 2 O 12− 1/2x and its stability in aqueous solutions. *Solid State Ionics* **2011,** *183* (1), 48-53.

53. Yamamoto, K.; Iriyama, Y.; Asaka, T.; Hirayama, T.; Fujita, H.; Fisher, C. A.; Nonaka, K.; Sugita, Y.; Ogumi, Z., Dynamic Visualization of the Electric Potential in an All‐Solid‐State Rechargeable Lithium Battery. *Angewandte Chemie International Edition* **2010,** *49* (26), 4414-4417.

54. Aizawa, Y.; Yamamoto, K.; Sato, T.; Murata, H.; Yoshida, R.; Fisher, C. A. J.; Kato, T.; Iriyama, Y.; Hirayama, T., In situ electron holography of electric potentials inside a solid-state electrolyte: Effect of electric-field leakage. *Ultramicroscopy* **2017,** *178*, 20-26.

55. Park, K.; Yu, B.-C.; Jung, J.-W.; Li, Y.; Zhou, W.; Gao, H.; Son, S.; Goodenough, J. B., Electrochemical Nature of the Cathode Interface for a Solid-State Lithium-Ion Battery: Interface between LiCoO2 and Garnet-Li7La3Zr2O12. *Chemistry of Materials* **2016,** *28* (21), 8051-8059.

56. Kc, S.; Longo, R. C.; Xiong, K.; Cho, K., Point defects in garnet-type solid electrolyte (c-Li7La3Zr2O12) for Li-ion batteries. *Solid State Ionics* **2014,** *261* (0), 100-105.

57. Bernstein, N.; Johannes, M.; Hoang, K., Origin of the structural phase transition in Li 7 La 3 Zr 2 O 12. *Physical review letters* **2012,** *109* (20), 205702.

58. Meier, K.; Laino, T.; Curioni, A., Solid-state electrolytes: revealing the mechanisms of Li-ion conduction in tetragonal and cubic LLZO by first-principles calculations. *The Journal of Physical Chemistry C* **2014,** *118* (13), 6668-6679.

59. Cheng, L.; Park, J. S.; Hou, H.; Zorba, V.; Chen, G.; Richardson, T.; Cabana, J.; Russo, R.; Doeff, M., Effect of microstructure and surface impurity segregation on the electrical and electrochemical properties of dense Al-substituted Li 7 La 3 Zr 2 O 12. *Journal of Materials Chemistry A* **2014,** *2* (1), 172-181.

60. Kubicek, M.; Wachter-Welzl, A.; Rettenwander, D.; Wagner, R.; Berendts, S.; Uecker, R.; Amthauer, G.; Hutter, H.; Fleig, J., Oxygen Vacancies in Fast Lithium-Ion Conducting Garnets. *Chemistry of Materials* **2017**.

61. Maier, J.; Amin, R., Defect chemistry of LiFePO4. *Journal of The Electrochemical Society* **2008,** *155* (4), A339-A344.

62. Gerbig, O.; Merkle, R.; Maier, J., Electron and ion transport in Li2O2. *Advanced Materials* **2013,** *25* (22), 3129-3133.

63. Dobretsov, E. A.; Mateyshina, Y. G.; Uvarov, N. F., Influence of lithium oxide excess and alumina on grain boundary resistance of Li 6.75 La 3 Zr 1.75 Nb 0.25 O 12 solid electrolyte. *Solid State Ionics* **2017,** *299*, 55-59.

64. Cheng, L.; Crumlin, E. J.; Chen, W.; Qiao, R.; Hou, H.; Lux, S. F.; Zorba, V.; Russo, R.; Kostecki, R.; Liu, Z., The origin of high electrolyte–electrode interfacial resistances in lithium cells containing garnet type solid electrolytes. *Physical Chemistry Chemical Physics* **2014,** *16* (34), 18294-18300.

65. Larson, A. C.; Von Dreele, R. B., Gsas. *General Structure Analysis System. LANSCE, MS-H805, Los Alamos, New Mexico* **1994**.

66. Toby, B. H., EXPGUI, a graphical user interface for GSAS. *Journal of applied crystallography* **2001,** *34* (2), 210-213.

67. Huang, M.; Liu, T.; Deng, Y.; Geng, H.; Shen, Y.; Lin, Y.; Nan, C.-W., Effect of sintering temperature on structure and ionic conductivity of Li 7− x La 3 Zr 2 O 12− 0.5 x (x= 0.5~ 0.7) ceramics. *Solid State Ionics* **2011,** *204*, 41-45.

68. Duvel, A.; Kuhn, A.; Robben, L.; Wilkening, M.; Heitjans, P., Mechanosynthesis of Solid Electrolytes: Preparation, Characterization, and Li Ion Transport Properties of Garnet-Type Al-Doped Li7La3Zr2O12 Crystallizing with Cubic Symmetry. *J Phys Chem C* **2012,** *116* (29), 15192-15202.

69. Rettenwander, D.; Blaha, P.; Laskowski, R.; Schwarz, K.; Bottke, P.; Wilkening, M.; Geiger, C. A.; Amthauer, G., DFT Study of the Role of Al3+ in the Fast Ion-Conductor Li7-3xAlx3+La3Zr2O12 Garnet. *Chem Mater* **2014,** *26* (8), 2617-2623.

70. Chen, C.; Lu, Z. H.; Ciucci, F., Data mining of molecular dynamics data reveals Li diffusion characteristics in garnet Li7La3Zr2O12. *Sci Rep-Uk* **2017,** *7*.

71. Rettenwander, D.; Langer, J.; Schmidt, W.; Arrer, C.; Harris, K. J.; Terskikh, V.; Goward, G. R.; Wilkening, M.; Amthauer, G., Site Occupation of Ga and Al in Stabilized Cubic Li7-3(x plus y)GaxAlyLa3Zr2O12 Garnets As Deduced from (27)AI and Ga-71 MAS NMR at Ultrahigh Magnetic Fields. *Chem Mater* **2015,** *27* (8), 3135-3142.

72. Geiger, C. A.; Alekseev, E.; Lazic, B.; Fisch, M.; Armbruster, T.; Langner, R.; Fechtelkord, M.; Kim, N.; Pettke, T.; Weppner, W., Crystal Chemistry and Stability of "Li7La3Zr2O12" Garnet: A Fast Lithium-Ion Conductor. *Inorg Chem* **2011,** *50* (3), 1089-1097.

73. Wolfenstine, J.; Sakamoto, J.; Allen, J., Electron microscopy characterization of hot-pressed Al substituted Li7La3Zr2O12. *Journal of Materials Science* **2012,** *47* (10), 4428-4431.

74. Fleig, J.; Maier, J., Finite‐Element Calculations on the Impedance of Electroceramics with Highly Resistive Grain Boundaries: I, Laterally Inhomogeneous Grain Boundaries. *Journal of the American Ceramic Society* **1999,** *82* (12), 3485-3493.

75. Ibbotson, M. G. E., *Electrical Grain Boundary Characteristics of Dense Cubic Li 7-3x Al x La 3 Zr 2 O 7 (x= 0.05-0.3) Prepared by Spark Plasma Sintering*. University of California, Davis: 2014.

76. Kumazaki, S.; Iriyama, Y.; Kim, K.-H.; Murugan, R.; Tanabe, K.; Yamamoto, K.; Hirayama, T.; Ogumi, Z., High lithium ion conductive Li 7 La 3 Zr 2 O 12 by inclusion of both Al and Si. *Electrochemistry communications* **2011,** *13* (5), 509-512.

77. Li, Y.; Han, J.-T.; Wang, C.-A.; Xie, H.; Goodenough, J. B., Optimizing Li+ conductivity in a garnet framework. *Journal of Materials Chemistry* **2012,** *22* (30), 15357-15361.

78. Sherstobitova, E.; Gubkin, A.; Bobrikov, I.; Kalashnova, A.; Pantyukhina, M., Bottle-necked ionic transport in Li 2 ZrO 3: high temperature neutron diffraction and impedance spectroscopy. *Electrochimica Acta* **2016,** *209*, 574-581.

79. Hellstrom, E. E.; Van Gool, W., Li ion conduction in Li2ZrO3, Li4ZrO4, and LiScO2. *Solid State Ionics* **1981,** *2* (1), 59-64.

80. Amin, R.; Maier, J., Effect of annealing on transport properties of LiFePO4: Towards a defect chemical model. *Solid State Ionics* **2008,** *178* (35-36), 1831-1836.

81. Tuller, H. L.; Bishop, S. R., Point Defects in Oxides: Tailoring Materials Through Defect Engineering. *Ann. Rev. Mater. Res.* **2011,** *41*, 369-398.

82. Rotman, S.; Tandon, R.; Tuller, H., Defect‐property correlations in garnet crystals: The electrical conductivity and defect structure of luminescent cerium‐doped yttrium aluminum garnet. *Journal of applied physics* **1985,** *57* (6), 1951-1955.

83. Rotman, S.; Tuller, H. L.; Roth, M.; Linz, A., Defect property correlations in garnet crystals. II. Electrical conductivity and optical absorption in Ca3Al2Ge3O12. *Journal of applied physics* **1985,** *57* (12), 5320-5324.

84. Amin, R.; Chiang, Y.-M., Characterization of Electronic and Ionic Transport in Li1-xNi0. 33Mn0. 33Co0. 33O2 (NMC333) and Li1-xNi0. 50Mn0. 20Co0. 30O2 (NMC523) as a Function of Li Content. *Journal of The Electrochemical Society* **2016,** *163* (8), A1512-A1517.

85. Amin, R.; Maier, J., Effect of annealing on transport properties of LiFePO 4: towards a defect chemical model. *Solid State Ionics* **2008,** *178* (35), 1831-1836.

86. Bishop, S. R.; Stefanik, T. S.; Tuller, H. L., Electrical conductivity and defect equilibria of Pr 0.1 Ce 0.9 O 2− δ. *Physical Chemistry Chemical Physics* **2011,** *13* (21), 10165-10173.

87. Bishop, S.; Duncan, K.; Wachsman, E., Surface and bulk oxygen non-stoichiometry and bulk chemical expansion in gadolinium-doped cerium oxide. *Acta Materialia* **2009,** *57* (12), 3596-3605.

88. Ong, S. P.; Mo, Y.; Ceder, G., Low hole polaron migration barrier in lithium peroxide. *Physical Review B* **2012,** *85* (8), 081105.

89. Crosbie, G., Chemical diffusivity and electrical conductivity in TiO2 containing a submicron dispersion of SiO2. *Journal of Solid State Chemistry* **1978,** *25* (4), 367-378.

90. Liang, C., Conduction Characteristics of the Lithium Iodide ‐ Aluminum Oxide Solid Electrolytes. *Journal of The Electrochemical Society* **1973,** *120* (10), 1289-1292.

91. Schuh, L.; Metselaar, R.; de With, G., Electrical transport and defect properties of Ca ‐ and Mg ‐ doped yttrium aluminum garnet ceramics. *Journal of applied physics* **1989,** *66* (6), 2627-2632.

92. Fleig, J.; Maier, J., A finite element study on the grain boundary impedance of different microstructures. *Journal of the Electrochemical Society* **1998,** *145* (6), 2081-2089.

93. Kofstad, P., *Nonstoichiometry, diffusion, and electrical conductivity in binary metal oxides*. Wiley-Interscience New York: 1972.

94. Song, S.; Kotobuki, M.; Zheng, F.; Xu, C.; Hu, N.; Lu, L.; Wang, Y.; Li, W.-D., Y-Doped Na2ZrO3: A Na-Rich Layered Oxide as a High-Capacity Cathode Material for Sodium-Ion Batteries. *ACS Sustainable Chemistry & Engineering* **2017**.

95. Ochoa-Fernández, E.; Rønning, M.; Grande, T.; Chen, D., Nanocrystalline lithium zirconate with improved kinetics for high-temperature CO2 capture. *Chemistry of materials* **2006,** *18* (6), 1383-1385.

96. Johnson, C.; Clemmer, R.; Hollenberg, G., Solid breeder materials. *Journal of Nuclear Materials* **1981,** *103*, 547-553.

97. Li, M.-Q.; Qu, M.-Z.; He, X.-Y.; Yu, Z.-L., Electrochemical properties of Li 2 ZrO 3-coated silicon/graphite/carbon composite as anode material for lithium ion batteries. *Journal of Power Sources* **2009,** *188* (2), 546-551.

98. Song, B.; Li, W.; Oh, S.-M.; Manthiram, A., Long-Life Nickel-Rich Layered Oxide Cathodes with a Uniform Li2ZrO3 Surface Coating for Lithium-Ion Batteries. *ACS Applied Materials & Interfaces* **2017,** *9* (11), 9718-9725.

99. Thackeray, M.; Johnson, C.; Kim, J.-S.; Lauzze, K.; Vaughey, J.; Dietz, N.; Abraham, D.; Hackney, S.; Zeltner, W.; Anderson, M., ZrO 2-and Li 2 ZrO 3-stabilized spinel and layered electrodes for lithium batteries. *Electrochemistry communications* **2003,** *5* (9), 752-758.

100. Lu, P.; Ding, F.; Xu, Z.; Liu, J.; Liu, X.; Xu, Q., Study on (100-x)(70Li 2 S-30P 2 S 5)-xLi 2 ZrO 3 glass-ceramic electrolyte for all-solid-state lithium-ion batteries. *Journal of Power Sources* **2017,** *356*, 163-171.

101. Ferreira, A. R.; Reuter, K.; Scheurer, C., DFT simulations of 7 Li solid state NMR spectral parameters and Li+ ion migration barriers in Li 2 ZrO 3. *RSC Advances* **2016,** *6* (47), 41015-41024.

102. Wang, C.; Dou, B.; Song, Y.; Chen, H.; Xu, Y.; Xie, B., High temperature CO2 sorption on Li2ZrO3 based sorbents. *Industrial & Engineering Chemistry Research* **2014,** *53* (32), 12744-12752.

103. Hellstrom, E.; Van Gool, W., Li ion conduction in Li2ZrO3, Li4ZrO4, and LiScO2. *Solid State Ionics* **1981,** *2* (1), 59-64.

104. Bottke, P.; Freude, D.; Wilkening, M., Ultraslow Li exchange processes in diamagnetic Li2ZrO3 as monitored by EXSY NMR. *The Journal of Physical Chemistry C* **2013,** *117* (16), 8114-8119.

105. Lulewicz, J.; Roux, N.; Piazza, G.; Reimann, J.; van der Laan, J., Behaviour of Li 2 ZrO 3 and Li 2 TiO 3 pebbles relevant to their utilization as ceramic breeder for the HCPB blanket. *Journal of nuclear materials* **2000,** *283*, 1361-1365.

106. Yamawaki, M.; Yamaguchi, K.; Suzuki, A., Impact of interfaces on nuclear materials. *Ionics* **2001,** *7* (4), 339-345.

107. Zhan, X.; Cheng, Y. T.; Shirpour, M., Nonstoichiometry and Li‐Ion Transport in Lithium Zirconate: the Role of Oxygen Vacancies. *Journal of the American Ceramic Society* **2018**.

108. Kordatos, A.; Christopoulos, S.-R.; Kelaidis, N.; Chroneos, A., Defect processes in Li2ZrO3: insights from atomistic modelling. *Journal of Materials Science: Materials in Electronics* **2017**, 1-5.

109. Kubicek, M.; Wachter-Welzl, A.; Rettenwander, D.; Wagner, R.; Berendts, S.; Uecker, R.; Amthauer, G.; Hutter, H.; Fleig, J. r., Oxygen Vacancies in Fast Lithium-Ion Conducting Garnets. *Chemistry of Materials* **2017,** *29* (17), 7189-7196.

110. Xiong, R.; Ida, J.; Lin, Y., Kinetics of carbon dioxide sorption on potassium-doped lithium zirconate. *Chemical Engineering Science* **2003,** *58* (19), 4377-4385.

111. Dunstan, M. T.; Laeverenz Schlogelhofer, H.; Griffin, J. M.; Dyer, M. S.; Gaultois, M. W.; Lau, C. Y.; Scott, S. A.; Grey, C. P., Ion Dynamics and CO2 Absorption Properties of Nb, Ta and

Y-Doped Li2ZrO3 Studied by Solid-State NMR, Thermogravimetry and First-Principles Calculations. *The Journal of Physical Chemistry C* **2017**.

112. Hodeau, J. L.; Marezio, M.; Santoro, A.; Roth, R. S., Neutron profile refinement of the structures of Li2SnO3 and Li2ZrO3. *Journal of Solid State Chemistry* **1982,** *45* (2), 170-179.

113. Hodeau, J.; Marezio, M.; Santoro, A.; Roth, R., Neutron profile refinement of the structures of Li2SnO3 and Li2ZrO3. *Journal of Solid State Chemistry* **1982,** *45* (2), 170-179.

114. Baklanova, Y. V.; Arapova, I. Y.; Buzlukov, A.; Gerashenko, A.; Verkhovskii, S.; Mikhalev, K.; Denisova, T.; Shein, I.; Maksimova, L., Localization of vacancies and mobility of lithium ions in Li 2 ZrO 3 as obtained by 6, 7 Li NMR. *Journal of Solid State Chemistry* **2013,** *208*, 43-49.

115. Djenadic, R.; Botros, M.; Benel, C.; Clemens, O.; Indris, S.; Choudhary, A.; Bergfeldt, T.; Hahn, H., Nebulized spray pyrolysis of Al-doped Li 7 La 3 Zr 2 O 12 solid electrolyte for battery applications. *Solid State Ionics* **2014,** *263*, 49-56.

116. Zhan, X.; Lai, S.; Gobet, M. P.; Greenbaum, S. G.; Shirpour, M., Defect chemistry and electrical properties of garnet-type Li7La3Zr2O12. *Physical Chemistry Chemical Physics* **2018,** *20* (3), 1447-1459.

117. Tarascon, J. M.; Armand, M., Issues and challenges facing rechargeable lithium batteries. *Nature* **2001,** *414* (6861), 359-367.

118. Zhan, X.; Shirpour, M.; Yang, F., A Thermodynamic Perspective for Formation of Solid Electrolyte Interphase in Lithium-Ion Batteries. *Electrochimica Acta* **2015,** *173*, 736-742.

119. Venkatraman, S.; Choi, J.; Manthiram, A., Factors influencing the chemical lithium extraction rate from layered LiNi1− y− zCoyMnzO2 cathodes. *Electrochemistry communications* **2004,** *6* (8), 832-837.

120. Sun, Y.-K.; Kim, D.-H.; Jung, H.-G.; Myung, S.-T.; Amine, K., High-voltage performance of concentration-gradient Li [Ni0. 67Co0. 15Mn0. 18] O2 cathode material for lithium-ion batteries. *Electrochimica Acta* **2010,** *55* (28), 8621-8627.

121. Belharouak, I.; Sun, Y.-K.; Liu, J.; Amine, K., Li (Ni1/3Co1/3Mn1/3) O2 as a suitable cathode for high power applications. *Journal of Power Sources* **2003,** *123* (2), 247-252.

122. Manthiram, A.; Knight, J. C.; Myung, S. T.; Oh, S. M.; Sun, Y. K., Nickel‐Rich and Lithium‐Rich Layered Oxide Cathodes: Progress and Perspectives. *Advanced Energy Materials* **2016,** *6* (1).

123. Liang, L.; Du, K.; Peng, Z.; Cao, Y.; Duan, J.; Jiang, J.; Hu, G., Co–precipitation synthesis of Ni0. 6Co0. 2Mn0. 2 (OH) 2 precursor and characterization of LiNi0. 6Co0. 2Mn0. 2O2 cathode material for secondary lithium batteries. *Electrochimica Acta* **2014,** *130*, 82-89.

124. Noh, H.-J.; Youn, S.; Yoon, C. S.; Sun, Y.-K., Comparison of the structural and electrochemical properties of layered Li[NixCoyMnz]O2 (x = 1/3, 0.5, 0.6, 0.7, 0.8 and 0.85) cathode material for lithium-ion batteries. *Journal of Power Sources* **2013,** *233*, 121-130.

125. Zheng, J.; Kan, W. H.; Manthiram, A., Role of Mn Content on the Electrochemical Properties of Nickel-Rich Layered LiNi0. 8 − x Co0. 1Mn0. 1+ x O2 (0.0⩽ x⩽ 0.08) Cathodes for Lithium-Ion Batteries. *ACS applied materials & interfaces* **2015,** *7* (12), 6926-6934.

126. Sun, H.-H.; Choi, W.; Lee, J. K.; Oh, I.-H.; Jung, H.-G., Control of electrochemical properties of nickel-rich layered cathode materials for lithium ion batteries by variation of the manganese to cobalt ratio. *Journal of Power Sources* **2015,** *275*, 877-883.

127. Xiong, X.; Wang, Z.; Yan, G.; Guo, H.; Li, X., Role of V2O5 coating on LiNiO2-based materials for lithium ion battery. *Journal of Power Sources* **2014,** *245*, 183-193.

128. Kim, N. Y.; Yim, T.; Song, J. H.; Yu, J.-S.; Lee, Z., Microstructural study on degradation mechanism of layered LiNi0. 6Co0. 2Mn0. 2O2 cathode materials by analytical transmission electron microscopy. *Journal of power sources* **2016,** *307*, 641-648.

129. Mu, L.; Lin, R.; Xu, R.; Han, L.; Xia, S.; Sokaras, D.; Steiner, J. D.; Weng, T. C.; Nordlund, D.; Doeff, M. M.; Liu, Y.; Zhao, K.; Xin, H. L.; Lin, F., Oxygen Release Induced Chemomechanical Breakdown of Layered Cathode Materials. *Nano Lett* **2018,** *18* (5), 3241-3249.

130. Lin, F.; Markus, I. M.; Nordlund, D.; Weng, T.-C.; Asta, M. D.; Xin, H. L.; Doeff, M. M., Surface reconstruction and chemical evolution of stoichiometric layered cathode materials for lithium-ion batteries. *Nature communications* **2014,** *5*, 3529.

131. Xia, J.; Ma, L.; Nelson, K.; Nie, M.; Lu, Z.; Dahn, J., A Study of Li-Ion Cells Operated to 4.5 V and at 55 C. *Journal of The Electrochemical Society* **2016,** *163* (10), A2399-A2406.

132. Lee, Y.-S.; Shin, W.-K.; Kannan, A. G.; Koo, S. M.; Kim, D.-W., Improvement of the cycling performance and thermal stability of lithium-ion cells by double-layer coating of cathode materials with Al2O3 nanoparticles and conductive polymer. *ACS applied materials & interfaces* **2015,** *7* (25), 13944-13951.

133. Xu, Y.; Liu, Y.; Lu, Z.; Wang, H.; Sun, D.; Yang, G., The preparation and role of Li2ZrO3 surface coating LiNi0.5Co0.2Mn0.3O2 as cathode for lithium-ion batteries. *Applied Surface Science* **2016,** *361*, 150-156.

134. Ni, J.; Zhou, H.; Chen, J.; Zhang, X., Improved electrochemical performance of layered LiNi0.4Co0.2Mn0.4O2 via Li2ZrO3 coating. *Electrochimica Acta* **2008,** *53* (7), 3075-3083.

135. Wang, D.; Li, X.; Wang, Z.; Guo, H.; Huang, Z.; Kong, L.; Ru, J., Improved high voltage electrochemical performance of Li 2 ZrO 3 -coated LiNi 0.5 Co 0.2 Mn 0.3 O 2 cathode material. *Journal of Alloys and Compounds* **2015,** *647*, 612-619.

136. Sun, S.; Du, C.; Qu, D.; Zhang, X.; Tang, Z., Li2ZrO3-coated LiNi0. 6Co0. 2Mn0. 2O2 for high-performance cathode material in lithium-ion battery. *Ionics* **2015,** *21* (7), 2091-2100.

137. Liang, H.; Wang, Z.; Guo, H.; Wang, J.; Leng, J., Improvement in the electrochemical performance of LiNi0. 8Co0. 1Mn0. 1O2 cathode material by Li2ZrO3 coating. *Applied Surface Science* **2017,** *423*, 1045-1053.

138. Schipper, F.; Bouzaglo, H.; Dixit, M.; Erickson, E. M.; Weigel, T.; Talianker, M.; Grinblat, J.; Burstein, L.; Schmidt, M.; Lampert, J., From Surface ZrO2 Coating to Bulk Zr Doping by High Temperature Annealing of Nickel‐Rich Lithiated Oxides and Their Enhanced Electrochemical Performance in Lithium Ion Batteries. *Advanced Energy Materials* **2018,** *8* (4).

139. Li, X.; Zhang, K.; Wang, M.; Liu, Y.; Qu, M.; Zhao, W.; Zheng, J., Dual functions of zirconium modification on improving the electrochemical performance of Ni-rich LiNi0.8Co0.1Mn0.1O2. *Sustainable Energy & Fuels* **2018,** *2* (2), 413-421.

140. Gao, S.; Zhan, X.; Cheng, Y.-T., Structural, Electrochemical and Li-Ion Transport Properties of Zr-Modified LiNi0.8Co0.1Mn0.1O2 Positive Electrode Materials for Lithium-Ion Batteries. *Journal of Power Sources* **2018,** DOI: 10.1016/j.jpowsour.2018.10.094.

141. Wang, W.; Yin, Z.; Wang, J.; Wang, Z.; Li, X.; Guo, H., Effect of heat-treatment on Li2ZrO3-coated LiNi1/3Co1/3Mn1/3O2 and its high voltage electrochemical performance. *Journal of Alloys and Compounds* **2015,** *651*, 737-743.

142. Ohzuku, T.; Ueda, A.; Nagayama, M., Electrochemistry and structural chemistry of LiNiO2 (R3m) for 4 volt secondary lithium cells. *Journal of the Electrochemical Society* **1993,** *140* (7), 1862-1870.

143. Chen, Z.; Dahn, J., Effect of a ZrO2 coating on the structure and electrochemistry of Li x CoO2 when cycled to 4.5 V. *Electrochemical and solid-state letters* **2002,** *5* (10), A213-A216.

144. Li, Y.; Wang, Z.; Li, C.; Cao, Y.; Guo, X., Densification and ionic-conduction improvement of lithium garnet solid electrolytes by flowing oxygen sintering. *Journal of Power Sources* **2014,** *248*, 642-646.

145. Sun, P.; Xu, C. N.; Akiyama, M.; Watanabe, T., Controlled oxygen partial pressure sintering of (Pb, La)(Zr, Ti) O3 ceramics. *Journal of the American Ceramic Society* **1999,** *82* (6), 1447-1450.

146. Zhan, X.; Lai, S.; Gobet, M. P.; Greenbaum, S. G.; Shirpour, M., Defect chemistry and electrical properties of garnet-type Li7La3Zr2O12. *Phys Chem Chem Phys* **2018,** *20* (3), 1447-1459.

147. Chen, D.; Cao, Y.; Weng, D.; Tuller, H. L., Defect and Transport Model of Ceria–Zirconia Solid Solutions: Ce0.8Zr0.2O2−δ—An Electrical Conductivity Study. *Chemistry of Materials* **2014,** *26* (17), 5143-5150.

148. Kang, B.; Ceder, G., Battery materials for ultrafast charging and discharging. *Nature* **2009,** *458* (7235), 190.

149. Li, D.; Kato, Y.; Kobayakawa, K.; Noguchi, H.; Sato, Y., Preparation and electrochemical characteristics of LiNi1/3Mn1/3Co1/3O2 coated with metal oxides coating. *Journal of Power Sources* **2006,** *160* (2), 1342-1348.

150. Li, X.; Liu, J.; Banis, M. N.; Lushington, A.; Li, R.; Cai, M.; Sun, X., Atomic layer deposition of solid-state electrolyte coated cathode materials with superior high-voltage cycling behavior for lithium ion battery application. *Energy & Environmental Science* **2014,** *7* (2), 768-778.

151. Zhuang, Q.-C.; Wei, T.; Du, L.-L.; Cui, Y.-L.; Fang, L.; Sun, S.-G., An electrochemical impedance spectroscopic study of the electronic and ionic transport properties of spinel LiMn2O4. *The Journal of Physical Chemistry C* **2010,** *114* (18), 8614-8621.

152. Ju, S. H.; Kang, I. S.; Lee, Y. S.; Shin, W. K.; Kim, S.; Shin, K.; Kim, D. W., Improvement of the cycling performance of LiNi(0.6)Co(0.2)Mn(0.2)O(2) cathode active materials by a dual-conductive polymer coating. *ACS Appl Mater Interfaces* **2014,** *6* (4), 2546-52.

153. Song, M. Y.; Lee, D. S.; Park, H. R., Electrochemical properties of LiNi1− yTiyO2 and LiNi0. 975M0. 025O2 (M= Zn, Al, and Ti) synthesized by the solid-state reaction method. *Materials Research Bulletin* **2012,** *47* (4), 1021-1027.

154. Huang, Z.; Wang, Z.; Guo, H.; Li, X., Influence of Mg 2+ doping on the structure and electrochemical performances of layered LiNi 0.6 Co 0.2-x Mn 0.2 Mg x O 2 cathode materials. *Journal of Alloys and Compounds* **2016,** *671*, 479-485.

155. Li, X.; Liu, J.; Banis, M. N.; Lushington, A.; Li, R.; Cai, M.; Sun, X., Atomic layer deposition of solid-state electrolyte coated cathode materials with superior high-voltage cycling behavior for lithium ion battery application. *Energy Environ. Sci.* **2014,** *7* (2), 768-778.

156. Kaneda, H., Improving the Cycling Performance and Thermal Stability of LiNi0.6Co0.2Mn0.2O2 Cathode Materials by Nb-doping and Surface Modification. *International Journal of Electrochemical Science* **2017**, 4640-4653.

157. Huang, Z.; Wang, Z.; Jing, Q.; Guo, H.; Li, X.; Yang, Z., Investigation on the effect of Na doping on structure and Li-ion kinetics of layered LiNi0. 6Co0. 2Mn0. 2O2 cathode material. *Electrochimica Acta* **2016,** *192*, 120-126.

158. Zhang, Y.; Wang, Z.-B.; Yu, F.-D.; Que, L.-F.; Wang, M.-J.; Xia, Y.-F.; Xue, Y.; Wu, J., Studies on stability and capacity for long-life cycle performance of Li(Ni 0.5 Co 0.2 Mn 0.3)O 2 by Mo modification for lithium-ion battery. *Journal of Power Sources* **2017,** *358*, 1-12.

159. Shaju, K. M.; Subba Rao, G. V.; Chowdari, B. V. R., Performance of layered Li(Ni1/3Co1/3Mn1/3)O2 as cathode for Li-ion batteries. *Electrochimica Acta* **2002,** *48* (2), 145-151.

160. Tang, K.; Yu, X.; Sun, J.; Li, H.; Huang, X., Kinetic analysis on LiFePO4 thin films by CV, GITT, and EIS. *Electrochimica Acta* **2011,** *56* (13), 4869-4875.

Vita

EDUCATION

- **Ph.D**., Materials Science & Engineering, University of Kentucky 2018
- **B.S.**, Materials Science & Engineering, University of Science and Technology Beijing 2014

PUBLICATIONS

- X. Zhan, M. Shirpour, *Evolution of Solid/Aqueous Interface in Aqueous Sodium-Ion Batteries*, Chem. Commun., 2017, 53, 204-207.
- X. Zhan, M. Shirpour, F. Yang, *A Thermodynamic Perspective for Formation of Solid Electrolyte Interphase in Lithium-Ion Batteries*, Electrochimica Acta, 2015, 173, 736-742.
- X. Zhan, Shen Lai, M. P. Gobet, S. G. Greenbaum, M. Shirpour, *Defect Chemistry and Electrical Properties of Garnet-Type* $Li_7La_3Zr_2O_{12}$, Phys. Chem. Chem. Phys.**,** 2018, 20, 1447-1459.
- X. Zhan, M. Shirpour, Y.T. Cheng, *Nonstoichiometry and Li-Ion Transport in Lithium Zirconate: The Role of Oxygen Vacancies*, J. Am. Ceram. Soc., 2018, 101, 4053-4065.
- L. Zhang, X. Zhan, Y.T. Cheng, and M. Shirpour, *Charge Transport in Electronic-Ionic Composites*, J. Phys. Chem. Lett., 2017, 8, 5385-5389.
- S. Gao, X. Zhan, Y.T. Cheng, *Structural, Electrochemical and Li-Ion Transport Properties of Zr-Modified* $LiNi_{0.8}Co_{0.1}Mn_{0.1}O_2$ *Positive Electrode Materials for Lithium-Ion Batteries*, J. Power Sources, DOI: 10.1016/j.jpowsour.2018.10.094.
- M. Shirpour, X. Zhan, M. Doeff, *Sodium-Ion Batteries: "Beyond Lithium-Ion"*, 2015 TechConnect World Innovation Conference and the National Innovation Summit, Washington, DC.

TECHNICAL PRESENTATIONS

- **X. Zhan**, M. Shirpour and F. Yang, *Analysis of the Formation and Growth of Solid Electrolyte Interphase in Lithium-Ion Batteries,* MS&T15 Technical Meeting and Exhibition, Columbus, OH (oral).
- **X. Zhan**, M. Shirpour, *Defect Chemistry and Electrical Properties of Garnet-Type* $Li_7La_3Zr_2O_{12}$, 231st ECS Meeting**,** New Orleans, LA (oral).
- **X. Zhan**, M. Shirpour, *Anode Surface Evolution in Aqueous Sodium-Ion Batteries Sodium-Ion Battery*, 231st ECS Meeting, New Orleans, LA (oral).
- **X. Zhan**, M. Shirpour, Y.T. Cheng, *Defect Chemistry and Lithium-Ion Transport in Doped* Li_2ZrO_3*: The Role of Oxygen Vacancies*, 233rd ECS Meeting, Seattle, WA (oral).
- **X. Zhan,** S. Lai, M.P. Gobet, S.G. Greenbaum, M. Shirpour, and Y.T. Cheng, *Revealing the relationship between defect chemistry and Li-ion transport in solid electrolytes for all-solid-state Li-ion batteries*, Beyond Lithium Ion XI by NASA, Cleveland, OH (poster).

HONORS & AWARDS

- **ECS Battery Division Travel Grant**, 231st ECS Meeting, New Orleans, 2017.
- **ECS Battery Division Travel Grant**, 233rd ECS Meeting, Seattle, 2018.
- **Outstanding Graduate Student Award**, University of Kentucky, 2018.
- **1st Place Award,** Beyond Lithium Ion XI poster session, NASA and Ohio Aerospace Institute, 2018

PROFESSIONAL SERVICES & MEMBERSHIPS

- **Chair,** the Electrochemical Society (ECS) Kentucky Student Chapter 2016-2018
- **Treasurer**, the ECS Kentucky Student Chapter 2015-2016
- **Member** of the ECS and the Materials Research Society 2014-present